UNIVERSITY OF PARMA

DEPARTMENT OF CHEMICAL, LIFE AND ENVIRONMENTAL SUSTAINABILITY SCIENCES

Doctor of Philosophy in Materials Science and Technology

Cycle XXXVII

Electron Crystallography of Organic Nanocrystals

Tutor:

Dr. Mauro Gemmi

Coordinator:

Prof. Mauro Riccò

Candidate:

Vincentia Emerson Agbemeh

ANNI ACCADEMICI 2022 - 2025

Content

List of Abbreviations

3D	Three-Dimensional
2D	Two-Dimensional
3D ED	Three-Dimensional Electron Diffraction
SCXRD	Single Crystal X-ray Diffraction
PXRD	Powder X-ray Diffraction
TEM	Transmission Electron Microscope (Microscopy)
CryoEM	Cryo-Electron Microscopy
NED	Nanobeam Electron Diffraction
SAED	Selected Area Electron Diffraction
PEDT	Precession Electron Diffraction Tomography
SerialED	Serial Electron Diffraction
XFEL	X-ray Free-Electron Laser
PETS2	Process Electron Tilt Series
XDS	X-ray Detector Software
DIALS	Diffraction Integration for Advanced Light Sources
CCD	Charge-Coupled Device
STEM	Scanning Transmission Electron Microscope
HAADF	High-Angle Angular Dark Field
CRED	Continuous Rotation Electron Diffraction
ADT	Automated Electron Diffraction Tomography
SA	Simulated Annealing
API	Active Pharmaceutical Ingredient
ORV	Oxyresveratrol
Nic	Nicotinamide
Iso	Isonicotinamide
LAG	Liquid Assisted Grinding
U	Urea

A-ORV	Anhydrate Oxyresveratrol
H-ORV	Hydrate Oxyresveratrol
MicroED	Micro Electron Diffraction
Cif	Crystallographic Information Frameworks
CCDC	Cambridge Crystallographic Data Centre
DFT	Density Functional Theory
TGA	Thermal Gravimetric Analysis
DSC	Differential Scanning Calorimetry
FDA	Food and Drug Authority
HIV	Human Immunodeficiency Virus
NMR	Nuclear Magnetic Resonance
GRAS	Generally Recognized as Safe
US FDA	United States Food and Drugs Administration
MOF	Metal-Organic Framework

Abstract

This thesis focuses on the application of 3D electron diffraction (3D ED) in studying the crystal structures of natural products that may exist in nanocrystalline forms, as well as cocrystals synthesized via mechanochemistry. The 3D ED technique offers an alternative for crystal structure elucidation of submicron-sized crystalline samples that are unsuitable for the conventional single crystal X-ray diffraction (SCXRD) technique. The first part of the thesis introduces the fundamentals of 3D ED, including instrumentation, diffraction geometry in electron diffraction, data collection and data processing strategies. Sample preparation methods for either stable, beam or vacuum-sensitive samples are also discussed. Building on this foundation, the application of the technique in the round robin project was reported to establish the reproducibility of 3D ED. The results of 3D ED analysis by various laboratories demonstrated the reliability of the technique regardless of the instrument used in the analysis. 3D ED was then applied for the investigation of crystal structures of unreported phases of the natural product oxyresveratrol. Two new phases were found, including one anhydrate phase and a novel hydrate polymorph. Additionally, the crystal structures of three oxyresveratrol cocrystals synthesized using mechanochemistry were uncovered using 3D ED. To address the problem of beam sensitivity, which is a common challenge during data acquisition on organic samples, a novel method of data collection serial electron diffraction (SerialED), has been applied for the collection of diffraction data on a well-known active pharmaceutical ingredient, L-dopa. Preliminary results after the data analysis have been reported, showing a promising future for SerialED method of data collection.

Introduction

1.1. 3D Electron Diffraction

Over the last 20 years, electron diffraction has undergone impressive developments. From being a niche technique for crystallography, it has become a reliable and powerful structure solution method. If it was originally used mainly to obtain qualitative information on the crystal structure through the collection of single selected area zone axis patterns, nowadays, in its 3D electron diffraction (3D ED) version, it is a single crystal diffraction technique for nanocrystals which can be used in the same way as single crystal X-ray diffraction, but on crystals that are two orders of magnitudes smaller. In this thesis, we exploit this remarkable characteristic of 3D ED for studying the crystal structures of natural products that may exist in nanocrystalline forms, as well as cocrystals synthesized via mechanochemistry.

The standard technique used for structure determination is single crystal x-ray diffraction (SCXRD). However, SCXRD cannot be used for characterizing crystals that are smaller than a few microns unless a very powerful synchrotron beamline is available, Powder X-ray diffraction (PXRD) is applied in such scenarios. PXRD is another X-ray diffraction technique that is used for the analysis of crystalline materials that are small-grained powders, which are not suitable for SCXRD. An ideal sample for PXRD analysis is made up of crystallites with sizes between 1 to 10 microns with random orientations (Altomare et al., 2017). In this case, the weak diffraction signal arising from each small grain is enhanced by the large number of grains that are simultaneously diffracting at the same time. This technique is widely used in the pharmaceutical industry as an efficient way of screening polymorphs and multicomponent solid forms of APIs during early-stage development (Ticona Chambi et al., 2024) (Chernyshev, 2023). It is also used for crystal structure determination and understanding temperature dependent phase transformations (Harry G. Brittain, 2009). This diffraction method however also comes with some setbacks. If the sample is not a single crystalline phase or contains some

minor phases it can be hard to define the different phases due to overlapping of peaks. The PXRD diffraction signal is in fact, a one-dimensional signal in which we record the number of diffracted photons vs. the scattering angle, therefore the diffraction signals coming from all the grains in the samples are superimposed in the powder pattern. This makes the crystal structure analysis of unknown compounds containing multiple phases an extremely challenging task(Li & Sun, 2017). (Altomare et al., 2017). To overcome this limitation, 3D Electron Diffraction (3D ED) has proven to be the technique of choice for analyzing nano-sized crystals (Gemmi & Lanza, 2019).

3D electron diffraction (3D ED) is a single crystal diffraction technique that allows for the *ab initio* structure solution of small crystals (smaller than 1 micron and thinner than several hundreds of nanometers) including organic nanocrystals (Andrusenko & Gemmi, 2022). 3D ED for organic nanocrystals however presents several challenges during data collection. Firstly, due to the presence of light atoms, these samples are susceptible to beam damage. Very rapidly, the effect of the electron beam can amorphize the crystals leading to low data quality and completeness. In this work, low-dose and fast data acquisition methods have been applied to make data collection feasible for organic nanocrystals. The instrument used for 3D ED data collection is the transmission electron microscope (TEM), therefore the sample inside the TEM is in a high vacuum environment. Some samples may experience amorphization in these extreme vacuum conditions and are known as vacuum-sensitive materials. This thesis also applies a classical sample preparation employed in cryo-EM, cryo-plunging method for protecting vacuum-sensitive samples. 3D Electron Diffraction (3D ED) has been combined with other characterisation methods such as Differential Scanning Calorimetry (DSC), Thermal Gravimetric Analysis (TGA) and PXRD. DSC and TGA were used to understand the thermal behaviour of the different crystal forms of the sample. PXRD has been used as a preliminary sample screening by comparing the experimental patterns with those simulated based on known

phases to check the presence of new unknown polymorphs. In case of detection of new phases, 3D ED has been used for their structure solution and refinement. The structural model obtained were cross checked through Rietveld refinement on the experimental PXRD that in some cases were multiphase patterns. This methodology has been successfully applied in this thesis to two relatively unexplored areas: crystal structure analysis of natural products and nanocrystalline cocrystals synthesized through mechanochemistry.

1.2. Active Pharmaceutical Ingredients(APIs)

Active Pharmaceutical Ingredients (APIs) small molecules can be administered in their amorphous forms, but some show better physicochemical properties and stability in their crystalline forms (Joshi et al., 2019). As a result, investigating and understanding the crystal structures of APIs is a key tool in drug development. This gives information about how to choose the correct crystal form for various therapeutic applications. Crystal forms of APIs (Figure 1.1) include polymorphs, hydrates/solvates, salts and cocrystals. An API in different crystal forms can exhibit different physicochemical properties, thereby influencing their potential use (Braga et al., 2022) (Couillaud et al., 2019).

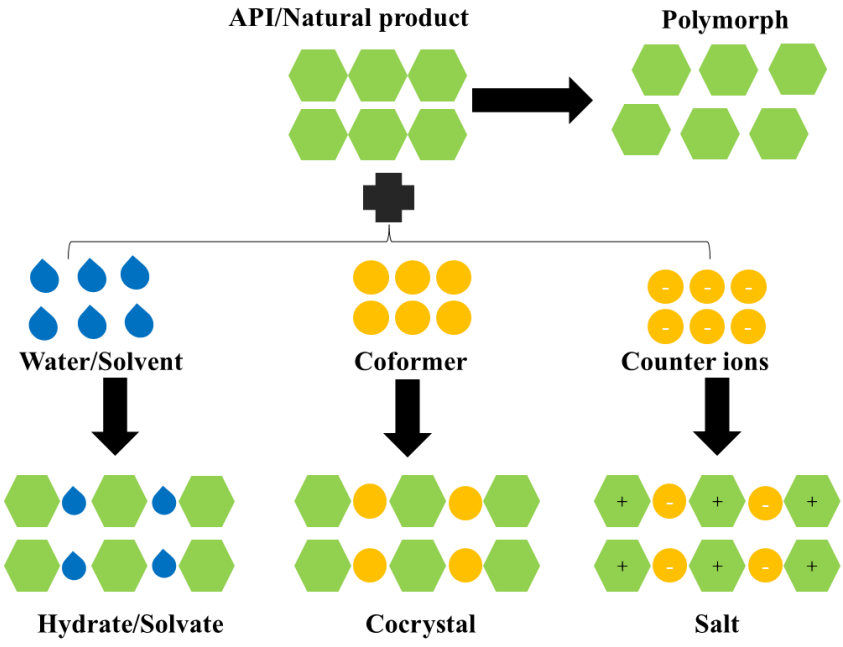

Figure 1. 1 Scheme of the various crystal forms of APIs

Crystal forms can exist with a single component such as anhydrous polymorphs or multicomponent including solvates, salts and cocrystals.

Polymorphs are the different crystal forms created due to the polymorphic tendencies of APIs. This phenomenon is described as polymorphism and occurs when a crystalline compound can have different molecular arrangements, which causes different unit cell parameters and crystal structures while its elemental composition remains the same (Healy et al., 2017). Polymorphism is very common in APIs and are present in about 80% of crystalline APIs (Yao et al., 2023). As a result, polymorphic screening is a routine in drug development, which is a requirement by the US FDA and for patent applications. This phenomenon can occur due to different factors such as temperature, humidity, mechanical stress and even light. The most thermodynamically stable polymorphs are selected for the market after various characterization is done (Harry G. Brittain, 2009). Thermodynamically unstable polymorphs are called the metastable forms which tend to appear or exist amongst other stable polymorphic forms. Salts, cocrystals, hydrate and solvates can all have different polymorphs (Braga et al., 2022) (Byrn et al., 2017). It has been reported that molecules that can form polymorphs also have a high likelihood of forming solvates (Couillaud et al., 2019). Solvated crystals or solvates are crystalline forms that contain molecules of solvents such as water, ethanol and acetone in their crystal lattice. Solvates that contain one or more molecules of water are known as hydrates. While APIs without any solvent or water in their structures are known as anhydrates. Anhydrates can transform into hydrates when stored in a high relative humidity condition (Couillaud et al., 2019). Research suggests that one-third of all APIs tend to form either a hydrate or a solvate. To give an example of how frequent and complex can be the formation of solvates, sulfathiazole is reported to have more than 100 solvated forms (Boothroyd et al., 2018). Although some APIs are marketed in their hydrated or solvated forms, they come with

some challenges such as poor thermal stability and inconsistencies with the stoichiometric ratio (Aitipamula & Vangala, 2017).

Studies show that about 40% of drugs on the market and 90% of APIs undergoing screening show low solubility which directly affects their bioactivity (Dhaval et al., 2025) (Hossain Mithu et al., 2021). To address this problem, many approaches have been used to improve the solubility using crystal engineering methods to form salts and cocrystals. Salts are a popular choice for administered API in solid form because of their improved solubility compared to their original pure state. Salts are made up of a basic and an acidic component held together by ionic interactions (Aitipamula & Vangala, 2017) (Byrn et al., 2017) (Hossain Mithu et al., 2021). A recent method of improving the solubility of orally administered drugs is by modifying their crystal structures through cocrystallization (Savjani et al., 2012) (Saha et al., 2023). Cocrystals are made up of at least one API combined with one or more coformers in their crystal lattice without altering their therapeutic properties. Coformers are small molecules which can sometimes fall under Generally Recognized as Safe (GRAS) compounds as defined by the US FDA (Bolla et al., 2022) (Artusio et al., 2024). GRAS compounds are typically amides and carboxylic acids (Qiao et al., 2011). Cocrystallization occurs because of non-covalent interactions such as hydrogen bonding, van der Waals force and pi-pi stacking interaction between coformers and the API molecules (Pal et al., 2022).

Characterization methods such as thermal studies (Differential Scanning Calorimetry (DSC), Thermogravimetric analysis (TGA)) and spectroscopy (Nuclear Magnetic Resonance (NMR), Raman, Infrared) (Jayant & Yusuf, 2024) (Southern & Bryce, 2021) (Pindelska et al., 2017) are necessary to understand crystal forms. The standard crystallographic techniques widely used for crystal structure analysis are Powder X-ray Diffraction (PXRD) and Single Crystal X-ray Diffraction (SCXRD).

1.3. Natural Products

Natural products and their derivatives are bioactive compounds sourced from plants that have played an important role throughout the history of human medicine (Harvey et al., 2015)(Dias et al., 2012). For example, Artemisinin is a natural product that can be extracted from *Artemisia annua L*. and has been used as an antimalarial drug since its discovery in 1987. This led to the award of half of the 2015 Nobel Prize in Physiology or Medicine for this development of artemisinin and the other half for avermectin/ivermectin complexes which are also of natural origin (J. Wang et al., 2019) (Newman & Cragg, 2016). Another example is the API aspirin, a household drug for the treatment of pain and inflammation. It is a derivative of the natural compound salicylic acid which can be extracted from the bark of the willow tree. However, salicylic acid had side effects like causing gastric irritation, so its acetyl derivative aspirin was created with a lower level of this side effect (Chopra & Dhingra, 2021). Natural compounds like most of the APIs exhibit polymorphism and exist in various crystal forms as seen in quercetin. Quercetin is a natural compound which can be extracted from many kinds of fruits such as tomatoes and onions and one of the most studied flavonoids with many desirable benefits. It is shown to exist in different crystal forms such as hydrates, solvates and cocrystals. It has also been reported to have two anhydrous polymorphs (Klitou et al., 2023). Curcumin is another natural product which is an anti-HIV agent and so far, has been shown to be polymorphic. It is reported to have three crystalline polymorphic and one amorphous phase (Sanphui et al., 2011). The potential biological activities of natural products are heavily reliance on their 3D crystal structure and the possible functional groups in the molecules (Chhetri et al., 2018). Many characterization methods of unknown natural products already exist such as NMR spectroscopy and mass spectrometry. The structural elucidation methods like X-ray crystallography have been used as a standard for crystalline natural products just like other APIs (Nicolaou & Snyder, 2005). The crystal structure determination of natural products using

3D electron diffraction is still a growing field (Danelius et al., 2021). Kim et al. in 2021 combined genome mining and 3D ED for revising the structure of fischerin. The crystal structure co-metabolite, austinol in the sample quantities below the detection limit of NMR analysis was solved using 3D ED (Kim et al., 2021). In 2024, Gurung et al. determined the crystal structure and absolute configuration of beauveriolide I, a natural fungal product that crystallizes in fibrous morphology (Gurung et al., 2024). Natural products are challenging to crystallize large enough for SCXRD and can also exist in polyphasic mixtures hence 3D ED is a key tool for their structural analysis.

In Chapter 4, we will discuss the crystal structure determination of two new crystal structures of oxyresveratrol solved *ab initio* using 3D ED by combining room and cryo temperature data collection.

1.4. Mechanochemical Synthesis for Crystal Engineering

There are different methods of synthesis used in the crystal engineering of API to create crystal forms with improved properties including solvothermal synthesis, sublimation and mechanochemical synthesis (Carstens et al., 2020). Mechanochemistry is a method of synthesis that involves the use of mechanical force to cause chemical reactions through grinding with little or no solvent. This synthesis route has several advantages over other methods. Firstly, due to the use of a low amount of or no solvent, there is minimal waste, which makes it a greener, less toxic and environmentally friendly method. The equipment for synthesis; ball mill device, mortar and pestle; are cost-effective (Figure 1.2) but also efficient and can be used in large-scale production (Hasa & Jones, 2017) (Basoccu et al., 2024) (Galant et al., 2022).

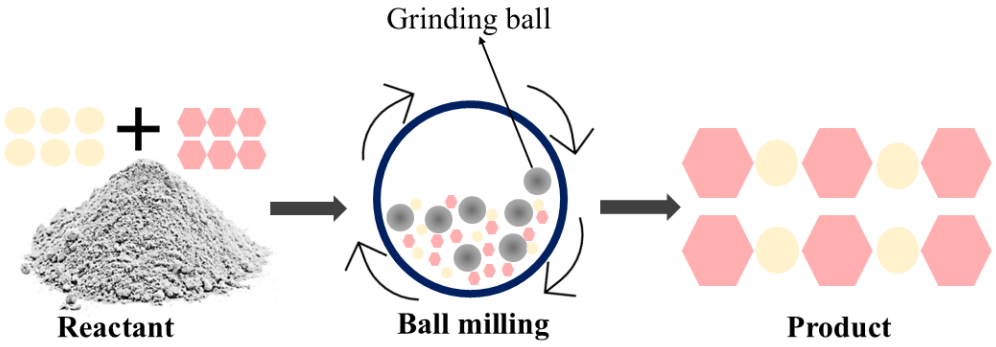

Figure 1. 2 Workflow of mechanochemical synthesis

Mechanochemical synthesis or mechanosynthesis includes neat grinding and liquid-assisted grinding (LAG) (Carstens et al., 2020). A limited amount of solvent is used to initiate reactions in LAG in cases where neat grinding is not successful (Do & Friščić, 2017). This synthesis route leads to the formation of nanocrystalline solids which are consequently difficult to characterize with the standard X-ray diffraction methods especially if new unknown crystal structures are formed. Efforts are made to grow larger single crystals after mechanosynthesis using other synthesis route for structure determination which can be unsuccessful or lead to the formation of different polymorphs. With crystals smaller than a few microns, the traditional XRD methods cannot be applied to the materials produced by mechanochemistry due to the reasons explained earlier. To tackle this, 3D ED can be the solution and has been used in various works with different materials including pharmaceuticals (Gogoi et al., 2023), Metal Organic Frame works (MOFs) (Sala et al., 2024), Supramolecular Organic Frameworks (SOF) (Marchetti et al., 2023) and coordination polymers (Marchetti et al., 2021).

In Chapter 5, we will discuss how 3D ED combined with PXRD, was used for the crystal structure analysis of three unknown cocrystals of oxyresveratrol synthesized using LAG mechanosynthesis.

1.5. Summary

The main scope of this thesis is to demonstrate that 3D ED has reached a sufficiently mature state, and is a reliable method for structure solution, even for samples that are challenging to

analyse due to their beam sensitivity to the illumination of an electron beam, such as organic crystals. We aim to demonstrate that 3D ED can free the organic chemist from the constraint of needing to synthesize and produce large crystals if they want to have a precise idea on which crystal structure/polymorph is obtained. We foresee that this could open a lot of new scenario in organic chemical synthesis with valuable applications, especially in pharmacology. The results of the thesis say that this is definitely possible. By going through the following chapters, 3D ED is able to provide a structure accuracy that is now better than PXRD and is approaching that of SCXRD. The results also show that organic structures can be investigated by 3D ED to a high degree of detail. Challenges such as the detection of the hydrogen or the determination of hydrated polymorphs, usually amorphized by the vacuum, can be addressed if proper sample preparation is considered. The example of the oxyresveratrol polymorphs crystal structure determination will also show how the method is ready for quality control. This is because two new polymorphs have been determined directly on the commercial batch bought from the chemical provider.

CHAPTER 2

3D Electron Diffraction

2.1. Introduction

3D Electron Diffraction (3D ED) or Microcrystal Electron Diffraction (Micro ED) is a technique for collecting single-crystal diffraction data on nanocrystals by recording patterns while the sample is rotating around a goniometer axis using accelerated electrons as a radiation source (Gemmi et al., 2019). The collected diffraction patterns can be analyzed like a single phi scan in a single crystal X-ray diffraction (SCXRD) for obtaining a reconstruction of the reciprocal space (Gemmi et al., 2015). This diffraction technique is ideal for the crystal structure characterization of single nanocrystals due to the stronger interactions between electrons and matter compared to X-ray-matter interaction (Gemmi et al., 2019). Electron diffraction was among the first proof of the wave-like nature of matter through the famous Davisson-Germer experiment. In their work, electrons were scattered by a nickel crystal by forming Bragg diffraction rings (Zettili, 2009). The electron beam interacts with the nuclei and electron clouds of the atoms via Coulomb forces. These are electrostatic forces that occur because of repulsion or attraction between charged particles (J. M. Zuo & Spence, 2016). The deflection induced by the force onto the electron beam is between 3 to 4 orders of magnitude stronger than that produced on a photon beam in the case of X-ray diffraction (Dorset, 1995). As a result, electron diffraction produces detectable diffraction signals from crystals of volumes 10^{-6} times smaller than those usually analyzed with SCXRD (Clabbers & Xu, 2020). To give a clearer comparison, a perfect crystal for laboratory SCXRD has a size of around 100 μm while a perfect crystal for electron diffraction is smaller than 500nm. 3D ED has other advantages: it can be used to easily identify the positions of light atoms such as carbon, nitrogen, oxygen, and hydrogen which are prevalent in organic structures and it is more sensitive than X-ray to determine the absolute structure of a chiral crystal (Klar et al., 2023). 3D ED has been

instrumental in the structure determination of small molecules such as pharmaceuticals whose structures had not been previously known due to their nanocrystalline form (Andrusenko & Gemmi, 2022).

The main instrument used for collecting 3D ED data is the Transmission Electron Microscope (TEM) since it can be used as a diffraction instrument with the accelerated electrons as probe (Dorset, 1995). The versatility of the TEM has been valuable for understanding nanostructured materials exploiting at the same time its capabilities of observing the sample in image mode at high magnification (Escalante et al., 2019) and in diffraction mode to directly probe the crystal structure. In the following paragraph, this peculiar characteristic of the TEM will be reviewed and with a focus on how it can function as an electron diffractometer.

2.2. Transmission Electron Microscope (TEM)

The TEM can be divided into four main parts: the electron gun, the illumination system, the objective lens and the projector system. The electron gun produces electrons which are accelerated to form the electron beam (Figure 2.1) (R. F. Egerton, 2005). Thanks to the fact that a magnetic field can deflect accelerated electrons, the illumination system can focus, through magnetic lenses, the electrons into a small bright electron beam with variable size, dose and convergence. The illumination system, an important part of TEM, is made up of condenser lenses and different-sized condenser apertures that determine different beam sizes (J. M. Zuo & Spence, 2016). The electron beam can be either convergent or parallel producing different illumination types at the level of the sample. When the condenser lens is used to defocus or spread the beam, a quasi-parallel beam is created with a small convergence angle on the sample plane. On the contrary, a convergent beam is created when the beam is focused into a point to form an almost conelike probe (J.-M. Zuo, 2006) (Cowley, 1992). Below the illumination system is the imaging system which consists of the objective lens. With the objective lens, magnified images of thin electron-transparent samples can be produced

(Williams & Carter, 2009). The magnified image can be studied to get detailed information at the atomic level of the sample when the microscope functions in imaging mode. Remarkably, as is the case with every optical system, the objective lens produces at its back focal plane a diffraction pattern of the illuminated area. Below the objective lens is the projection lens system which has two important functions. The first is to serve as a tool for adjusting the magnification. The second function is to help switch the TEM from a traditional microscope for imaging to a diffractometer. When the projection system images on the screen the image plane of the objective lens, the operator sees the image of the sample. Meanwhile, when the projection system images the back focal plane, the operator can see the diffraction pattern (Figure 2.1). While a lot can be said about the imaging theory in the TEM, the samples studied in this thesis are usually quite beam-sensitive and have completely unknown structures, therefore they can be hardly studied in image mode at high magnification. In fact, if we want to obtain a high-resolution image, we need to focus the beam onto the small area we are imaging exposing it to a high dose, which usually amorphized beam-sensitive samples. For these reasons, the samples investigated in this thesis are studied in diffraction mode and imaging is only used at small or medium magnifications for searching the crystals of interest and to highlight only their morphology.

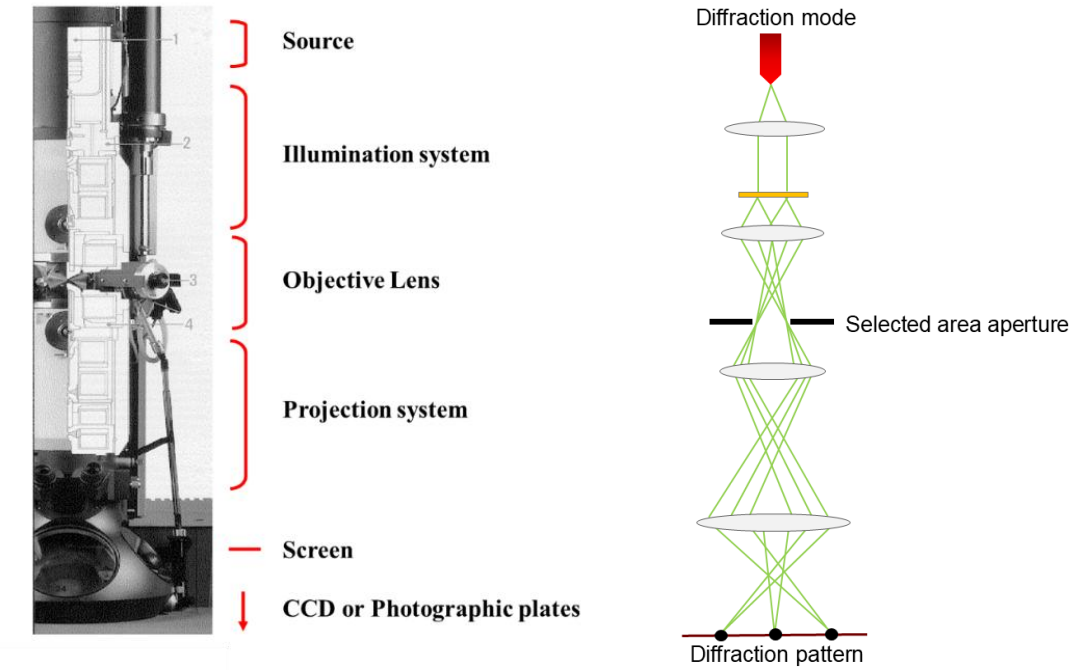

Figure 2. 1 TEM illumination system and diffraction mode configuration

2.2.1. Selected Area Electron Diffraction and Nanobeam Electron Diffraction

When the TEM operates in diffraction mode, with the projection system bringing the back focal plane of the objective lens onto the screen, two types of electron diffraction configurations are possible: Selected Area Electron Diffraction (SAED) and Nanobeam Electron Diffraction (NED) (Figure2.2). SAED is a type of electron diffraction in which the diffracting area is selected by positioning an aperture at the image plane of the objective lens, allowing the beam to illuminate an area larger than the diffracting crystal (J. M. Zuo & Spence, 2016). Different aperture sizes of SAED determine varying sizes of diffracting areas. NED is performed with a smaller parallel beam formed by the condenser lens, whose sizes are determined by the inserted condenser aperture. In this case, the size of the beam directly determines the diffracting area and only the diffracting area is illuminated and nothing else. The beam size can sometimes be smaller than the crystal, as a result, it can be directed to a specific region of the crystal during diffraction. This gives the advantage of minimizing beam damage on crystals that are not of interest during the data collection of a selected crystal. Since the beam size is relatively smaller than in SAED, there is also a reduction of the background from other crystals close to the

measured one or the continuous carbon film of the grid during the data collection (Plana-Ruiz et al., 2020).

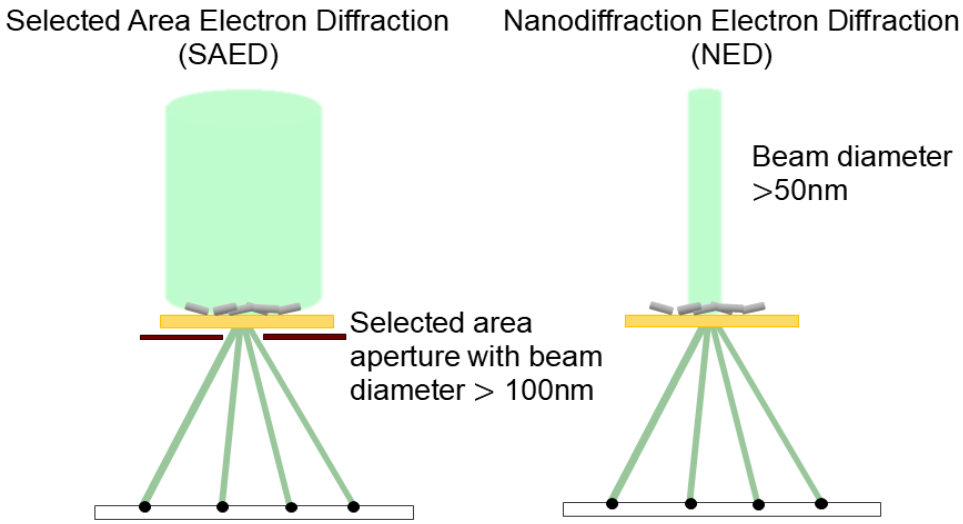

Figure 2. 2 Scheme of SAED vs NED configurations

2.2.2. STEM and TEM Imaging for Crystal Search

Although the TEM is used as a diffractometer in 3D ED data collection, the imaging capability of the TEM is still exploited to search for suitable crystals for diffraction. Given this, there are two modes of imaging for crystal search: the TEM and STEM mode (Figure 2.3).

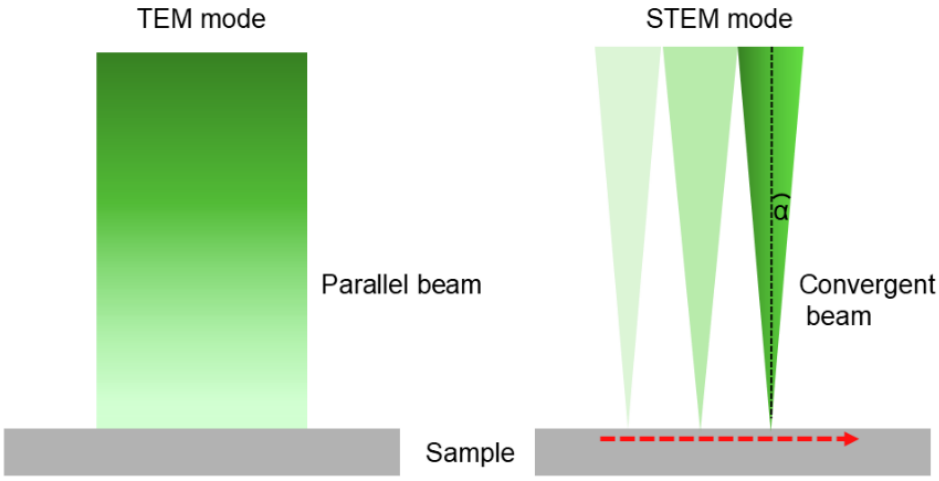

Figure 2. 3 TEM and STEM imaging modes for crystal search involving the use of different beam illumination

TEM mode uses a large parallel beam to illuminate an area of interest and is the standard imaging mode present in every TEM. It is used for crystal search when diffraction is performed in SAED (Goodhew, 2011). A major setback of the TEM mode is the high electron dose which damages organic samples. If we want to search a certain area, the entire area is illuminated with a certain exposure while inspecting it for suitable crystals. This means accumulating the electron dose on all the crystals in the area. Scanning Transmission Electron Microscopy (STEM) mode is a method of obtaining high-contrast images using a smaller electron beam as a probe combined with the High-Angle Angular Dark Field (HAADF) detector. The main advantage of this technique is that a fast scan of a region of interest can be done to produce an image after which the scan is frozen, and the beam is blanked. This means the scanned region is no longer illuminated hence a search for a suitable crystal is done on the image without beam-damaging the crystals. The STEM mode can use either a small convergent or a larger parallel beam. In the STEM convergent, the beam is converged at an angle α to form a scanning probe having a very narrow size which allows sub-nanometric resolution (which reaches the Ångström size in the best microscopes).

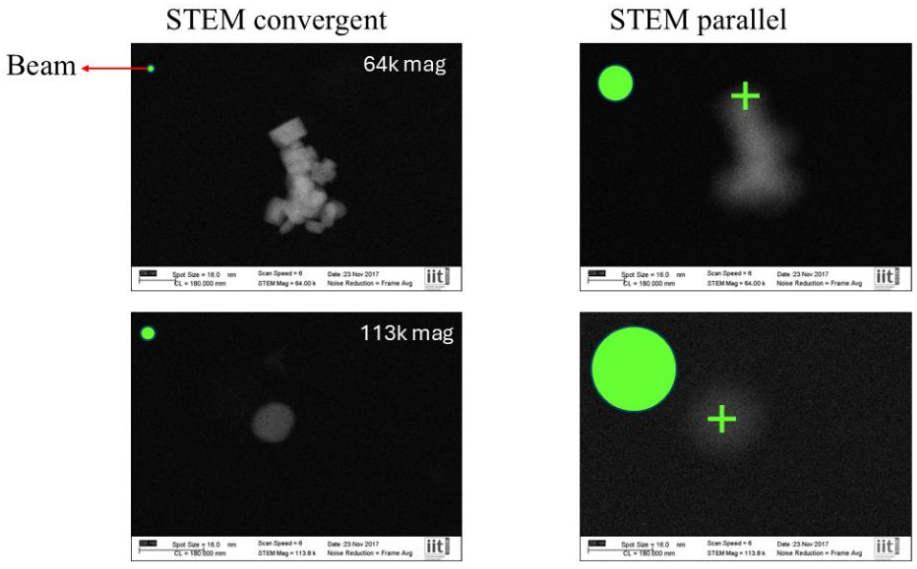

Figure 2. 4 Different visibility levels for crystal search in STEM convergent and STEM parallel beam imaging modes

The STEM parallel mode employs a small parallel beam, which is usually larger than the convergent one and produces blurred images (Figure 2.4). Consequently, there is reduced visibility of the crystals but still sufficient to complete a crystal search as shown in Figure 2.4. This is the modality we use when we are working in NED, since without changing any electron optical configuration we can locate the beam onto every crystal in the image and check its diffraction with our direct electron detector. This can be done by directly clicking with the mouse on the frozen image with the beam still blanked, avoiding then any extra electron dose. After data collection, the STEM convergent beam can be used for imaging crystals to check the morphology and sizes of the crystals using the best image performances available in the microscope.

2.3. Electron Diffraction Theory

As mentioned earlier in the chapter, electrons have both particle and wave-like properties, therefore their wavelength, λ in vacuum can be calculated using the relation proposed by Louis de Broglie expressed as:

$$\lambda = \frac{h}{p} = \frac{h}{\sqrt{2mE_0}} \tag{1}$$

where m is the electron relativistic mass, h the Planck's constant, and E_0 the kinetic energy given to the electrons by the accelerating voltage of the TEM (J. M. Zuo & Spence, 2016). The electrons in a TEM with an accelerating voltage of 120 kV will have λ= 0.03350 Å while with 200 kV they have λ= 0.025079 Å. It is also important to note that the wavelength of the electrons in a TEM is around one hundred times smaller than photons used in a laboratory X-ray diffractometer. For instance, the standard Cu Kα source has a wavelength of 1.5406 Å.

Although electron diffraction is produced by a different interaction with matter with respect to X-ray diffraction, its diffraction geometry is analogous to X-ray and follows the same laws. In crystalline materials, the atoms and molecules are arranged in a three-dimensional periodic

manner, hence, any scattered radiation interferes to form diffraction spots. The diffraction spots also follow a periodic three-dimensional order which is known as the reciprocal lattice.

The diffraction phenomenon (X-ray or electrons) can be well described by Bragg's law which states that:

$$2dsin\theta = n\lambda \tag{2}$$

Where 2θ is the scattering angle, d is the interplanar spacing, n is a positive integer indicating the diffraction order and finally λ is the wavelength.

According to Bragg's law, there will not be scattered particles along any direction of sight except when the crystal is oriented in such a way that a set of direct lattice planes satisfies the equation above (Figure 2.5). In that case, if the detector is oriented along a 2θ angle with respect to the incoming beam it will pick up the corresponding diffraction signal.

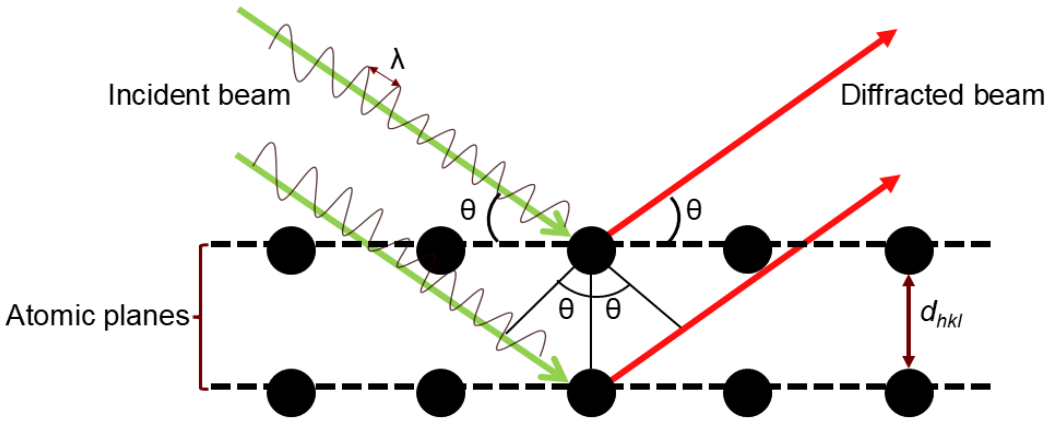

Figure 2. 5 Scheme of the Bragg diffraction law

Remarkably, this is valid for both X-ray and electrons provided the correct wavelength is inserted into the formula. To better visualize and understand the geometry of diffraction, a geometric construction has been adopted called Ewald sphere. Since diffraction is an elastic phenomenon, the energy of the diffracted electrons is the same as the incoming beam. Quantum mechanics states that the energy of a free particle is proportional to the square modulus of its

wave vector defined as $|k| = \frac{1}{\lambda}$ therefore, the wave vector of the incoming (k_0) and diffracted (k) particles must have the same length. This implies that they must lie on a sphere surface known as the Ewald sphere (Figure 2.6).

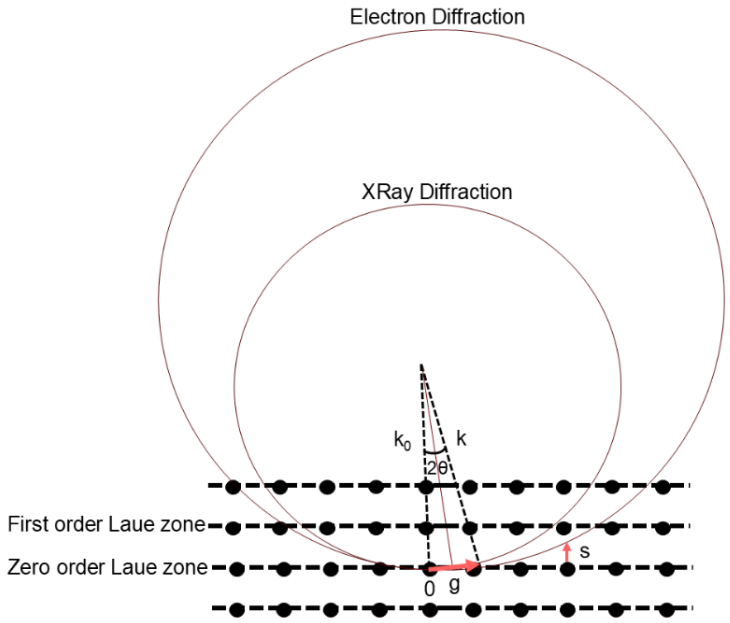

Figure 2. 6 Ewald sphere geometric construction

From a mathematical treatment of diffraction, it turns out that the Bragg law can be better expressed using a reciprocal lattice, whose vectors are normal to sets of reciprocal lattice planes and have a length equal to *1/d*, where d is the interplanar distance.

The formal mathematical description of the basis vectors of the reciprocal lattice, ***a****, ***b****, ***c**** is as follows:

$$\boldsymbol{a} *\cdot \boldsymbol{a} = 1\,;\ \boldsymbol{a} *\cdot \boldsymbol{b} = 0\,;\ \boldsymbol{a} *\cdot \boldsymbol{c} = 0 \tag{3}$$

$$\boldsymbol{b} *\cdot \boldsymbol{a} = 0\,;\ \boldsymbol{b} *\cdot \boldsymbol{b} = 1\,;\ \boldsymbol{b} *\cdot \boldsymbol{c} = 0 \tag{4}$$

$$\boldsymbol{c} *\cdot \boldsymbol{a} = 0\,;\ \boldsymbol{c} *\cdot \boldsymbol{b} = 0\,;\ \boldsymbol{c} *\cdot \boldsymbol{c} = 1 \tag{5}$$

where the bold notation indicates the vectors. Each reciprocal lattice vector can then be expressed as a linear combination of these three basis vectors, with integer coefficients *h*,*k*,*l*

$$\boldsymbol{g}_{hkl} = h\boldsymbol{a}^* + k\boldsymbol{b}^* + l\boldsymbol{c}^* \tag{6}$$

Each set of direct lattice planes can then be identified by its integer components with respect to the reciprocal basis vectors of the lattice, reported in rounded brackets as (*hkl).* The length of this vector will be the inverse of the d spacing between these planes

$$g_{hkl} = ha^* + kb^* + lc^* = \frac{1}{d_{hkl}} \quad (7)$$

Since Bragg's law states that $|k\text{-}k_0| = \frac{2\sin\theta}{\lambda} = \frac{1}{d_{hkl}}$, it is equivalent to saying that the difference between the incoming and diffracted wave vector should coincide with a reciprocal lattice vector (Laue conditions), once the reciprocal lattice is drawn according to the actual crystal orientation. This dramatically simplifies the construction of any expected diffraction pattern. It is merely a matter of constructing it as the intersection between the reciprocal lattice and the Ewald sphere. Since λ is around one hundred times greater in X-ray diffraction than in electron diffraction, the Ewald sphere for electrons is so large that, locally, it can be considered almost flat, while the corresponding scattering angles are of the order of just 1°.

If we consider the possible intersections between a large sphere and the reciprocal lattice of the crystal, we see that two possible electron diffraction patterns can be observed. A common pattern in which the spots are usually arranged in groups following large circles if the crystal is oriented in a random orientation. The other is a geometric pattern in which the spots are arranged in a two-dimensional lattice if the incoming beam direction coincides with a direct lattice vector. In the second case, the Ewald sphere is tangent to a reciprocal lattice plane and since it is almost flat it practically coincides with it. We refer to these two cases as off-zone and zone axis patterns respectively (Figure 2.7).

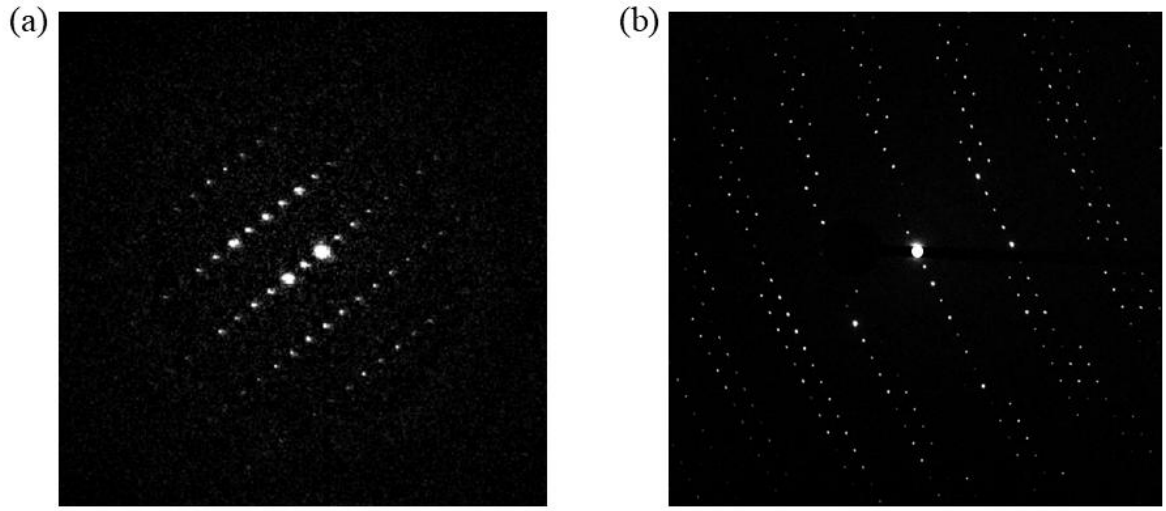

Figure 2. 7 (a) Zone axis pattern (b) off-zone axis pattern in electron diffraction

The description of the diffraction arising when a reciprocal lattice node passes through the Ewald sphere is valid only for perfect infinite crystals. In real cases, a crystal is finite and its coherent domains are reduced by crystal imperfections referred to as mosaicity. A real crystal can then be modelled with reciprocal lattice nodes that are not points but small volumes (usually elongated along the beam direction where the crystal is thinner) (Figure 2.8). We therefore also see diffraction if a reciprocal lattice point is in the proximity of the Ewald sphere.

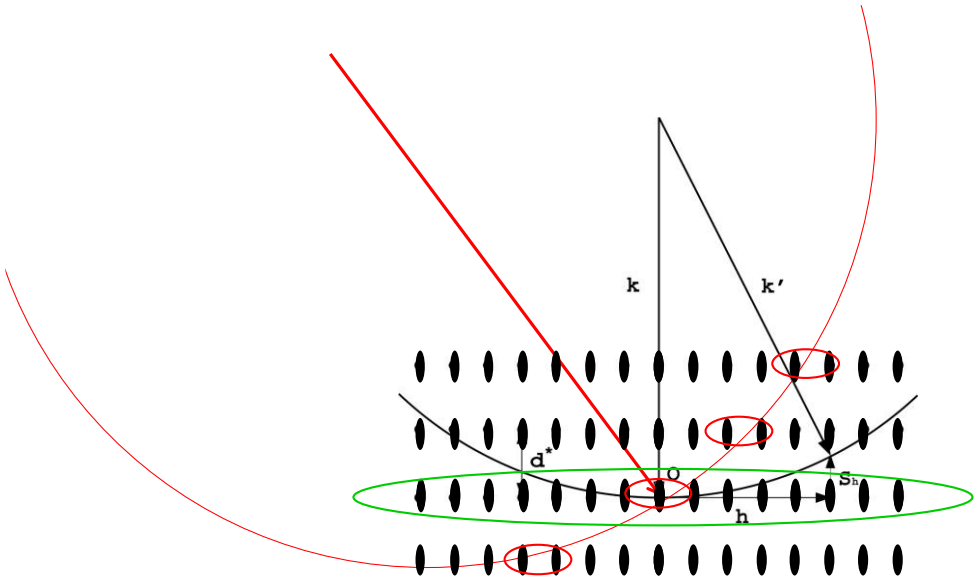

Figure 2. 8 The reciprocal lattice nodes are not discrete but elongated (black) thereby diffraction can still be observed when the nodes are close to the surface of the Ewald sphere (red)

The distance of each reciprocal lattice point from the Ewald sphere is measured with a vector as depicted in Figure 2.8 called excitation error, S_g (J. M. Zuo & Spence, 2016). The S_h value is related to the incoming wave vector as;

$$S_g = \frac{|k_0|^2 - |k_0 + g|^2}{2|k_0|} \tag{8}$$

When S_g is equal to zero the reflection is in exact Bragg condition and its intensity is in most cases at the maximum. The variation of the reflection intensity with S_g, known as the rocking curve, directly depends on the size of the coherent domain whose main limiting factor is the mosaicity (an example several rocking curves vs. excitation error is depicted in Figure 2.9).

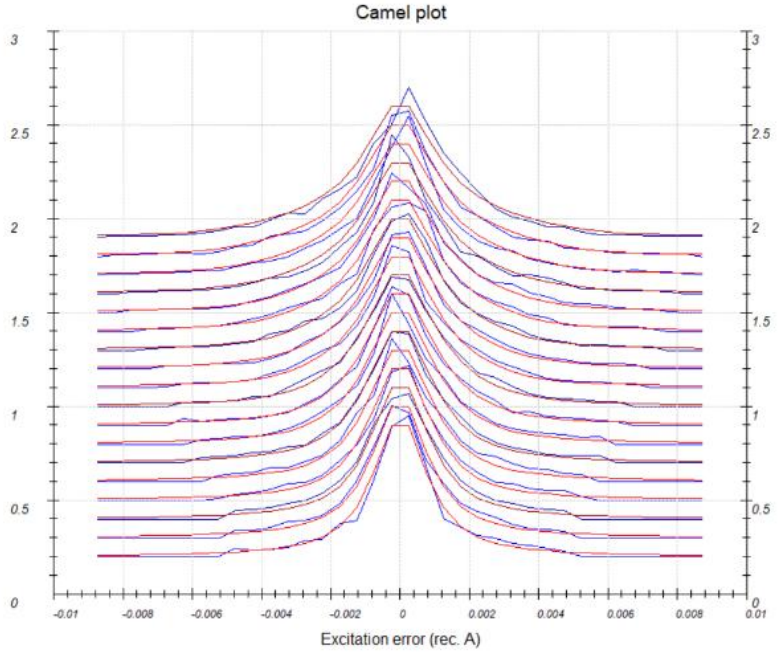

Figure 2. 9 The rocking curve or the 'camel plot' is the plot is the plot of the intensities of the reflections at different resolution vs. the excitation error on the x-axis

2.3.2. Electron Diffraction Intensities

The intensity of a reflection in electron diffraction according to the first order approximation, known as kinematical, is equal to the square modulus of the Fourier transform of the

electrostatic potential since for electrons this is the "scattering agents". This quantity is known as the structure factor. The same approximation also holds for X-ray diffraction, however in this case, since the "scattering agent" is the electron density they therefore the X-ray structure factors are different and correspond to the Fourier transform of the electron density. As described above, the combination of mosaicity and crystal size blurs the reflection intensities in reciprocal space. As a result, the measured intensity of the reflection g_{hkl} can be expressed as a function of S_g as:

$$I(g_{hkl}) = |F(g_{hkl})|^2 \, R(g_{hkl}, S_g) \tag{9}$$

where R is the rocking curve of the reflection. This makes it then clear that any diffraction data collection aiming to correctly estimate the structure factor amplitude through the reflection intensity needs to sample the rocking curve by properly scanning the reciprocal space around each reflection. Assuming we can perform such a scan, the electron diffraction analysis would be quite like any SCXRD experiment once we consider the different nature of the "scattering agent". Unfortunately, the strong interaction of electrons with matter, which allows us to measure nanocrystals, has the drawback that even for very thin specimens, that is, electrons are scattered multiple times inside the sample. This phenomenon is known as dynamical scattering in electron diffraction and can be considered negligible in X-ray diffraction. Dynamical scattering alters the simple relation between diffraction intensity and structure factors expressed by the first order approximation. An example of these effects can be seen in the Figure 2.10 below where a zone axis diffraction pattern is compared with its kinematical simulation. Therefore, if we want to use electron diffraction for solving crystal structures, we need to design data collection strategies to be able on one side to properly sample the reciprocal space and on the other to minimize the dynamical scattering.

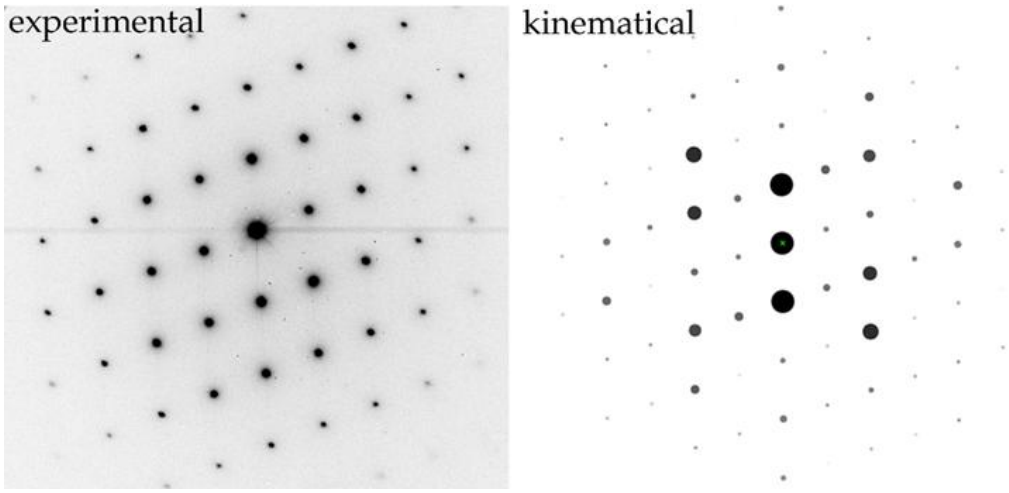

Figure 2. 10 [100] Zone axis electron diffraction pattern collected on a calcite crystal (left) and its kinematical simulation (right). Note how in the experimental pattern all the reflections have a more uniform intensity compared with the corresponding kinematical values, like if the dynamical scattering is distributing evenly the intensity between them.

2.4. 3D Electron Diffraction Data Collection Methods

Historically, before the 3D ED era, electron diffraction data were acquired by collecting single zone axis patterns using a precessed electron beam in a method known as Precession Electron Diffraction (PED) and the data collected in this way were treated as quasi-kinematical. PED was a method first proposed in 1994 by *Vincent et al.* to help reduce dynamical effects in electron diffraction (Vincent & Midgley, 1994). In PED, diffraction patterns are collected while the electron beam is precessing on a cone with a fixed vertex at the sample surface (Midgley & Eggeman, 2015) (Figure 2.12). The diffraction intensities collected in different zone axes were merged into a three-dimensional data set that was used for solving the structure in kinematical approximation (Gemmi & Nicolopoulos, 2007). This method however had some limitations. Firstly, while precession reduced the dynamical effects, the sampling of the reciprocal space, especially for low symmetry structures remained low. This type of data collection is also time-consuming since the microscopist must undergo the long and tedious process of orienting the crystal in zone axis, which is a disadvantage for beam-sensitive samples like organic nanocrystals (Gemmi & Lanza, 2019).

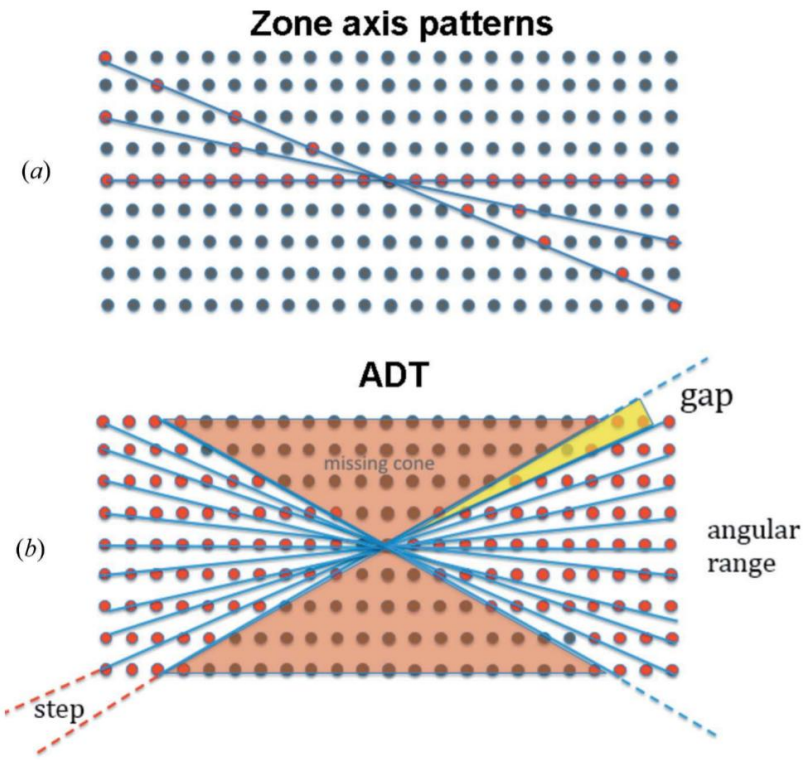

Figure 2. 11 Sketch of the reciprocal space sampling in zone axes data collection (a) PED or (b) ADT (Gemmi & Lanza, 2019)

Later in 2007, the idea of collecting both on and off-zone axis diffraction patterns without beam precession by crystal tilt was proposed by Kolb et. al. with a technique called Automated Diffraction Tomography (ADT). A stepwise tilt series was used to collect diffraction patterns with an angular step between 1º and 2º for a total angular range between 60º and 120º (Kolb et al., 2007a). Although more reciprocal space was sampled compared to the PED method making it possible to determine easily the unit cell parameters, some challenges remained such as the data gaps between tilt steps. In this case, since the reflections are not fully integrated over the excitation error their intensities were not correctly estimated and the structure solution proved to be difficult.

Mugnaioli et al. in 2009 then proposed a new method of data collection by combining the stepwise tilt in ADT with the precessed beam method PED called Precession Electron Diffraction Tomography (PEDT). PEDT solves at the same both problems of PED and ADT: due to the multiple patterns data collections increase the completeness to an angular range of

about 120º; secondly, the lack of the integration of the intensity in ADT is solved by the beam precession which allows the Ewald sphere to sweep missing gaps between the frames (Figure 2.12). The first structure solved *ab initio* using PEDT was on an inorganic salt $BaSO_4$ (Mugnaioli et al., 2009).

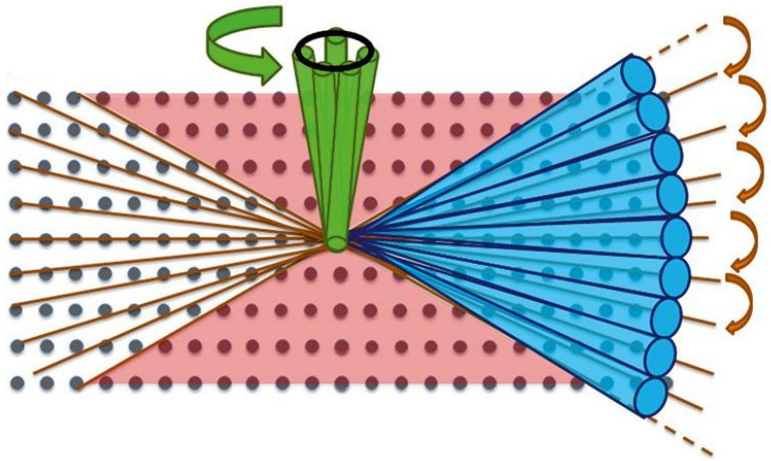

Figure 2. 12 Scheme of PEDT data collection. In blue the reciprocal space using a precessed beam in green the beam movement.

The resulting diffraction patterns collected include more reflections that would not otherwise be present in the ADT technique. The beam is precessed at an angle called the precession angle, and that corresponds to the semi-angle of the precession cone. It is usually set between 0.5º and 1.5º. PEDT can be done with almost all microscopes with a dedicated device produced by NanoMegas called Spinningstar (the old model) or Digistar P1000.

The stepwise crystal tilting method for data collection was then modified by using beam and goniometer tilts in small steps between 0.05- 0.2º and 2-3º respectively on an axis in a technique called Rotation Electron Diffraction (RED).

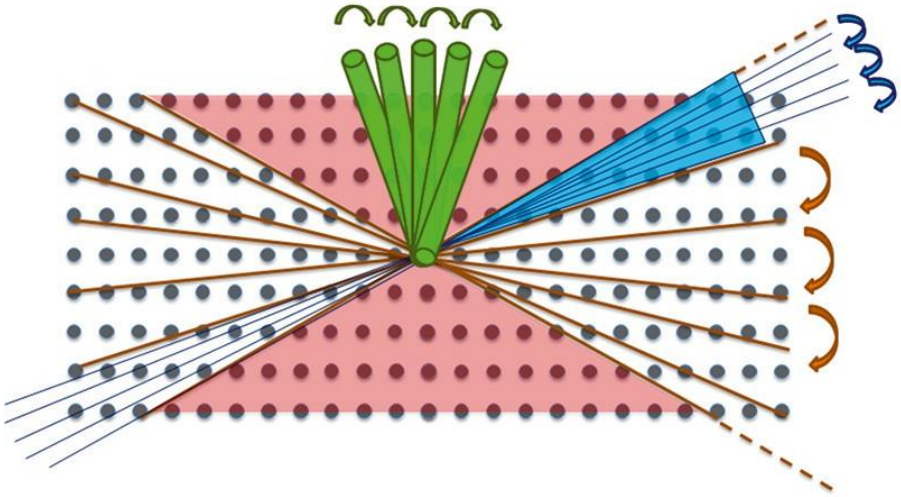

Figure 2. 13 RED data collection, in blue, is the tilt step during rotation combined with the beam tilt in green for sampling the reciprocal space

The data is collected utilizing the RED data collection program, that is used to control both the beam tilt and the rotation of the goniometer. It is not a complete integration of the reciprocal space however the small tilts between the frames minimize the missing gaps. This was a technique that could be implemented in any TEM instead of PEDT because it does not require the use of an additional device (Zhang et al., 2010).

A more recent approach to data collection involves recording diffraction patterns continuously while the crystal is rotated and was introduced by Nederlof et al, using the new Medipix detector (Nederlof et al., 2013). Subsequently, the same approach was proposed as MicroED (Nannenga et al., 2014), Integrated Electron Diffraction Tomography (IEDT) (Gemmi et al., 2015), Continuous Rotation Electron Diffraction (cRED) (Y. Wang et al., 2018) by other research groups.

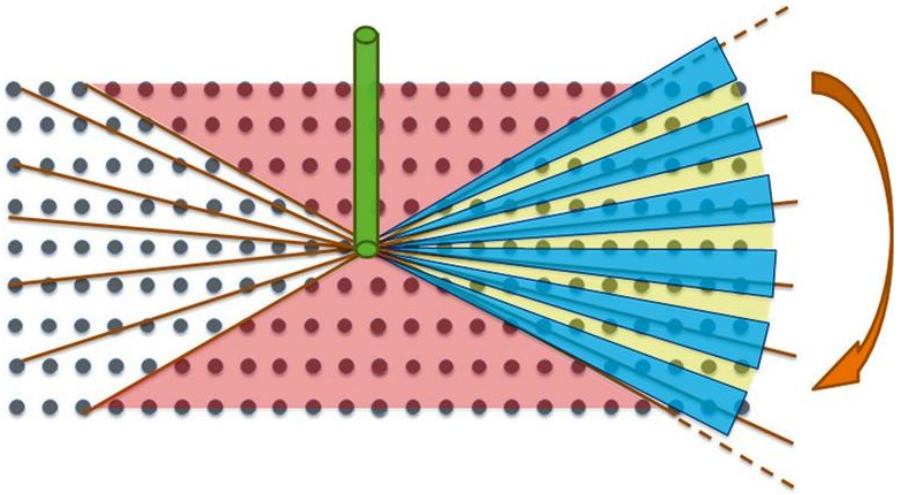

Figure 2. 14 Scheme of the cRED, with green representing the fixed electron beam. In blue is the sampled reciprocal space and in yellow are the missing gaps due to dead time of the detector.

In the rest of the thesis, we refer to this technique as continuous rotation electron diffraction or cRED. cRED as the name suggests involves continuously rotating the crystal with a stable goniometer and a fixed beam while collecting the diffraction patterns by shooting continuously with the detector which is the same method used in SCXRD data collection. By combining the speed of the goniometer with the exposure time of the detector we obtain the angular step between the frames which corresponds also to the angular integration of each frame. If the detector has a significant readout time, a missing gap is obtained between the frame which must be minimized by using a slower rotation speed (Figure 2.14). Fortunately, these days, the new detectors have high read-out rates and sensitivity with an almost negligible dead time (Gemmi & Lanza, 2019). This has made data collection fast and thereby suitable for beam-sensitive materials like organics, the subject of this thesis.

There are still some materials that are so beam sensitive for data collection using cRED leading to the loss of high-resolution data by the time the data collection is completed. A solution for this has been implemented to further push boundaries called Serial Electron Diffraction (SerialED) (Smeets et al., 2018) (Bücker et al., 2020).

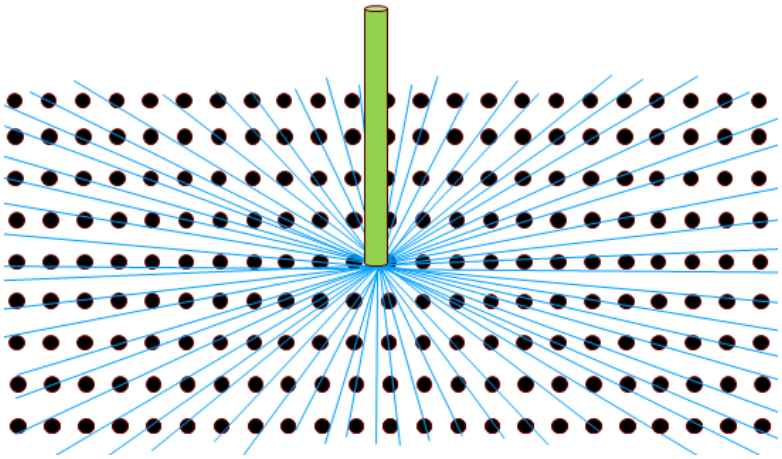

Figure 2. 15 Scheme of SerialED data collection with blue lines representing the sampling of the reciprocal space by collection of single diffraction shots of different crystals

SerialED is an adaptation of the serial X-ray Crystallography data collection method (Spence, 2017) where an automated data collection is performed on thousands of crystals randomly oriented. A single diffraction shot is acquired for each single crystal and all the collected patterns are finally merged into one data set. Therefore, even if the crystals are amorphized after a few seconds of exposure to the beam in a single shot the high-resolution diffraction data can be recorded before crystal deterioration. So far, SerialED has been used for the *ab initio* solution of materials with already known unit cell parameters (Hogan-Lamarre et al., 2024). This is because all diffraction patterns are randomly oriented which makes indexing a daunting task. A proposed approach is to combine a rotation in a small angular range with the serial sequence in order to collect small reciprocal wedges large enough for proper indexing. This method is called Serial Rotation Electron Diffraction (SerialRED) (B. Wang et al., 2019).

In this thesis, the two data collection methods used are the continuous rotation, cRED and the PEDT for Chapter 3 to 5, while preliminary work on SerialED was done in Chapter 6.

2.5. 3D ED Data Analysis and Processing

Once the diffraction patterns have been collected, the next important step is to extract the information from them by data processing. 3D ED data processing is done on the 3D reconstructed reciprocal space obtained from the collected patterns. The first step to carry out

is to find the unit cell of the investigated material by indexing the collected patterns. The software and protocol for indexing diffraction data for unit cell and space group determination used in SCXRD are adaptable for 3D ED data since the geometry follows the same principles described the Bragg's law (Gemmi et al., 2019). *XDS* (Kabsch, 2010) and *DIALS* (Winter et al., 2018) used for processing diffraction data of macro, micro molecules and inorganic compounds obtained from SCXRD can be used to process 3D ED data as well. *PETS2* (Palatinus et al., 2019a), *Redp* (Wan et al., 2013) and *ADT3* (Kolb et al., 2007b) are software specifically designed for processing 3D ED data instead. In this thesis, *Pets2* was the software of choice for data processing and analysis therefore its workflow will be discussed.

2.5.1. 3D ED Data Analysis with *PETS2*

To process 3D ED data in *PETS2*, it is necessary to know several parameters that must be included in the input file. One of these is the wavelength (λ), which differs from microscope to microscope depending on the accelerating voltage used. The type of data collection must also be specified for example whether it is cRED, PEDT or ADT (static frame) this will determine how the data is processed which is relevant for the integration of intensities step. After these parameters have been given the next step is to load the diffraction data. The diffraction patterns readable by *PETS2* are in the *.tiff* format and must be loaded sequentially specifying the rotation angle alpha (α) frame. Normally, this is easily achieved by giving the starting angle and the angular step. In the case of cRED, the angular step required is half the integration angle. The next parameter to be included is the location of the projection of the tilt axis onto the diffraction plane given by its azimuthal angle ω calculated starting from the horizontal direction. Usually, this value, which is camera length dependent, is known by the user however if for some reason it is not available a global search option can be activated to calculate it during the data processing. Another mandatory and important parameter is the value of the pixel size of the images in reciprocal space, $Å^{-1}$ (aperpixel). This value is known as calibration parameter and

allows the software to directly measure the position of the spots in reciprocal units and ultimately to determine the lengths of the reciprocal lattice vectors. It changes if we change the camera length and its values are calibrated once for all with a standard. The signal-to-noise ratio (I/δ) parameter is the threshold that determines which detected spots will be retained for indexing. It is usually set between 5-10 unless the data show quite streaking disorder when it is set to higher values to avoid interpreting as peak the diffuse scattering. Lastly, the reflection size in pixels is set. In our experiments, it is usually set to 8 pixels in diameter. The diameter should be able to contain the reflections but should not be too large to prevent overlapping. After all this information has been added to the input file the data processing can then begin.

The first step is to launch a peak search to pick up reflections that meet the threshold (I/δ) that is set in the input file with the 'Peak search' button on the menu. The central beam is masked therefore it is not included in the calculations as reflection however its position is determined in every pattern as the origin position. Figure 2.16 below is the graphical interface opened on the peak search procedure. The peak search is performed in a resolution range (max d* for peak search) selected by the user.

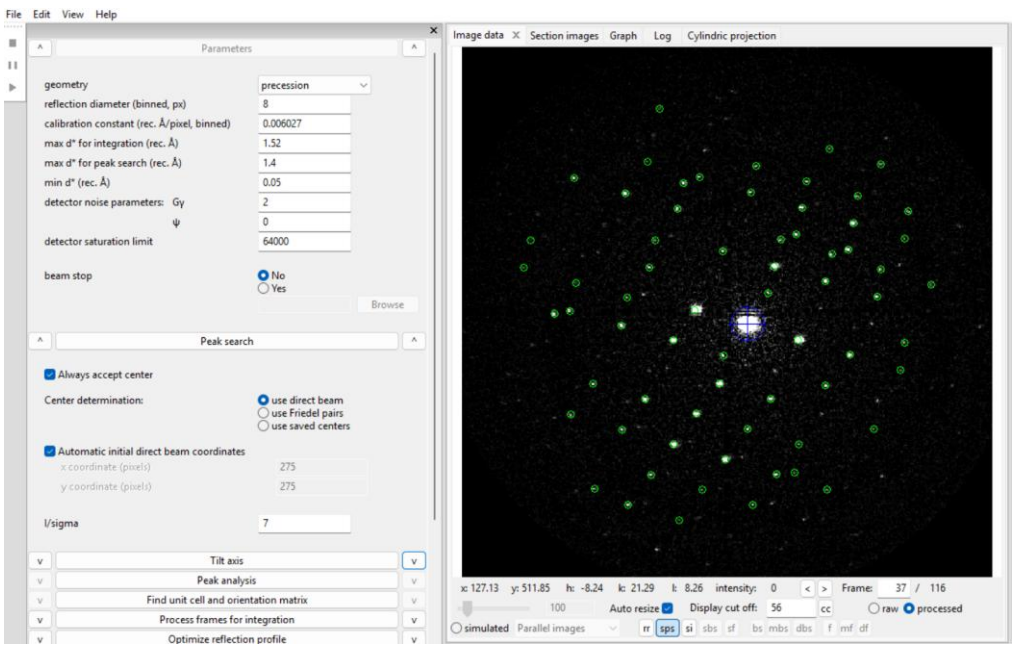

Figure 2. 16 An example of a peak search window in PETS2. The reflections picked up by the software are in the green circles based on the value of the I/sigma on the panel on the left. The central beam is masked in the blue circle and not included in the peak search and calculations. The x and y coordinates of the central beam can be calculated automatically or determined manually.

The next step is the refinement of the rotation axis azimuth ω, if already provided in the input file. If a preliminary estimation is not known, then the global search option can be activated to calculate the value of the orientation axis using the 'Tilt axis' tab. The tilt axis is refined based on the concept that it remains constant throughout the data collection. After the tilt axis is refined, the 2D cylindrical projection of the data should display sharp discrete peaks located along sinusoidal lines which can be the first indicator of a good quality data set (Figure 2.17). The following step is the peak analysis. The first step of the peak analysis is to calculate the distribution of the distance positions of the peaks identified during the peak search process.

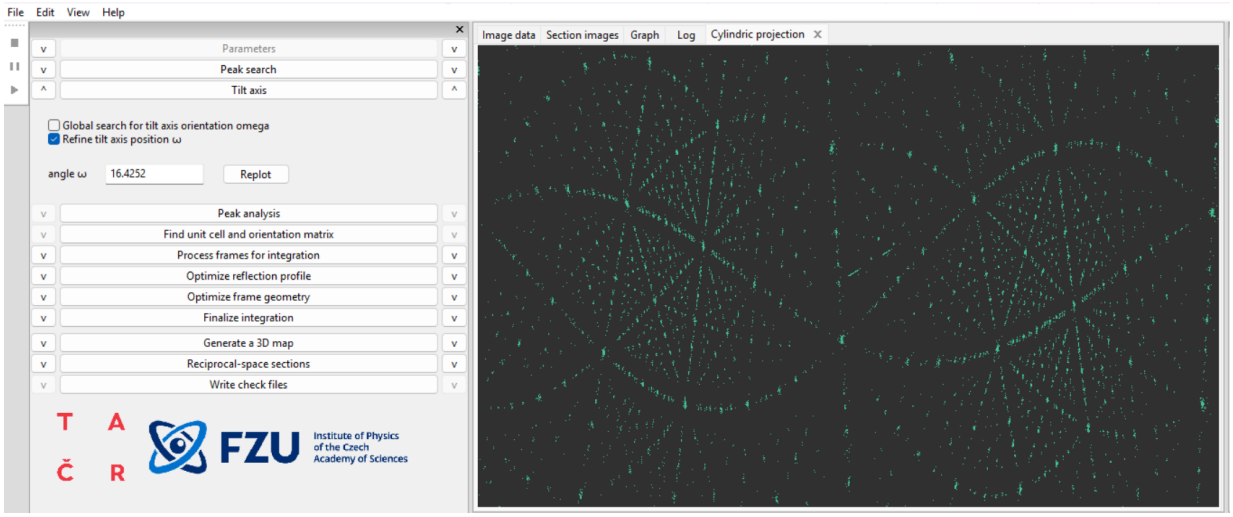

Figure 2. 17 In this window, the cylindrical projection of the data after refining the ω value.

This can then be used to analyze the inter-peak distance, displayed in red in Figure 2.18, and its derivative, displayed in green. The green graph should be a series of sharp distinct peaks which testifies that the data collection is formed by sharp well separated peaks.

Peak analysis calculates the 3D clustering of the centres of all the reflections in XYZ and serves as a step to have a proper 3D distribution of single peaks for the unit cell determination.

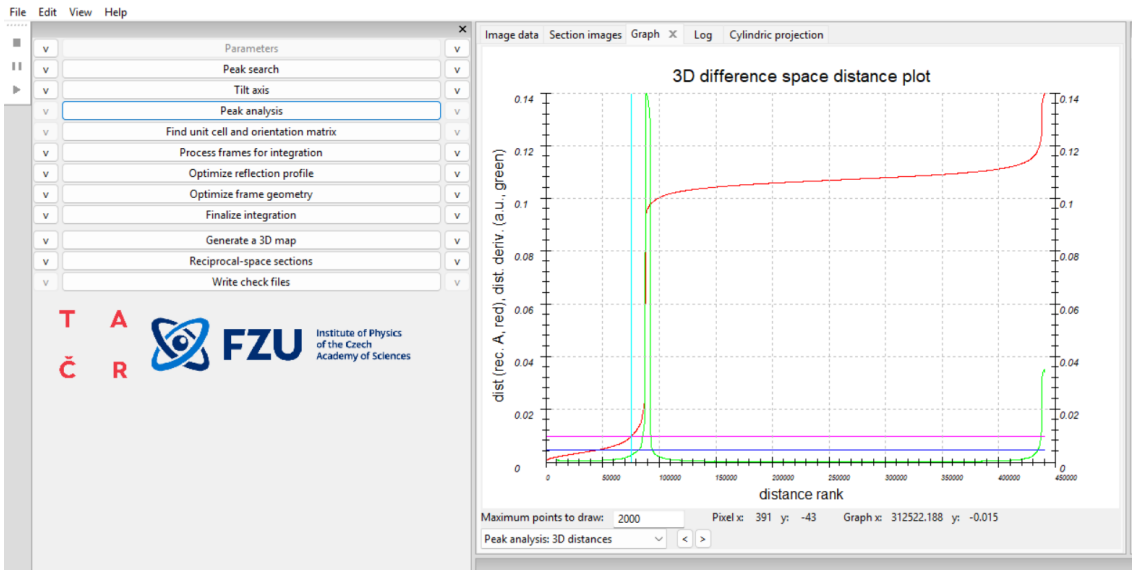

Figure 2. 18 An example of the 3D difference space distance plot where in red a smooth curve of the interpeak distance and a sharp peak is observed in green for its derivative

With all the prior steps in place, the reciprocal space can then be reconstructed which will allow us to determine the unit cell parameters and to index each collected pattern.

The unit cell parameters are defined by their reciprocal lattice basis vectors a^*, b^* and c^* together with the angles between them defined as α^*, β^*, γ^*. The software can automatically calculate the unit cell parameters and the orientation matrix from the 3D reconstruction of the peak positions. This can also be done manually by defining three reciprocal lattice plane which will correspond to the three main direct lattice directions (Figure 2.19). Once the unit cell parameters have been found, they are refined to reduce the effects of distortions in order to obtain more accurate cell parameters. In the microscope used in this thesis the accuracy in the unit cell parameters is affected by lens distortion and usually is within 1% in the parameter length and 0.5° to 1° for the angles.

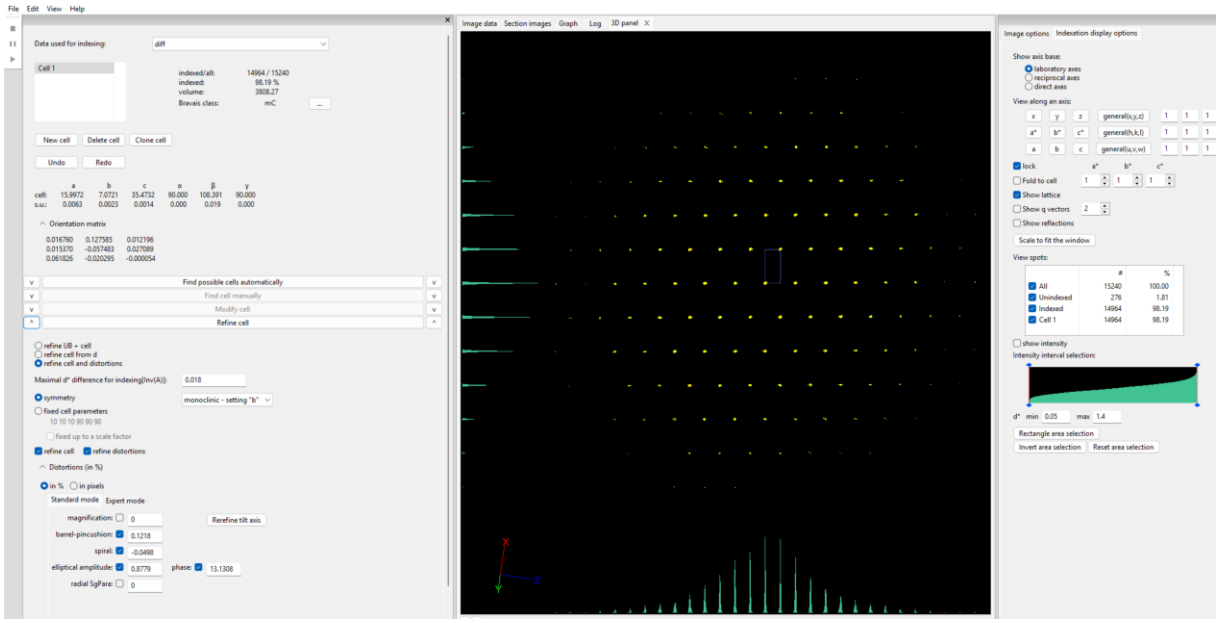

Figure 2. 19 The graphical interface of PETS2 software shows the unit cell determination step before further data processing

The next step in the data processing is the 'Process frames for integration' routine. As the name suggests, this is a crucial stage for the integration of intensities. The positions and intensity of each peak in all the frames are calculated based on the orientation matrix determined during the previous indexing step. There are two ways the integration of intensities is done, either by

using ‘sum count’; which sums the total measured intensity inside the peak area or by ‘fit profile’; where the average intensity profile of the reflections is calculated based on the strongest ones and it is then fitted to every reflection for the intensity extraction. The ‘fit profile’ is a better way for the integration especially when there are some weak or saturated reflections in some of the frames. After this process is run, it is possible to see on each frame the integrated peaks which are marked by the green circles. The gold circles are the predicted positions of the reflections that are unobserved (Figure 2.20).

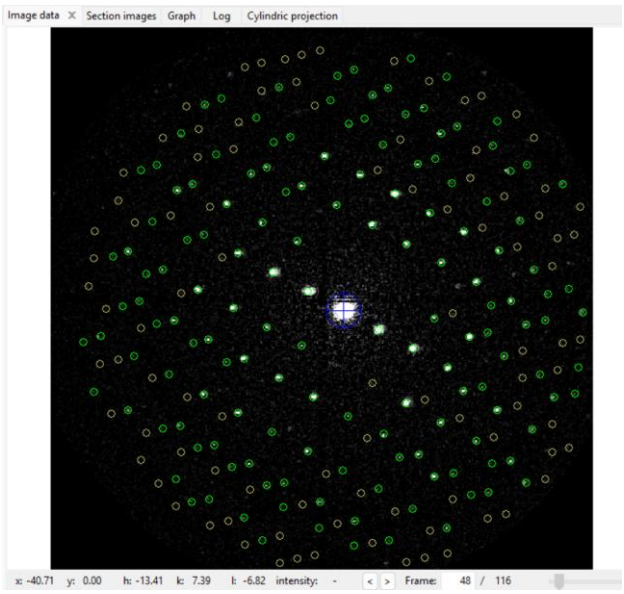

Figure 2. 20 ‘Process frames for integration’ step in the data processing with the green circles indicating observed reflections the algorithm found after the prediction and the gold circle showing the predicted position of unobserved reflections

Once the reflections are integrated in every frame, it is possible to access the rocking curve which is, as stated above, the dependence of the reflection intensities vs. the excitation error. *PETS2* at the end of the integration process directly displays the rocking curve for different resolution shells. This plot is the named camel plot for its characteristic shape in the case of PEDT.

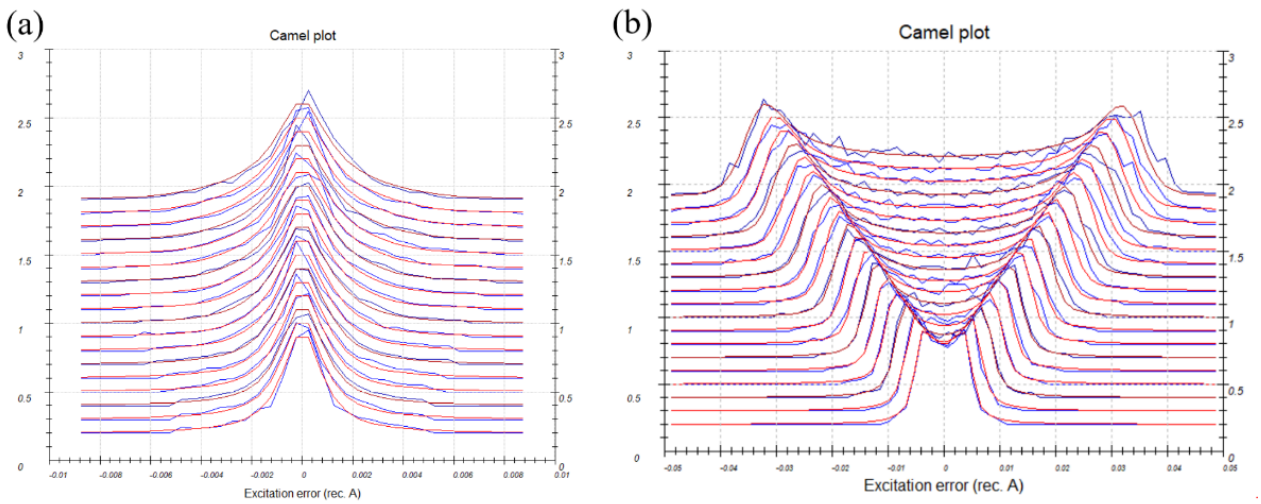

Figure 2. 21 Camel plot of (a) cRED data and (b) PEDT data with the excitation error plotted against the resolution and intensity. The red graph plots are the calculated while the blue are the experimental values

The shape of the rocking curve is directly dependent on the geometry of the experiment as displayed in Figure 2.21. For example, in cRED, a single maxima appears at $S_g = 0$ (Bragg condition) with a width that increases at high resolution due to the mosaicity. PEDT on the other hand has a camel-like plot as the resolution increases. It is as if at each resolution there are two replicas of the cRED single peak at $S_g \neq 0$ with their separation which increases with the resolution. The reason relies on the integration of the reciprocal space done with the precession of the beam. Basically, reflections at high resolution stay longer time close to Bragg condition if their excitation errors satisfy the equation,

$$|S_g| = g\ \varphi \tag{10}$$

where φ is the precession angle. This happens twice for S_g positive and negative which explains the double peak. Also, for the camel the width of the peak depends on the mosaicity.

In the plot, the calculated profiles in red and the experimental in blue in Figure 2.21 should have a similar shape and position showing an agreement which will also imply that the data is of good quality. After the plots have been calculated, the next thing is to do the optimization of

the reflection profile to give a better fit of the camel plot and ultimately improve the intensity extraction. The first step is carried out in the 'Optimize Frame Geometry' and it precisely correct the orientation of each frame allowing for the optimization of two possible tilt angle of the frame and of the central beam position to ensure the precision in the position of the reflections for the integration of the intensities. This is necessary since the crystal can have a local bending and movements of the beam position onto the crystal can probe areas of slightly different orientations. After having performed this optimization, the 'process frames for integration' should be run again to apply the corrections to the integration step. The last step for completing the integration is the 'Finalize integration' routine. At this stage, an *.hkl* output file is produced containing a list of reflections and their intensities integrated across all the frames to be treated as kinematical for the structure solution step. A file called *.cif_pets* is also generated which contains the cell parameters and other information about the experiment. A second option is present in case the user is interested in performing a dynamical refinement of the structure. This option generates additional files necessary to run dynamical refinement. In this case the integration of intensities is not performed across all the frames but is considered only frame-by-frame (Palatinus et al., 2019b). For cRED data, the frames are summed to form a series of virtual frames like a simulated PEDT integration, while the frames in PEDT are each considered as a single frame since they are already integrated in reciprocal space by the precession movement of the Ewald sphere. This generates an additional output called *pets_dyn.cif* file which is needed as input for *JANA2020* for running a dynamical refinement (Palatinus, Petříček, et al., 2015). A piece of crucial information that can be obtained after the 'Finalize Integration' step is the reflection statistics showing the figures of merit *(Rint*) for each Laue class, resolution range and the completeness of the data. The values of the *Rint* observed *Rint(obs)* in the statistics should be as low as possible and the completeness value must also be high. A first indication of the possible Laue classes can be seen from the *Rint(obs)*. Then the

space group can distinctively be determined afterwards by observing the reciprocal space sections and analysing the possible systematic absences. Sometimes it can be useful to check if the cell can be transformed into a higher symmetry one through a transformation matrix. This can be computed with *Lepage*(Carson & Bugg, 1986), using the online platform of the Computational Crystallography Toolbox (*cci*) (Grosse-Kunstleve et al., 2002) or manually.

2.6. Crystal Structure Determination

The outputs of the data processing step (unit cell parameters, the *.hkl* file containing all the reflections and their respective intensity) can then be used for the structure solution. In electron diffraction data, like SCXRD data, only the squared amplitudes of the diffracted waves (intensity) can be measured while their phases are lost, thereby, the structure cannot be directly observed. This is known as the phase problem in crystallography and all the structure solution methods try to derive *ab initio* the phases from the determined amplitudes following the kinematical approximation. Once the phases are available with an inverse Fourier transform it is possible to reconstruct the scattering quantity (the electrostatic potential for electron) which is a positive function peaked where the atoms are located. These methods are quite complex, and it is beyond the scope of this thesis to revise them, so we just list briefly the most important ones. *Ab initio* methods include Patterson, Direct Methods and Charge flipping (Oszlányi & Sütő, 2004) all methods that do not require prior crystal structural knowledge but only the elemental composition. There are non-*ab initio* methods used mainly for organic molecules that require a starting rigid body model of the molecule with an algorithm that tries to find a 3D model by varying the different positions and orientations of the molecules and in some cases allowing also some possible torsion. Typical non-*ab initio* methods include simulated annealing (Bollweg et al., 1997) and molecular replacement. Software like *Sir2019* (Burla et al., 2015) has the option for either *ab initio* or non-*ab initio* for phasing and structure solution. *Superflip* (Palatinus & Chapuis, 2007) is based on the charge-flipping algorithm, while *Shelxt*

(Sheldrick, 2015b) uses the dual space method. In this thesis, the unknown crystal structures were solved *ab initio* phasing by dual space method using *Shelxt*.

2.7. Crystal Structure Refinement

The initial structural model is a rough estimate of the real structure, which creates the need to determine more accurate atomic coordinates and other parameters such as thermal factors and partial occupancies. Crystal structure refinement is therefore necessary to obtain a more accurate model. The goal of any refinement type is to minimise the difference between the observed and the calculated intensities. Restraints can be placed on the interatomic distances, angles, planes and the geometry for aromatic rings for example. For 3D ED data, either the kinematical or the dynamical refinement can be performed.

2.7.1. Kinematical Refinement

Kinematical refinement is a least square method refinement which uses the kinematical approach that compares the calculated intensities with the measured and tries to find the best fitting. The quality of the final model is calculated using the Residual factors or the *RFactors or RValues*, where *R* calculated as follows:

$$R = \frac{\sum|F_{obs}| - |F_{calc}|}{\sum|F_{obs}|} \tag{11}$$

With F_{obs} as the observed structure factors obtained from the experimental data and F_{calc} the calculated structure factors (Giacovazzo et al., 2013). This refinement can be done in *Shelxl (Sheldrick, 2015a)* with electron wavelength and scattering factors or in *Jana2020* (Petříček et al., 2023). The initial refinement is done with only the non-hydrogen atoms together with some restraints and constraints when necessary. The hydrogen atoms are later added to the structure on a riding model before the final run of refinement. The *Rfactors* are typically high for electron diffraction datasets in kinematical refinement compared to those from SCXRD because of the dynamical effects. A good dataset very rarely reaches 15%.

2.7.2. Dynamical Refinement

Although electron diffraction data can be treated as purely kinematical, dynamical effects are strong and non-negligible compared with SCXRD (Palatinus, Corrêa, et al., 2015). Therefore, a refinement method that wants to obtain accurate structures needs to include them in the modelling of diffraction. Lukas Palatinus has implemented inside *JANA2020* software the *dyngo* package to run dynamical refinement on 3D ED data. The algorithm uses the Bloch wave approach to solve the Schrödinger equation and calculate the diffraction intensities of each frame going well beyond the first order approximation of kinematical scattering (Palatinus, Corrêa, et al., 2015).

2.7.2.1. Dynamical Refinement in *JANA2020*

The intensities calculated on the single frames (PEDT) or on the virtual frames (cRED) and the orientation matrix are previously processed by *PETS2* and are stored in the *dyn.cif_pets* file, which is the input required by *JANA2020*. During the dynamical refinement, several relevant parameters that should be optimized that are characteristic of 3D ED. Some of them are directly listed in the software tab in Figure 22.2 below. Firstly, the virtual frames used in the refinement are also referred to as zones in the software (Palatinus, Petříček, et al., 2015). All the zones are included in the calculations at the start of the refinement. In the window, there is an option to specify the type of diffraction geometry, but other parameters such as the orientation matrix, rotation semi-angle, alpha and beta are automatically loaded which are already in the input file.

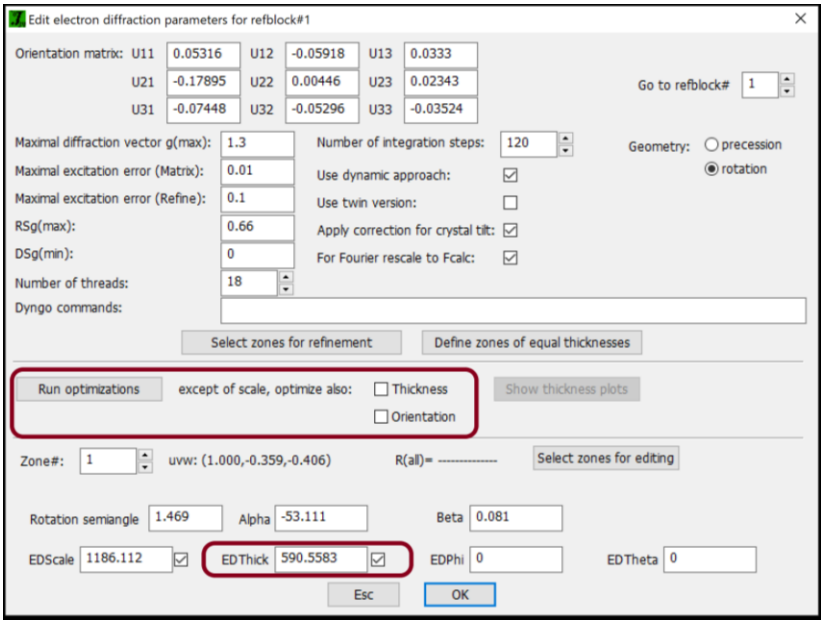

Figure 2. 22 Parameters that are refined in dynamical refinement with a set excitation error value in Jana2020

Some crucial parameters that affect the dynamical refinement calculations must be specified at the beginning of the process:

- the maximal diffraction vector *g(max)* is the maximum resolution of the reciprocal space used in the calculations and is already defined during the data reduction and remains fixed.
- the excitation error values, S_g which determines the intensities on each frame that will be used in the refinement (Palatinus, Petříček, et al., 2015). These threshold values are set with the 'Maximal excitation error (Matrix) which is the threshold for the reflections included in the structure matrix which is kept around 0.01 Å^{-1}. The second is the 'Maximal excitation error (Refine)' set at a fixed value of 0.1 Å^{-1} which limits the intensities considered in the minimization routine.
- the parameter $R_{Sg}(max)$. R_{Sg} is defined as the ratio between the excitation error and the D_{Sg} as;

$$R_{Sg} = \frac{|S_g|}{D_{S_g} + |S_g|} \tag{12}$$

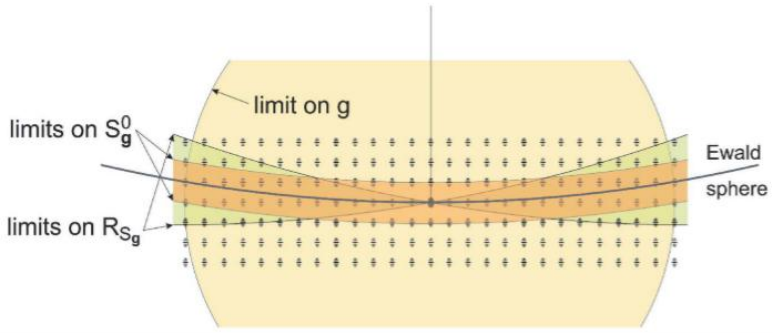

Figure 2. 23 Scheme showing the Ewald sphere with the g showing the diffraction vector whose limit is set as gmax, the Sg range in green and the R_{Sg} range whose limit is set at R_{Sg} max in Jana2020(Palatinus et al., 2013)

- the 'Number of integration steps' which is a key point for properly simulate a single pattern as a sum over several orientations, the number of steps. This is because either a PEDT pattern or a virtual frame from cRED are not steady patterns having a single orientation, but they are integrated over a continuous movement over a cone or a line of orientations respectively. The number of integration steps is the number of orientations considered for simulating this integration.

Apart from standard refinement performed on the usual structural parameters (atomic positions and occupancies, thermal parameters) in the case of dynamical refinement on 3D ED data, the thickness and the orientation of the crystal with respect to single zones are also refined. Before starting the thickness refinement, a preliminary thickness for each pattern is roughly calculated. For each pattern, a plot of the agreement factor between calculated and observed reflections vs the thickness can be displayed with the minimum corresponding to the optimal thickness for that pattern (Figure 2.24). If the data collection is of good quality this minimum should not vary much from one pattern to the other and can be used to determine the starting thickness in the refinement.

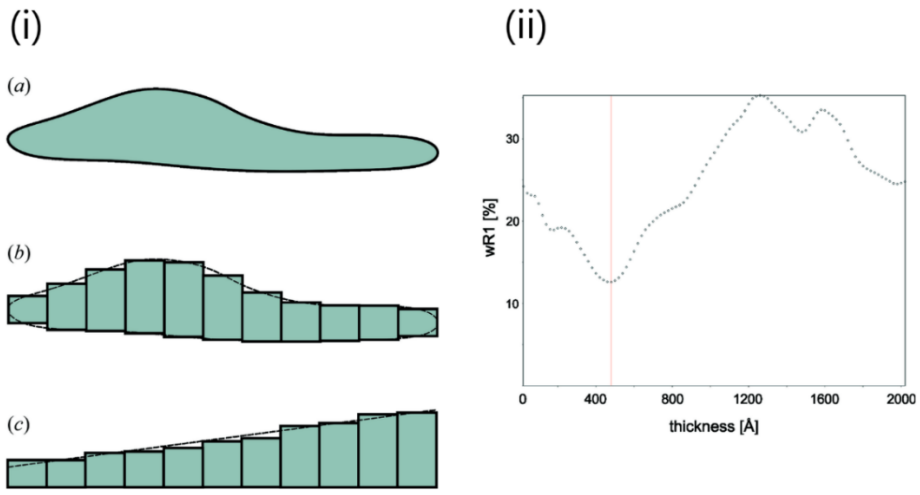

Figure 2. 24 In (i) the modelling of the intensity with irregular crystal (a) is an example of an irregular crystal (b) sorting of the crystal into small sections (c) the sections are sorted in increasing order of thickness. (ii) The thickness plot against the wR1% with the red showing the minimum thickness (Palatinus, Petříček, et al., 2015).

The orientations of the crystal, because of the tilting during the 3D ED data collection are important for the calculation of the dynamical intensities of diffraction. This can be derived from the combination of the orientation matrix and the angular position of the goniometer during the rotation. The experimentally estimated orientation matrix for each zone may be imprecise due to an unstable goniometer or a slight movement of the crystal during the data collection. There is a need then to refine and optimize the orientation matrix directly during the refinement. This if necessary is done in an optimization step in which all the other parameters are kept fixed to avoid correlation and eventually divergence of the refinement.

The resulting model from dynamical refinement is more accurate than the kinematically refined one and with better *Rfactors* typically almost half of what is observed in kinematical refinement. The difference between the results of the two types of refinement is also observable in the difference Fourier maps, where the maps after dynamical refinement have less noise. An example of how accurate and how sensitive dynamical refinement to small structural details can be found in the papers by Klar et al. and Brázda et al. in 2023 and 2019 respectively, where the authors demonstrate the possibility of determining the absolute structure of chiral organic crystals.

2.8. Sample Preparation Techniques

2.8.1. Room Temperature Sample Preparation

Most organic samples come in their dry state as powders and the simple experiment that we can perform is to prepare them and observe them at room temperature (Figure 2.25). The powder is crushed gently between two glass slides and deposited on a carbon-coated copper grid. The grid is secured onto the sample holder with the help of precision tweezers. After gently tapping the sample holder to ensure the grid is fully secured, it is inserted into the microscope.

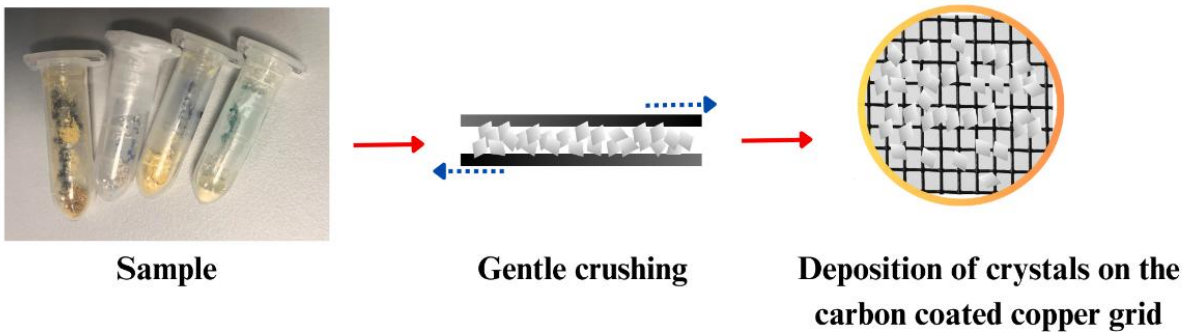

Figure 2. 25 Room temperature sample preparation workflow

2.8.2. Cryo Cooling Sample Preparation

A problem related to the data collection of organic nanocrystals can be their vacuum sensitivity. This is due to the high vacuum in the TEM (10^{-7} mBar) necessary to bring an electron beam onto the sample. Some samples experience structural collapse or dehydration under such a high vacuum, leading to amorphization (Andrusenko & Gemmi, 2022). To address the problem of vacuum sensitivity a cryo-plunging sample preparation can be used (Dobro et al., 2010). The cryo plunging sample preparation involves making a suspension of crystals in liquid and by a fast immersion in liquid ethane or nitrogen to form an amorphous/vitrified layer of iced solvent (usually water) which protects the crystals from direct contact with the vacuum (Figure 2.27). The plunge freezing done in the liquid ethane is a preferred choice because of its higher cooling capacity, it is less probable to have crystalline ice formation. A simple protocol is displayed in

Figure 2.26. First, a crystal suspension is sonicated in a sonication bath for five minutes to ensure an even dispersion of the crystals. Then a drop of suspension is placed on a TEM carbon-coated grid that has been made hydrophilic by a glow discharge plasma treatment. The grid is blotted by filter paper to produce a tiny film of liquid with the crystal inside and then is plunge-frozen in the liquid ethane. The entire procedure can be done manually or automatically in sample preparation devices called plunge-freezers like the Thermo-Fisher Vitrobot or the Leica EMPG. Once the grid is frozen, it is kept in liquid nitrogen and stored in a special cooling station that at the same time can also host the cryo-transfer sample holder. The grid is then mounted on the cryo-transfer sample holder that was already pre-cooled and rapidly inserted into the TEM column. The TEM column is pre-cooled to -180°C to avoid the sample contamination, which otherwise will work as a cold finger, and to improve the column vacuum. The standard temperature at which the sample is kept is the same as the column or higher depending on the needs of the experiment.

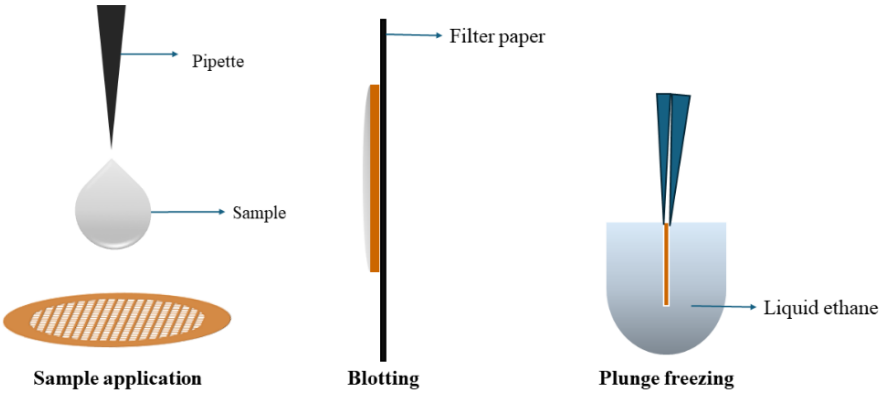

Figure 2. 26 Cryoplunging sample preparation workflow

This method of sample preparation was originally invented in cryo-EM and used for the first time in 3D ED for collecting data on protein crystals which must be in the hydrated state but experience dehydration in the TEM (Clabbers & Xu, 2020).

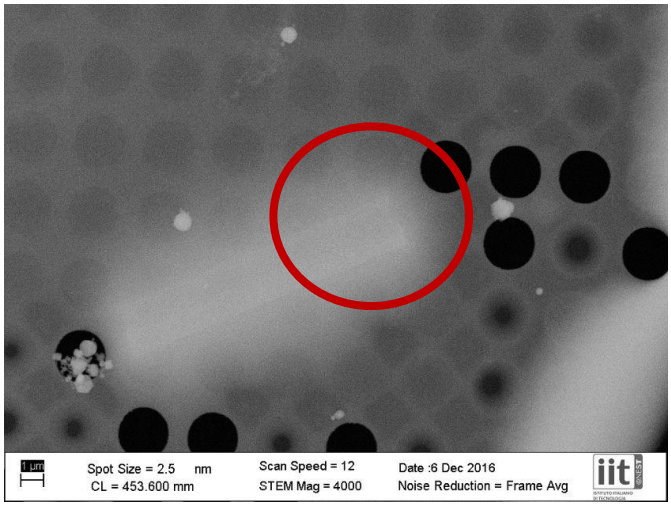

Figure 2. 27 STEM image of a crystal encapsulated by vitrified ice after cryo-plunge freezing with red showing where the data can be collected

Cooling experiments can also be done on dry samples, in this case, the samples are prepared as for a room temperature protocol. No sonication or plunging is done but cooling the column before the cryo-holder is transferred into the TEM. The cryo holder is usually cooled outside the microscope before transferring it into the microscope. This method is used for samples that deteriorate quickly after being exposed to the electron beam. This is because cooling slows down the degradation process of the sample (Andrusenko & Gemmi, 2022).

2.9. Application of 3D ED on Organic Structures

3D Electron Diffraction has been used for the determination of crystal structures of pharmaceuticals and organic small molecules. Initially, this technique was predominantly used to solve the crystal structures of inorganic materials due to the beam sensitivity of organic crystals. With the development and evolution of low-dose acquisition methods, the number of organic structures solved using 3D ED began to increase significantly (Andrusenko & Gemmi, 2022). The introduction of the first Timepix detector was a major milestone for the structure solution of organics. The Timepix hybrid detector is a fast single-count electron detector for collecting low-dose data. Work done by (Van Genderen et al., 2016) used the first Timepix detector to solve the structures of carbamazepine and nicotinic acid. The goal was to compare the resulting statistics with those solved after collecting data using the CCD detector. They observed that the sensitivity of the Timepix detector to diffraction signals was ten times greater than the traditional CCD and had a higher readout rate. 3D ED was also validated by comparing the structures of teniposide, paracetamol and biotin obtained from 3D ED with those from literature obtained using SCXRD (Bruhn et al., 2021). 3D ED played an important role in determining the crystal structure of orthocetamol, a well-known molecule. Orthocetamol is an anti-arthritic drug and a regioisomer of paracetamol which was first reported in 1876. Yet, its crystal structure was not solved until 2019, when *Andrusenko et al*. approached the problem using 3D ED. This is because orthocetamol crystallizes as agglomerated 'quadrilateral platelets' which are a very tiny intergrowth of twinned domains. This posed a problem when the SCXRD structure solution was attempted (Andrusenko et al., 2019). The identification of different polymorphs that can only be present in submicron sizes is another advantage of 3D ED for crystallography in the pharmaceutical world. δ-Indomethacin is one of the many polymorphs of indomethacin and was reported more than 50 years ago (Borka, 1974) however its crystal structure was not reported until 2021. Both *(Andrusenko et al., 2021; Lightowler et*

al., 2021) solved the crystal structure of δ-Indomethacin independently by 3D ED. This is because δ-Indomethacin forms crystals with hairlike morphology after crystallization which are too thin for SCXRD characterization.

Olanzapine is an antipsychotic drug with 60 polymorphs, counting also hydrates and solvates, but only four anhydrous forms are known. While form I, II and IV are known, form III of had been difficult to isolate and up to now could only be synthesized in phase mixtures with two other phases (Reutzel-Edens & Bhardwaj, 2020). The Form III had not been reported until recently *Anyfanti et al.* in 2024 were able to identify all three phases present in the phase mixtures. The unit cell parameters of form I were found, and the crystal structures of the other two phases present were solved by 3D ED with form III being the unreported structure (Anyfanti et al., 2024) All these successes have encouraged us to use the same technique to investigate the crystal structure of other organic nanocrystals.

The incredible development of 3D ED has had many commercial fallouts. Two different companies have already introduced to the market dedicated electron diffractometers capable of collecting 3D ED data in an optimized way. In 2022, Rigaku introduced its first dedicated electron diffractometer known as the XtaLAB synergy-ED. It operates with an accelerating voltage of 200 kV and uses the *CrysAlis Pro* software used also for SCXRD for cRED data collection, automated data processing and structural analysis (Ito & Yamano, 2022). Cryo cooling was also included which makes data collection on beam-sensitive materials possible. Later, in 2023, Eldico Scientific also introduced another electron diffractometer with a 160 kV accelerating voltage and features a horizontal beam of 40nm diameter in imaging and between 200 nm and 1000 nm beam size in diffraction mode. STEM is used for low-dose crystal search and cRED data collection, ideal for data collection on beam-sensitive materials. Additionally, it is equipped with a highly stable goniometer that reduces the movement of the crystal during rotation (Simoncic et al., 2023).

CHAPTER 3

Test on the accuracy of 3D electron diffraction on round-robin samples

3.1. Introduction

3D ED is still a growing field therefore, assessing how reproducible and accurate its results are still a debated topic. For this reason, the NanED (Electron Nanocrystallography) project conducted a round-robin experiment on unknown samples to be carried out blindly between seven laboratories. As a NanED PhD student, I was involved in characterising the samples that I report here. The round robin was implemented by giving to all labs three samples in the form of powder, without any prior information on them, including their chemical composition. The data collection was performed using different microscopes (Table 3.1) and at different laboratories within the consortium. Each of the labs had a different experimental setup for 3D ED data collection and software for data processing and structure solution. The results obtained from the analysis were compared after with the structure obtained on the same samples using SCXRD.

TEM	Accelerating voltage (kV)	Technique	Detector	Illumination
Zeiss Libra 120	120	PEDT/CRED	Timepix	NED
Fei Tecnai G2	200	EDT	FEI Eagle	SAED
Fei Tecnai G2 20	200	PEDT/CRED	Medipix3	NED
Fei Tecnai F30	300	PEDT	Ultrascan4000	NED
Jeol 2100	200	CRED	Timepix	SAED
Jeol F200	200	PEDT	Medipix3/Rio16	NED
Jeol F200	200	CRED	Medipix3	SAED

Table 3. 1 All the instruments and their respective parameters were used for data collection on the round-robin samples. Highlighted in red is the setup used in our laboratory in IIT with

the Zeiss Libra 120 TEM having an accelerating voltage of 120kV and a Timepix hybrid detector.

The samples consisted of two inorganic and one organic material. The crystal structures of these samples are already known, but the project aimed to compare the statistics obtained after the crystal structural analysis with the different instruments. In this chapter, focus will be placed on applying 3D ED on the crystal structure solution of these samples; natrolite, epidote and ibuprofen using the Zeiss Libra 120 TEM which is the instrument used in our lab. The unit cell parameters obtained were compared to those from SCXRD reference data. The SCXRD reference data was collected and analyzed from the same batch of samples using a Rigaku XtaLAB Synergy with Mo source at the Crystallography and Materials Sciences Laboratory (CRISMAT) in France. A summary of the outcomes of the round-robin experiment from the other labs will be discussed at the conclusion of the chapter.

3.2. Methodology

The two inorganic samples (natrolite and epidote) were obtained by crushing the large crystals seen in Figure 3.1 and Figure 3.4. to form poweder. The powders, were then diluted with isopropanol, after which a drop was deposited onto the grid and left to dry. It was then transferred to the microscope and data was collected at room temperature. Energy Dispersive X-ray (EDX) spectroscopy was performed on the two inorganic samples to discover their elemental composition. The organic sample also arrived in a powder form and was first prepared using the room temperature sample preparation protocol discussed in Chapter 2. However, due to the beam and vacuum sensitivity of the crystals, the cryo sample cooling protocol for dry samples listed in Chapter 2 was implemented to address it. For all the samples, STEM mode was used for crystal search and data was collected using PEDT and cRED with a NED illumination with a beam size of approximately 150 nm. PEDT was collected with a precession angle of 1° using a tilt step of 1° at an exposure time of 1 second. For the cRED,

the data was collected at a 0.5° tilt step with an exposure time of 450 ms. The best datasets were used for the crystal structure solution and refinement (kinematical and dynamical).

3.3. Epidote ($Ca_2Al_2(Fe^{3+};Al)(SiO_4)(Si_2O_7)O(OH)$)

The first sample analyzed was a mineral and inorganic material called epidote, which originated from Val d'Ossola, located in Italy. The epidote crystal structure has a monoclinic space group of $P2_1/m$. It contains 19 atoms in the asymmetric unit, with atomic species; Si, Al, Ca, Al/Fe, O and H.

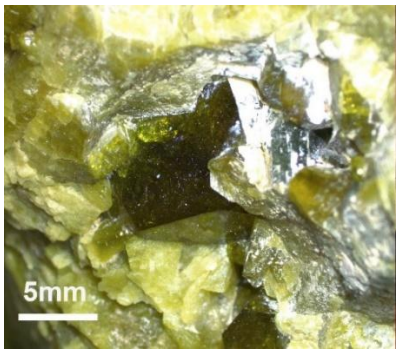

Figure 3. 1 An image of the epidote crystal originating from Val d'Ossola (Italy) used for the round-robin crystal structure analysis

For this sample, the goal was not only to solve the crystal structure using 3D ED, but also to see if it is possible to directly detect and refine the position of the H atom in the structure. In most crystal structures, each atomic site is occupied by one atom, however, in some situations, it can be occupied by two different atom types known as mixed occupancy. This is the case for epidote which has an atomic site with mixed occupancy between the Al and Fe. Therefore, another goal for this sample was to see if by using 3D ED, the occupancy of both atoms at the site can be refined and the corresponding ratio be determined.

The cRED data collection on the sample was successful, with the crystals remaining stable throughout a total angular range of 120°. The data were processed using *PETS2,* after which the cell parameters obtained were a= 8.8618(3) Å, b=5.6237(4) Å, c=10.1104(4) Å with a beta angle of 115(14)° and a volume of 455.49(6)Å^3 which is comparable to what was obtained from SCXRD where a=8.8947(10) Å, b=5.6248(10) Å c=10.1562(2) Å with β=115.40(11)°.

The final data processing statistics showed a maximum resolution of 1.3 Å, completeness of 89% and *Rint(obs)* of 22.96% for the Laue class 2/*m*. The space group was determined to be monoclinic $P2_1/m$ by examining the reciprocal space sections in Figure 3.2. which is the correct space group.

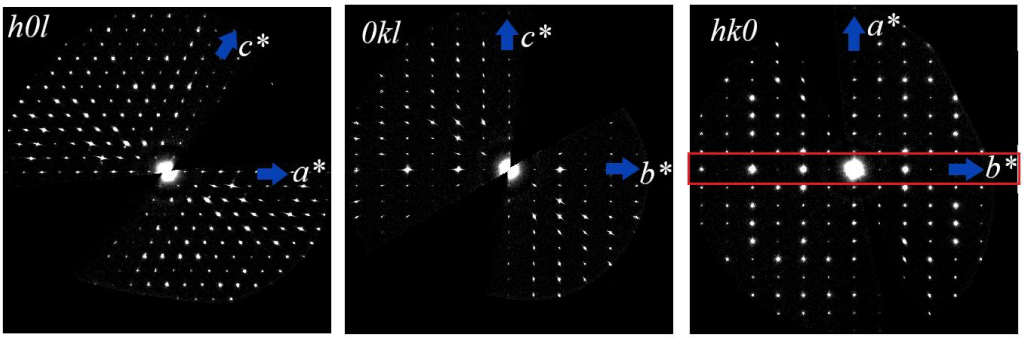

Figure 3. 2 Reciprocal space sections showing the main crystallographic directions in blue of epidote data

The structural model of epidote was then obtained by *ab initio* by direct methods using *Sir2019* with all the correct positions of the non-hydrogen atoms. The chemical composition for the direct methods attempt was estimated based on EDX data. The next step was to refine the structure which was initially done without the H atom. For the kinematical refinement, the H atom was not detected in the Fourier difference maps. The H atom was added automatically and refined kinematically in a riding model obtaining a final *RValue* (R_{obs}) of 29.02% with a goodness of fit of 4.81. On the other hand, in the dynamical refinement, a residual peak was observable directly from the calculated Fourier difference maps approximately at a 1 Å distance from the oxygen, O8 after the initial refinement run without H atoms. This was clear evidence of the H atom which was added to the structural model, and its position was refined. In addition, the mixed occupancy of the Al/Fe was refined and was determined to be 0.66 to 0.34 with a ratio of 2:1 which is consistent with what was obtained from SCXRD (0.67/0.33) as seen in List 3.1. The results after dynamical refinement are seen in Table 3.2, giving a final *RValue* (R_{obs}) of 12.6%.

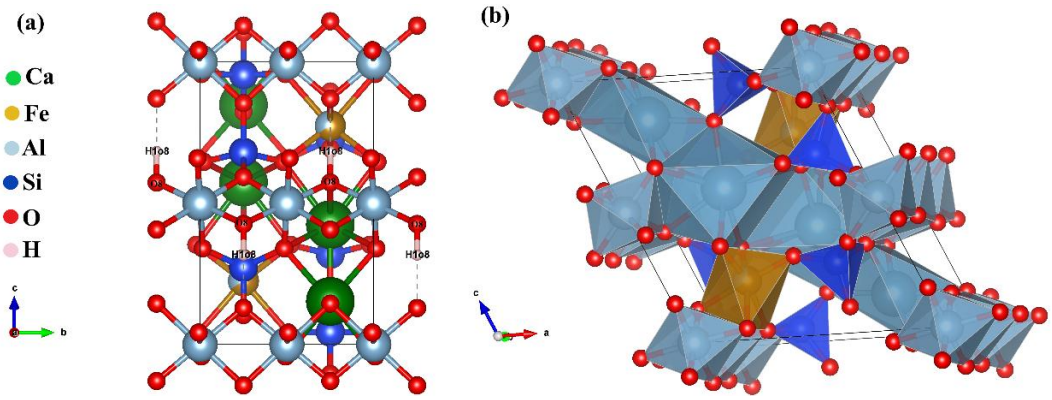

Figure 3. 3 On the left is the atomic arrangement of epidote when viewed along the a direction while on the right is the tetrahedral coordination of Ca, Fe, Si and Al with the O in the unit cell

The final model can be seen in Figure 3.3 and in List 3.1 all the atomic positions, atomic displacement parameters (ADPs) and occupancies are noted.

Crystal data	
Chemical formula	$Al_2Ca_2FeH_2O_{13}Si_3$
M_r	484.2
Crystal system, space group	Monoclinic, $P2_1/m$
Temperature (K)	293
a, *b*, *c* (Å)	8.8618 (3), 5.6237 (4), 10.1104 (4)
β (°)	115.313 (14)
V (Å^3)	455.49(6)
Radiation type	Electron, λ = 0.0335 Å
Data collection	
Data collection instrument (TEM)	Zeiss Libra 120
Data collection type	PEDT
Precession angle(°)	1
Angular Range (°)	120
Angular step	1
Beam size (nm)	≈150
Measured, independent and observed [$I > 3\sigma(I)$] reflections	12213, 3585, 1671
(sin θ/λ)max (Å−1)	0.651
Kinematical Refinement	
R(obs), wR(all), S	0.2902, 40, 4.81
No. of reflections	1024
No. of parameters	55
Dynamical Refinement	
R(obs), wR(all), S	0.127, 0.259, 2.11
No. of reflections	3585
No. of parameters	177

Table 3. 2 Results after both kinematic and dynamical refinement of the crystal structure of epidote

Atoms	x	y	z	Uiso*/Ueq	Occ.
Ca1	−0.7589 (8)	0.25	−0.1527 (4)	0.0019 (9)*	1
Fe1	−0.2951 (9)	−0.25	−0.2252 (5)	0.0050 (16)*	0.66(4)
Al1'	−0.2951 (9)	−0.25	−0.2252 (5)	0.0050 (16)*	0.34(4)
Ca2	−0.6059 (9)	0.25	−0.4246 (5)	0.0103 (11)*	1
Si1	−0.1858 (11)	−0.75	−0.3191 (6)	0.0017 (9)*	1
Si2	−0.3221 (12)	0.25	0.2735 (6)	0.0017 (9)*	1
Al1	−0	−0	−0	0.0019 (13)*	1
Si3	−0.3327 (12)	0.25	−0.0440 (6)	0.0025 (13)*	1
Al2	0	0	−0.5	0.0020 (13)*	1
O1	−0.0429 (18)	−0.75	−0.1447 (10)	0.0052 (18)*	1
O2	−0.5079 (19)	0.25	−0.1756 (10)	0.010 (2)*	1
O3	−0.2341 (12)	0.0077 (11)	−0.0423 (7)	0.0066 (14)*	1
O4	−0.0698 (18)	−0.75	−0.4069 (10)	0.0050 (18)*	1
O5	−0.0498 (16)	−0.25	−0.1291 (9)	0.0015 (18)*	1
O6	−0.2085 (12)	0.4848 (11)	0.3404 (7)	0.0055 (12)*	1
O7	−0.2995 (12)	−0.5215 (11)	−0.3533 (7)	0.0059 (12)*	1
O8	−0.9209 (17)	0.25	−0.5735 (9)	0.0051 (19)*	1
O9	−0.3642 (18)	0.25	0.1043 (10)	0.008 (2)*	1
O10	−0.522 (2)	−0.25	−0.3057 (11)	0.014 (2)*	1
H1o8	−0.917 (10)	0.25	−0.683 (5)	0.0061*	1

List 3. 1 Fractional atomic coordinates and isotropic or equivalent isotropic displacement parameters of epidote

3.4. Natrolite ($Na_2Al_2Si_3O_{10}·2(H_2O)$)

Natrolite is the next inorganic sample that was analyzed in the round-robin experiment. Natrolite is a mineral whose crystals were sourced from Marianska Skala, Usti nad Labem, Czechia seen in Figure 3. 4 below. It is part of the zeolite family made up of a 3D framework of $(SiAl)O_4$ with Na and coordinated water. It crystallizes in an orthorhombic space group *Fdd*2, with its asymmetric unit containing 12 atoms. Although it has an orthorhombic symmetry it shows a pseudotetragonal symmetry. Therefore, since no knowledge of the sample

was given initially, the task for this sample was to see if it was possible to determine the correct space group after the data collection and analysis using 3D ED. The crystal structure contains Si and Al which are close in atomic weight that are so very difficult to distinguish based only on their atomic scattering factor. Therefore, the second task is to determine the correct positions of Al and Si in the crystal structure, exploiting the correct distance with the oxygens in their tetrahedral coordination which is significantly different. Since the framework contains coordinated water, naturally another thing to do will be to see if it is possible to identify all the H atoms directly during the structure solution or in the Fourier maps during the refinement. Finally, natrolite is non-centrosymmetric, so we were asked to investigate how sensitive the data will be for determining the absolute structure using dynamical refinement.

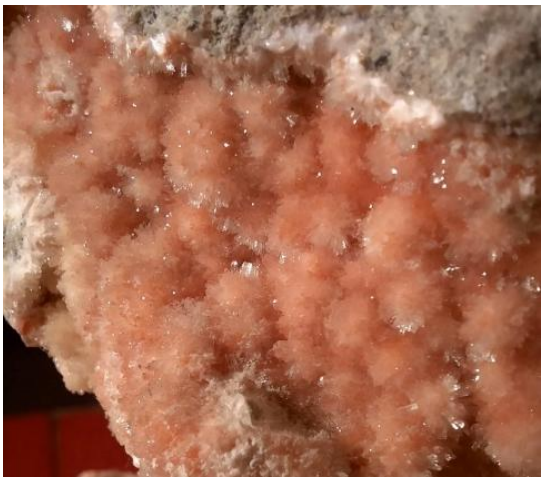

Figure 3. 4 An image of the natrolite crystal originating from Marianska Skala (Czechia)

During the data collection, the sample did not show any significant signs of beam sensitivity, which allowed for a total angular range of 114° using PEDT. The data were then processed and indexed with an orthorhombic unit cell having a=18.8278(10) Å, b=18.667(3) Å, c=6.6414(10) Å which is very close to what was observed in SCXRD where a=18.6323(3) Å, b=18.2877(2) Å c=6.5831(10) Å. The results obtained after the final integration in *PETS2* showed an *Rint(obs)* of 19.14% for the *mmm* Laue class. The possible space group was assigned as orthorhombic *Fdd*2 when the reciprocal space sections (Figure 3.5) were carefully examined.

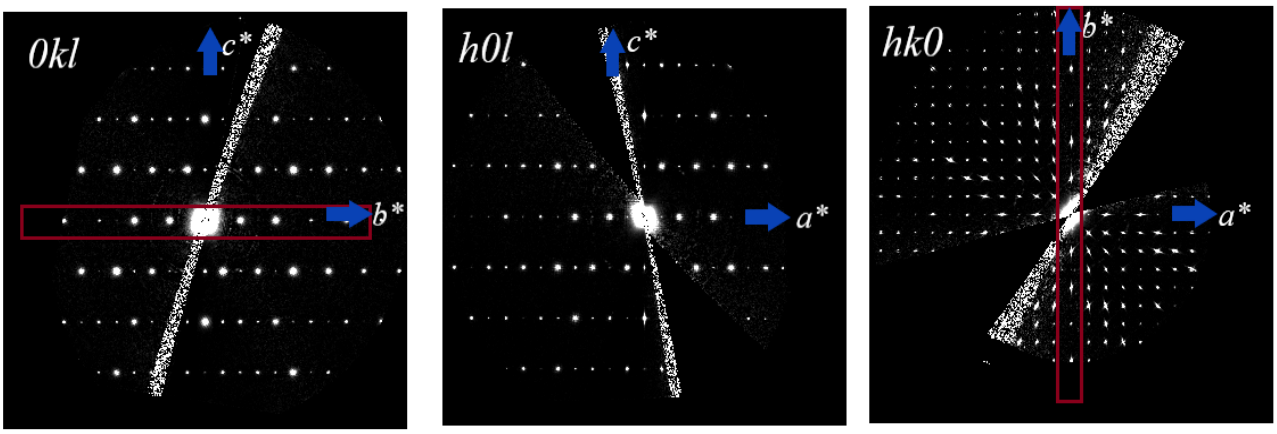

Figure 3. 5 Reciprocal space sections showing the main crystallographic directions for natrolite data

With all the information needed for the next step, the structural model was obtained with the location of all the non-hydrogen atoms by structure solution with direct methods using *SIR2019* solved in the assigned space group. The positions of Si and Al were confirmed based on their distance from the O atoms measured to be approximately 1.67 Å and 1.73 Å respectively. The peaks observed in the calculated positive difference Fourier maps after dynamical refinement were assumed to be signals of the H of the water molecules, based on their distances from the O atom which occupies the Na channels. Based on this, the H atoms were added to the structure and their positions were refined in the step of the final refinement. In Table 3.3 we obtain a kinematical refinement *RValue* (R_{obs}) of 19.26% which was more than halved at 9.42% after dynamical refinement. Remarkably it seems that dynamical refinement is super sensitive to the chirality of inorganic structure. By the handiness of the structure in dynamical refinement the *RValue* (R_{obs}) increases by 6%. The final model can be seen in Figure 3.6 with the different coordinations of Si, Al and Na with O.

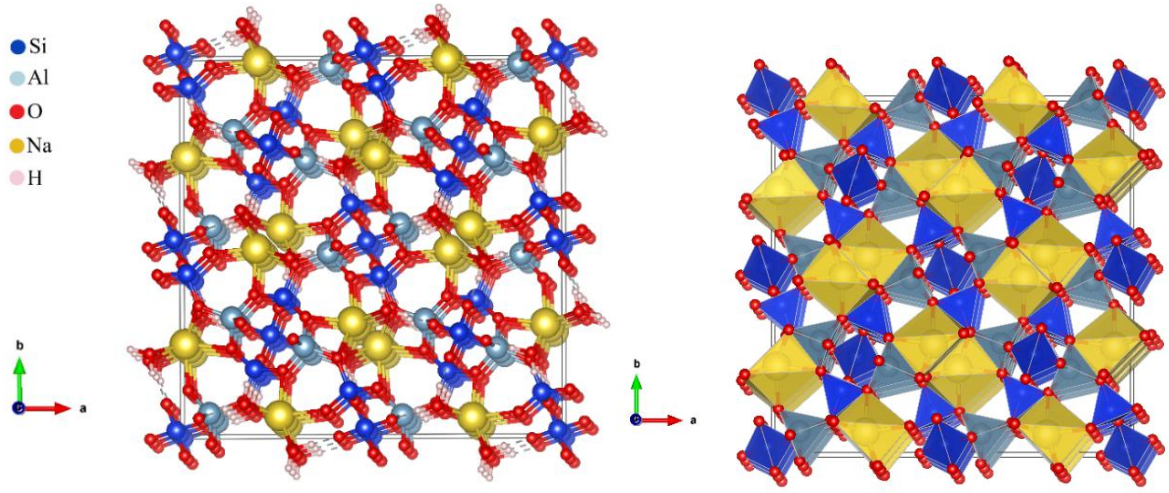

Figure 3. 6 On the left is the atomic arrangement of natrolite when viewed along the c direction while on the right is the coordination of Al, Si and N with O in the crystal structure

Crystal data	
Chemical formula	$Na_2Al_2Si_3O_{10}\cdot 2(H_2O)$
M_r	304.2
Crystal system, space group	Orthorhombic, *Fdd*2
Temperature (K)	293
a, *b*, *c* (Å)	18.8278 (10), 18.667 (3), 6.6414 (10)
V (Å^3)	2334.2 (5)
Radiation type	Electron, λ = 0.0335 Å
Data collection	
Data collection instrument (TEM)	Zeiss Libra 120
Data collection type	PEDT
Precession angle(°)	1
Angular Range (°)	114
Angular step	1
Beam size (nm)	≈150
Measured, independent and observed [$I > 3\sigma(I)$] reflections	24010, 4356, 2086
(sin θ/λ)max (Å^{-1})	0.667
Kinematical Refinement	
R(obs), wR(all), S	0.1926, 0.3253, 3.48
No. of reflections	1281
No. of parameters	39
Dynamical Refinement	
R(obs), wR(all), S	0.0942, 0.189, 1.72
No. of reflections	4356
No. of parameters	151
Absolute structure	568 of Friedel pairs used in the refinement

Table 3. 3 Results after both kinematic and dynamical refinement of the crystal structure of natrolite

In List 3.2 all the atoms with their atomic coordinates, occupancies and ADP can be seen. On List 3.3 are the hydrogen bonding distances and geometry between the H and O atoms with a distance 0.96 Å.

Atoms	x	y	z	Uiso*/Ueq	Occ.
Si1	0.5	0	−0.3847 (5)	0.0009 (10)*	1
Si2	0.53794 (13)	−0.0952 (2)	−0.0068 (4)	0.0033 (6)*	1
Al1	0.59413 (14)	0.5376 (2)	0.7384 (4)	0.0011 (7)*	1
O1	0.4626 (2)	−0.1004 (4)	0.1248 (7)	0.0099 (11)*	1
O2	0.5231 (2)	−0.0683 (4)	−0.2385 (7)	0.0145 (11)*	1
O3	0.5683 (2)	−0.1808 (4)	−0.0150 (7)	0.0080 (10)*	1
O4	0.5688 (2)	0.0219 (4)	−0.5161 (7)	0.0121 (11)*	1
Na1	0.71925 (19)	0.4707 (4)	0.4853 (7)	0.0167 (10)*	1
O5	0.5980 (3)	−0.0421 (4)	0.0958 (7)	0.0142 (12)*	1
O6	0.5603 (3)	−0.1926 (5)	−0.5135 (10)	0.0307 (14)*	1
H1o6	0.6172 (15)	−0.196 (3)	−0.579 (4)	0.023 (8)*	1
H2o6	0.554 (2)	−0.129 (4)	−0.440 (6)	0.067 (16)*	1

List 3. 2 Fractional atomic coordinates and isotropic or equivalent isotropic displacement parameters of epidote

Hydrogen-bond geometry (Å, °)

D—H···*A*	*D*—H	H···*A*	*D*···*A*	*D*—H···*A*
O6—H1*o*6···O4^{xvii}	0.96 (3)	1.98 (3)	2.897 (10)	159 (2)
O6—H2*o*6···O2	0.960 (10)	2.113 (9)	3.015 (13)	156.1 (6)

List 3. 3 Hydrogen bonding present in the natrolite with their respective distances

3.5. S-Ibuprofen ($C_{13}H_{18}O_2$)

The last sample for analysis in the series of experiments was ibuprofen which is a well-known pharmaceutical molecule with anti-inflammatory properties. Ibuprofen is a chiral molecule with two enantiomers; S and R . They can form a racemic crystal which crystallizes in the space group of $P2_1/c$ or, if crystallized as pure enantiomers, they form a chiral crystal structure in the non-centrosymmetric chiral space group $P2_1$ (Freer et al., 1993).

The initial attempt at data collection was not successful, since the crystals were sublimating in the vacuum which was a clear indication of vacuum or beam sensitivity. As a result, the first task for this sample was to address the problem of beam and vacuum sensitivity which is very common in organic small molecules. Since ibuprofen is chiral, the next goal was to determine the correct enantiomer in case the sample had a crystal structure with a non-centrosymmetric space group. Organic molecules contain a substantial number of hydrogens in their crystal structure which may be hard to detect. As a result, the last task for this sample was to see if there was a possibility to directly see the hydrogen in the structure in Fourier maps.

The problem of sublimation was addressed by using the cryo-plunging sample preparation described in Chapter 2 followed by an observation in cryo conditions.

Data collection on this sample although challenging, was successful and resulted in a total angular range of 104° collected in PEDT mode. We found the unit cell parameters to be a=12.21 (3) Å b=8.006(3) Å c=13.565(19) Å and β= 111.65(12)°. These values were comparable to what was obtained with the SCXRD data that is cell a=12.1051(3) Å b=7.9464(2) Å c=13.3610(4) Å, β= 111.923(3)°. A non-centrosymmetric space group of monoclinic $P2_1$ was found. After checking the reciprocal space sections (Figure 3.7) we see the extinctions characteristic of a 2_1 screw axis along b. With a unit cell volume of 1327.761 $Å^{3,}$ the asymmetric unit could host two molecules of ibuprofen.

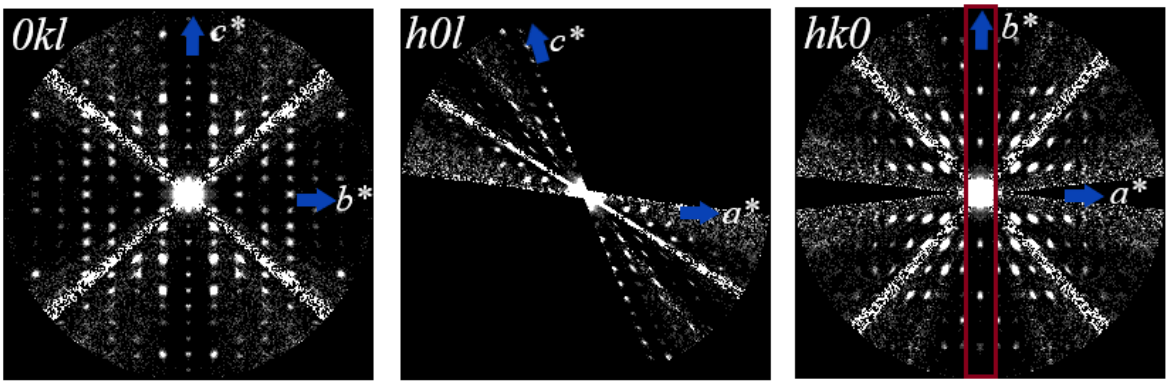

Figure 3. 7 Reciprocal space sections showing the main crystallographic directions of ibuprofen

A structural model was then obtained after structure solution using *Shelxt* completely *ab initio* without any previous knowledge of the molecule involved and all the non-hydrogen atoms were correctly located. Both kinematical and dynamical refinements were run on the structural model. The kinematical refinement resulted in an *RValue* (R_{obs}) of 17.9% and a goodness of fit of 1.14 however, signals from H atoms were not strong enough to be added and refined. With the dynamical refinement, 8 of the hydrogen out of 34 were detected in the difference maps which were then added to the structure and refined. We checked the refinement for the L and S molecules obtaining the best *RValue* (R_{obs}) of 11.3% for S-ibuprofen (Table 3.4). The other enantiomer gave an *RValue* (R_{obs}) 1.5%. Remarkably, the sample was a pure crystalline synthesis of S-ibuprofen. The model obtained with 3D ED is displayed in Figures 3.8 and 3.9. In the first picture, the asymmetric unit formed by two S-ibuprofen molecules can be seen, in the second picture the crystal packing viewed along *a* and *b* directions is displayed.

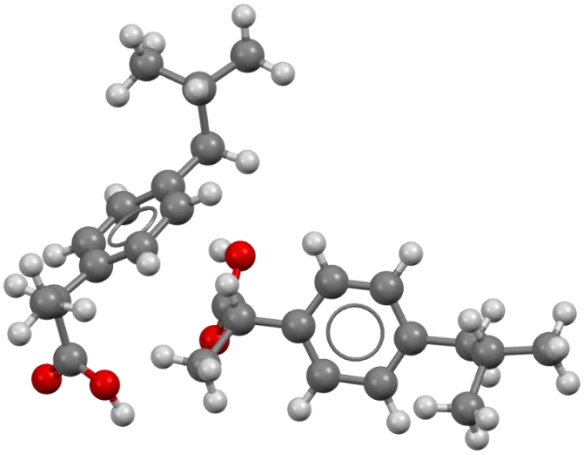

Figure 3. 8 The asymmetric unit of S-ibuprofen crystal structure containing two molecules of ibuprofen

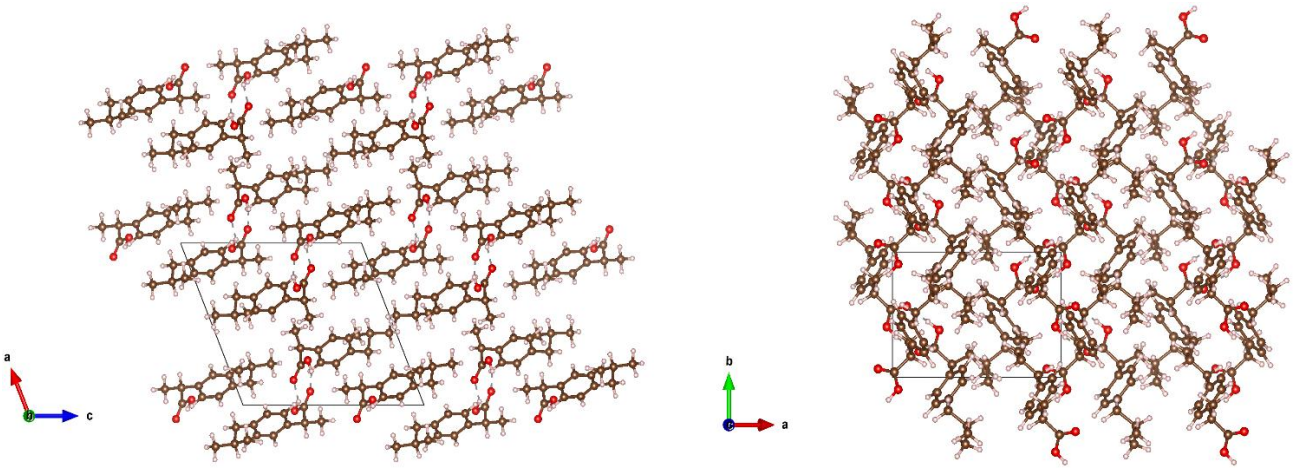

Figure 3. 9 Crystal packing of S-ibuprofen on the left viewed along b and on the right viewed along c

Crystal data	
Chemical formula	$C_{13}H_{18}O_2$
M_r	206.3
Crystal system, space group	Monoclinic, $P2_1$
Temperature (K)	93
a, *b*, *c* (Å)	12.21 (3), 7.98 (3), 13.520 (19)
β (°)	111.041 (12)
V (Å^3)	1228 (6)
Radiation type	Electron, λ = 0.0335 Å
Data collection	
Data collection instrument (TEM)	Zeiss Libra 120
Data collection type	PEDT
Precession angle(°)	1
Angular Range (°)	104
Angular step	1
Beam size (nm)	≈150
Measured, independent and observed [$I > 3\sigma(I)$] reflection	14101, 2805, 635
(sin θ/λ)max (Å−1)	0.5
Kinematical Refinement	
R(obs), wR(all), S	0.179, 0.457, 1.14
No. of reflections	1873
No. of parameters	104
Dynamical Refinement	
R(obs), wR(all), S	0.113, 0.278, 1.35
No. of reflections	4224
No. of parameters	171
Absolute structure	963 of Friedel pairs used in the refinement

Table 3. 4 Results after both kinematic and dynamical refinement of the crystal structure of S-ibuprofen

Conclusion

To have an idea of the accuracy obtained in our structures we compared them with respect to the SCXRD reference structures obtained at CNRS. To do this, we used the COMPSTRU utility of the Bilbao Crystallographic Server (De La Flor et al., 2016), which delivers the distance between the corresponding atomic positions of the two compared structures. In COMPSTRU, "the difference between the two models is quantified by evaluation of the global distortion decomposed into a spontaneous strain (lattice deformation) and atomic displacement field representing the distances between the paired atoms of the two structures." Therefore, before comparing the atomic positions of the checked structure with the reference structure, the software deforms its unit cell to make it most similar to the reference, and then it evaluates the atomic shifts. This compensation of different unit cells is particularly necessary for 3D ED data, where the accuracy in the unit cell determination is low. As key parameters for the comparison, the maximum (d_{max}) and the average shift (d_{ave}) given by COMPSTRU were considered, which are a sort of maximum distance and average distance between the corresponding atomic position in the determined model and the reference model. The comparison for the three analyzed sampled is displayed in Table 3.5

Sample	**Kinematical**		**Dynamical**	
	dmax (Å)	d ave (Å)	dmax (Å)	dave (Å)
Epidote	0.119	0.066	0.060	0.024
Natrolite	0.126	0.061	0.065	0.038
S-Ibuprofen	0.2675	0.1013	0.1161	0.0602

Table 3. 5 Comparison of the three structures obtained with COMPSTRU

As can be seen, dynamical refinement always increases the accuracy by almost a factor of two. We can also state that the errors in the located atoms are better than 0.04 Å on average and around 0.06 Å for the organics because of their beam sensitivity is more challenging. Our results are in line with those obtained in the other laboratories.

The two inorganic structures were solved by all seven laboratories *ab initio* and refined using kinematical and dynamical refinement. The *RValue* (R_{obs}) after refining the crystal structure of the epidote ranged between 17.5% - 27.4% for kinematical and 8.7%-14.3% for dynamical refinement. In the case of natrolite, the *RValue* (R_{obs}) was slightly lower, with a range of 12.4% - 21.6% kinematical and an impressive range of 5.9% - 17% for dynamical refinement. The data collection for the S-ibuprofen was done by five labs with cryo-cooling capabilities. The final models obtained were refined kinematically resulting in an *RValue* (R_{obs}) between 16% - 27%. Only 3 labs however run dynamical refinement resulting in *RValue* (R_{obs}) of 11.3%, 10.6% and 14.5% respectively. The accuracy of the structure dynamical refinement averaged over all labs was 0.012 Å for epidote 0.027 Å for natrolite and 0.042 Å for S-ibuprofen.

These numbers can be considered the actual accuracy we can expect from a 3D ED analysis. The results of this chapter show which kinds of challenges can be faced by 3D ED. It is possible to solve most inorganic and organic structures provided they are not super beam sensitive, without any prior chemical knowledge (which can eventually be derived by EDX analysis). It is possible to refine mixed occupancies, to determine hydrogen positions, both in inorganic and organic structures, it is possible to determine the absolute structure.

The consistency in the results from the different laboratories in this work also confirms how reproducible 3D ED is regardless of the type of setup used. It is also worthy to note that the unit cell parameters obtained from the 3D ED may be slightly different from those from SCXRD and PXRD and that they are typically reliable only to two decimal places due to lens distortions and other instrumental factors (the errors reported here are numerical estimate coming from the least square refinement on the data and cannot estimate the real errors which are of the order of 0.5 %).

CHAPTER 4

Oxyresveratrol polymorphic forms studied using 3D ED

Background

In this chapter, we will apply 3D ED for the crystal structure solution of different polymorphs of a natural compound. The structural characterization will be based on a combination of 3D ED with other characterisation techniques to explore the possible phases of oxyresveratrol present in a nanocrystalline phase mixture. Thanks to this synergy, we successfully determined: the crystal structure of the first unreported anhydrate phase (A-ORV) of oxyresveratrol from 3D ED data collected at room temperature and the crystal structure of a new hydrate polymorph of oxyresveratrol (H-ORV) which was identified and studied thanks to the cryoplunging sample preparation method. All these phases existed in a polyphasic mixture purchased from a chemical company which testifies how 3D ED can identify phases in challenging powder samples and can be used as a quality control technique. Thermal and calorimetric analyses were conducted to understand the thermal behaviour and dehydration pathways of the identified phases. Furthermore, density functional theory (DFT) calculations were used to investigate the rotational conformations of the molecule and the stability of the conformers. The combination of 3D ED and other solid-state analyses method for studying nanocrystalline natural compounds was established as a powerful tool to be applied in the pharmaceutical industry.

4.1. Introduction

Natural products come in different classifications such as alkaloids, terpenoids, flavonoids, stilbenes etc. (Springob & Kutchan, 2009). Stilbenes are a family of polyphenolic compounds with a basic structure containing two phenyl rings. They have been shown to have antifungal, antioxidant and anti-inflammatory properties (Springob & Kutchan, 2009) (Teka et al., 2022) (Suzuki et al., 2019). One of such stilbenes is oxyresveratrol which like other stilbenes have some anti-inflammatory properties, antimicrobial activities (Likhitwitayawuid, 2021) and even

recently a potential anti-cancer effect (Thaklaewphan et al., 2024). Oxyresveratrol (ORV) is a natural product that can be extracted from different plants including mulberry *Morus alba L.* (Figure 4.1) and in significant amounts from heartwood of *Artocarpus lacucha.* The different parts of the mulberry plant have been used in traditional Chinese medicine for treating various health problems (H. Wang et al., 2024) (Chatsumpun et al., 2016). Chemically, ORV is trans-3,5,2′,4′-tetrahydroxystilbene and in Figure 4. 1 we can see its chemical structure.

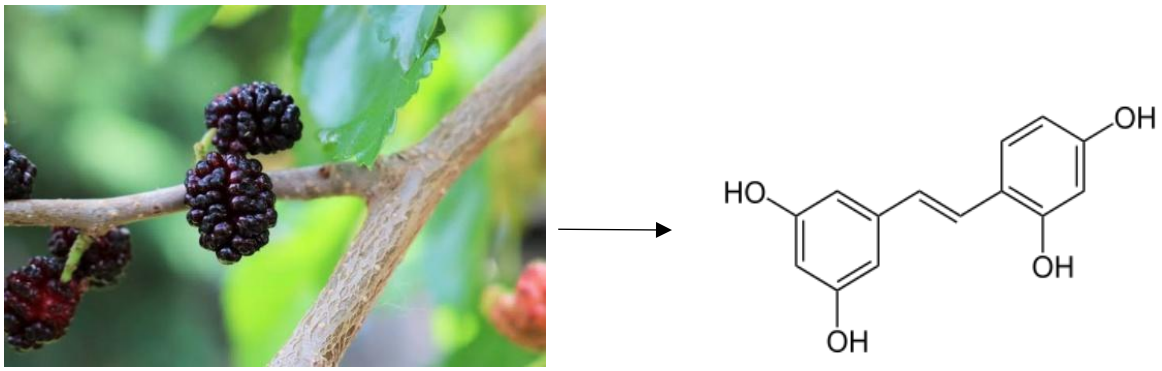

Figure 4. 1 On the right is the mulberry plant from which oxyresveratrol can be extracted, and on the right is the chemical structure of oxyresveratrol

Its chemical structure contains two aromatic rings held together by an olefinic bond and on each aromatic ring there are two hydroxyl groups. Oxyresveratrol has a similar chemical structure as resveratrol, another naturally occurring stilbene. However, in resveratrol one of the two aromatic rings has only one hydroxyl group. Resveratrol also shows similar pharmacological activities and can be extracted from the same plants as oxyresveratrol (Zeng et al., 2021). Due to the presence of an extra hydroxyl group, oxyresveratrol is slightly more effective than resveratrol in its application as an inhibitor and a biological binder (Zeng et al., 2021). However, the crystal chemistry of oxyresveratrol has not been widely studied probably because it tends to exist in powder form and large single crystals are difficult to grow. So far, the only crystal structure of oxyresveratrol reported is in the hydrated form, by Deng et al. in 2012 with the CCDC code ZAPDOL (Figure 4.2).

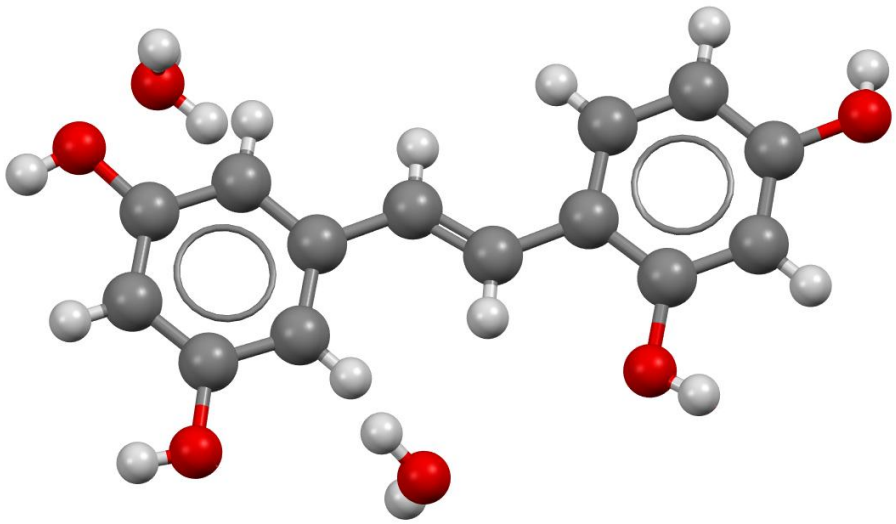

Figure 4. 2 Crystal structure of ZAPDOL with the asymmetric unit containing two molecules of water

The structure was solved using SCXRD by first obtaining resveratrol from mulberry and then further converting it to oxyresveratrol. It crystallized in a triclinic space group, *P*-1, with a volume of 654.509 $Å^3$ and unit cell parameters *a*=6.6523 (5) Å *b*=9.2005 (9) Å *c*=11.5294 (8) Å with angles α=72.533 (7)º β=78.686 (6)º and γ= 79.651 (7)º. There are two molecules of water in the asymmetric unit in disordered positions. Hydrogen bonding was observed between both the hydroxyl groups and the water molecules. Although other multicomponent crystalline forms of oxyresveratrol like cocrystals have been reported (Suzuki et al., 2019), no other polymorph has been reported, and any anhydrous form was unknown. In this chapter, we explore oxyresveratrol polymorphism by combining 3D ED, PXRD, TGA, DSC and DFT techniques. Remarkably, this study started as side research of the main project of this thesis, which was the structure determination of oxyresveratrol cocrystals. However, the characterization of the purchased starting oxyresveratrol reagent showed already a powder pattern that did not match the known crystal structure, and this triggered all the following research on the crystal structure of this molecule.

4.2. Molecular Modelling

The ORV molecular conformations were investigated using molecular modelling studies, DFT theory level with a B3LYP functional and a 6-311+(3d, p) basis set. It was performed using the energy scan calculation by fixing the dihedral angle and gradually increasing it by 2° while optimizing the geometry on each step using the *Gaussian 16* software (Frisch et al., 2016). Two stable conformations of the ORV molecule were found, attributed to the rotation of one of the aryl groups up to 180º about the single C-C bond with respect to the other aryl ring. The two conformations are labelled 1 and 2 in Figure 4. 3 below. The DFT calculations showed a total activation energy (E_a) for the rotation of the aryl group to be 22.72 kJ mol^{-1}. It also revealed that the interconversion energy from conformation 1 to 2 as ΔE=1.94 kJ mol^{-1} is seen in Graph 4.1 and shows that the ORV conformation 1 is twice as likely to form as conformation 2.

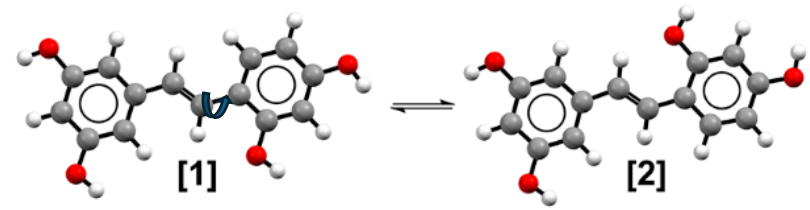

Figure 4. 3 Molecular modelling studies of the conformations of oxyresveratrol

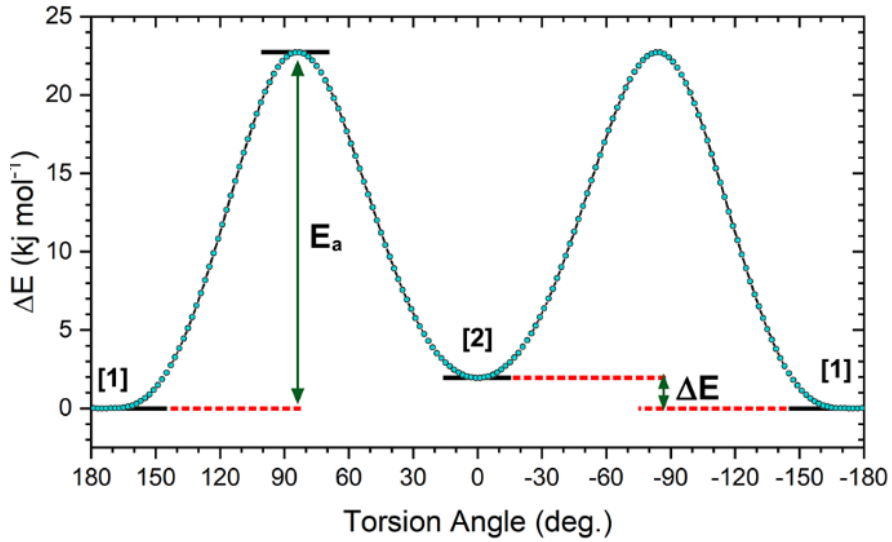

Graph 4. 1 Stabilization energies of the two conformations against their torsion angles of oxyresveratrol

4.3. Anhydrate Oxyresveratrol Crystal Structure

An oxyresveratrol sample was purchased from Sigma Aldrich and used as received for PXRD analysis to check the phase present. All the PXRD data were collected using the STOE Stadi P diffractometer with a Cu -Kα1 radiation source of wavelength λ=1.5406 and a Debye-Scherrer geometry. All samples in this work were prepared by loading them into a borosilicate glass capillary with a diameter of 0.5mm. The data were acquired in the 2θ range of 3−90° which corresponds to a maximum resolution of 1.09 Å with an interval of 0.03° between the consecutive points. The only exception is the data collection on the as-received ORV sample; since the purpose was only the phase quantification, it was characterized in the 3−70° angular range which corresponds to a maximum resolution of 1.34 Å. Data were preliminarily processed using *WinXPOW* software (by STOE & Cie). In Figure 4.4, we see the PXRD pattern of our starting material (black) and the simulated PXRD pattern of ZAPDOL (red). It was clear that the two patterns did not fully match giving a strong indication that the sample was hosting of a different phase.

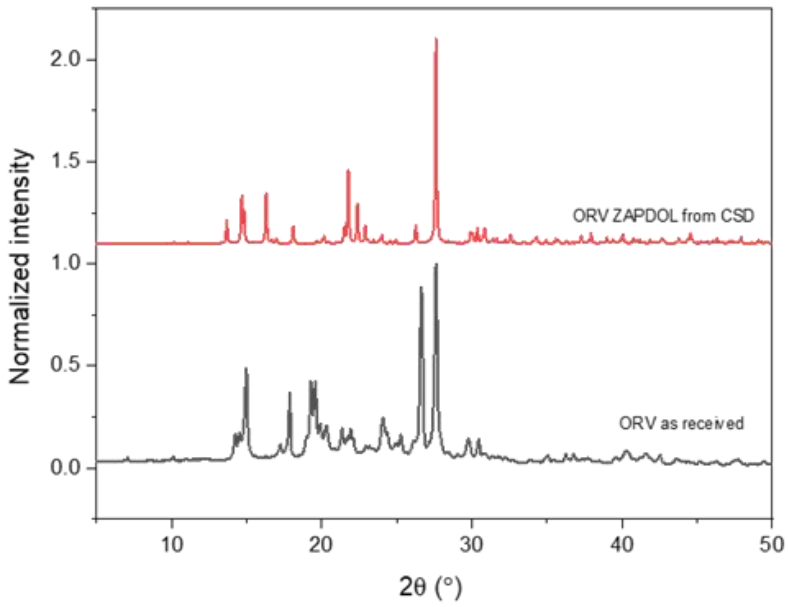

Figure 4. 4 Experimental PXRD pattern of ORV sample as received in black compared to the simulated PXRD pattern of ORV ZAPDOL from the database in red

3D ED data collection was then acquired on the as-received ORV sample after an unsuccessful initial attempt to synthesize large crystals for SCXRD. 3D ED data were collected on the samples at room temperature with cRED. cRED data collection was done with a parallel beam size of approximately 570 nm using a fast acquisition enabled by the *LibraEDT* software *(Faye et. al, 2025 manuscript under preparation*). Room temperature sample preparation for 3D ED was performed with the protocol listed in the previous Chapter 2. More than 10 data sets were collected, with the crystals being relatively stable under the electron beam during the acquisition. The crystals had morphology appearing like layered thin platelets (Figure 4.5). All the indexed data sets pointed to a monoclinic unit cell with parameters a=5.05 (1) Å b= 12.7 (1) Å, c=18.1(1) Å, β= 91.4 (1)º and volume V=1115.3(2) Å^3. These were different unit cell parameters compared to those of ZAPDOL. After analysing the reciprocal space sections, a monoclinic space group of *Pc* was chosen due to the presence of a glide plane given by the reflection condition $h0l$:l=2n (Figure 4.6).

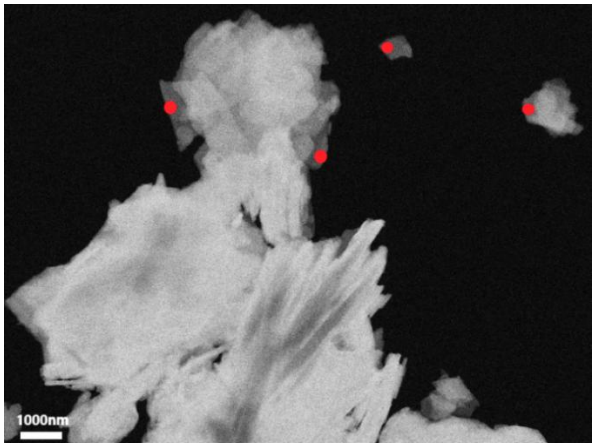

Figure 4. 5 HAADF-STEM image of typical A-ORV crystals comprising of layers of platelets with the red dot indicating possible points for data acquisition

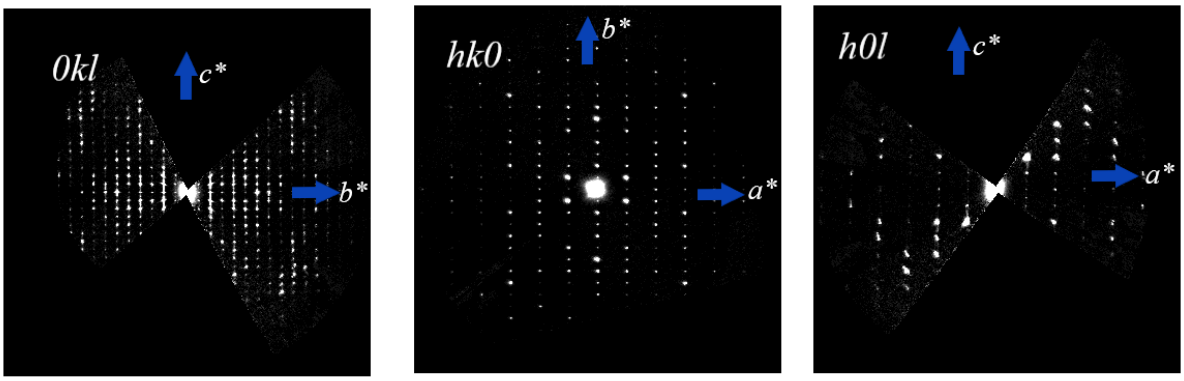

Figure 4. 6 Reciprocal space sections of ORV data of as-received sample.

The structure was then solved *ab initio* in the monoclinic space group *Pc* (7) using *Shelxt* and all 36 non-hydrogen atoms in the asymmetric unit were detected. The structure that was solved appeared to be a new anhydrate ORV (A-ORV) polymorph, with two ORV molecules in the asymmetric unit. The ORV molecules in the asymmetric unit assumed conformation 1 which was the same conformation as the ORV molecule in the ZAPDOL crystal structure.

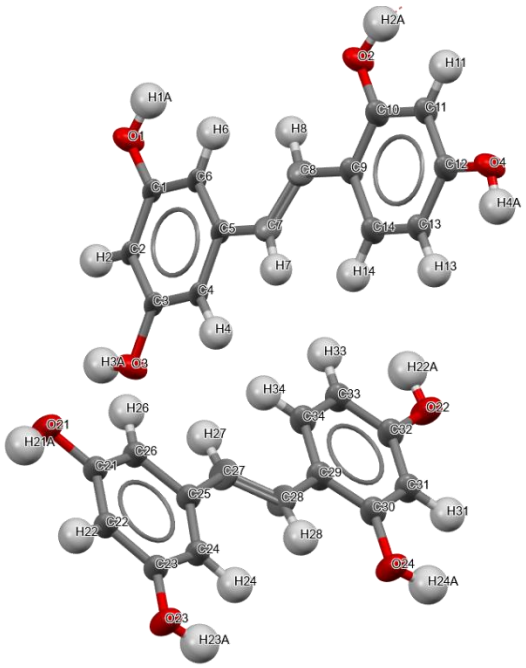

Figure 4. 7 The asymmetric unit of the A-ORV in ellipsoid of 50% probability containing two molecules of ORV assuming the conformation 1

The first run of dynamical refinement was performed without the hydrogen atoms against $|F|^2$. The interatomic bond distance angles, the flatness of the two different aryl rings and the geometry of the aromatic rings were restrained. The thermal parameters of all the atoms were refined anisotropically. The hydrogen atoms were then added automatically and constrained to a riding model for the second run of refinement. The dynamical refinement resulted in an R_{obs} of 12.45% with the resulting parameters listed in Table 4. 1. The final model can be seen in Figure 4.7, which is drawn with the anisotropic thermal ellipsoids for the non-hydrogen atoms and 50% probability for the H atoms. The arrangement of the molecules in the crystal structure along different directions is seen in Figure 4.8. A-ORV molecules in the crystal structure have an arrangement that appears as layers of chains stacked along the *b*-axis Figure 4.8 (b). Each chain layer is formed by one of the two independent molecules of the asymmetric unit. Along the [401] or [-401] direction (Figure 4.8 (c)), the chains run parallel to each other depending on which molecule belongs to the layer. However, when viewed along *a* in Figure 4. 8 (a), the layers have an alternate stacking attributed to the staggered configuration of the molecules. The molecules are disposed in a head-to-tail fashion along the chains and are held in place by H bonds involving the OH groups that are present in the para and para′ position of the aromatic ring and the OH situated in the meta position of the other ring. Only one H bond is between two consecutive molecules of the same chain (O3−H3A···O4), while all the others connect adjacent layers laterally and the chains in the same layers interact with each other through π−π interactions.

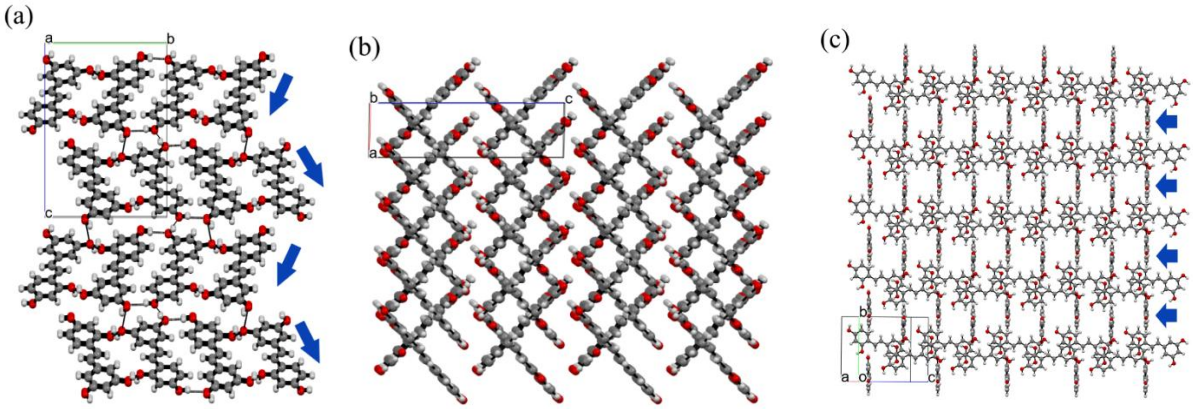

Figure 4. 8 The molecular arrangement of oxyresveratrol in different crystallographic directions in (a), a direction in (b) the b direction and in (c) the [401] direction

To study the thermal behaviours of the as-received sample, DSC and TGA thermal analysis were performed. The DSC analysis was done using the calorimeter PerkinElmer model 8500 which is equipped with the Intracooler III as the refrigerating system. The samples were loaded into a 40µL aluminium pan and sealed with masses ranging from 5 mg to 10 mg. The temperature and enthalpy scale calibrations were done with indium. Nitrogen was used as the purge gas with a flow rate of 20mL/min. The TGA measurements were performed with a PerkinElmer instrument, model TGA 8000 only on the starting sample. All calorimetric measurements were carried out at a rate of 10K/min. In Graph 4.2, we see the results of the thermal analysis of the starting ORV sample. It can be seen on the TGA plot that there was a mass loss of about 5% between the temperatures of 298K−393K. A corresponding endothermic peak was observed between 350-383K in the DSC scan which reached a maxima at 367K. This can be associated with the loss of bound water in the sample. This was the first indication of the presence of a hydrated phase in the sample. Between temperature ranges of 457 and 487 K, it was observed that one endothermic peak merged with an exothermic peak. This phenomenon is associated with the melting and the onset of the decomposition of the compound.

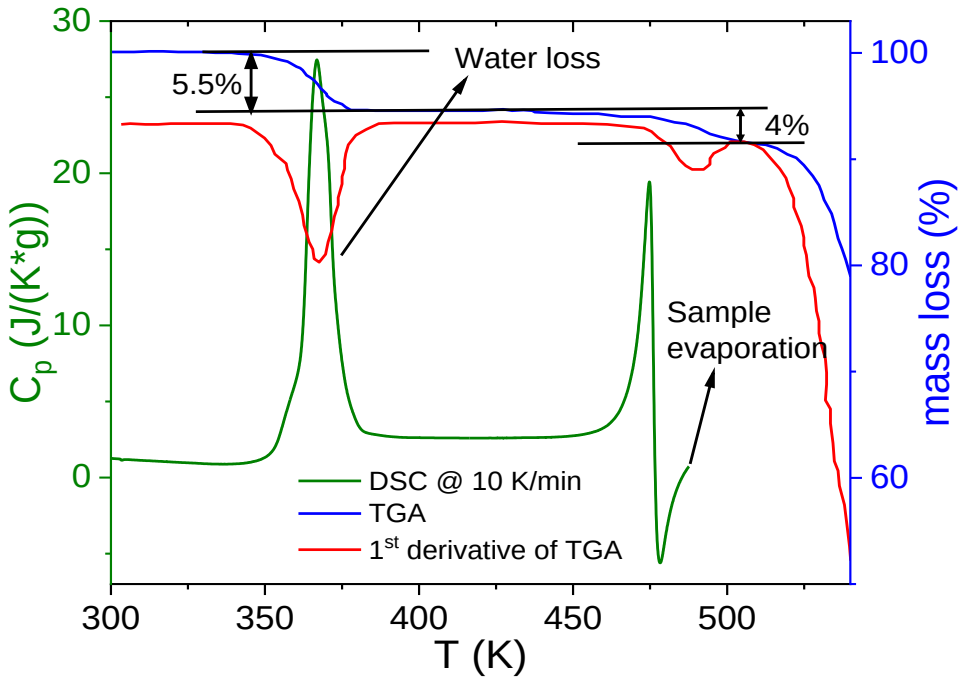

Graph 4. 2 DSC in green and TGA in blue analysis and the 1st derivative of the TGA in red of ORV received sample

Since there was a clear indication of water in the starting sample, a Variable Temperature PXRD (VT-PXRD) analysis was done to get a deeper understanding of how the structure is modified by the loss of water (Graph 4.3). The sample was loaded into a 0.5 mm quartz capillary and then mounted in a STOE capillary furnace. The detector was kept fixed at 20° while recording since the peaks of interest were in the 2θ range of 12−32°. After every 10°C, an isotherm of 3 min was done, after which data collection was performed. This in-situ analysis was carried out from room temperature up to 390 K at a heat rate of 10k/min. This corresponded to the range of temperatures where water is lost according to the TGA profile (Graph 4.2). According to our observation, the crystalline state of the ORV as received sample was stable until 370 K. Once the temperature range went further up to 370−390 K, some of the peaks lost their intensities, but some remained unchanged. The peaks which remained unchanged were noted to belong to the pure A-ORV phase which could be obtained, as pure phase as the final product at a temperature of 403 K. It was also confirmed by comparing the experimental PXRD pattern obtained to the simulated PXRD pattern from the A-ORV 3D ED crystal structure.

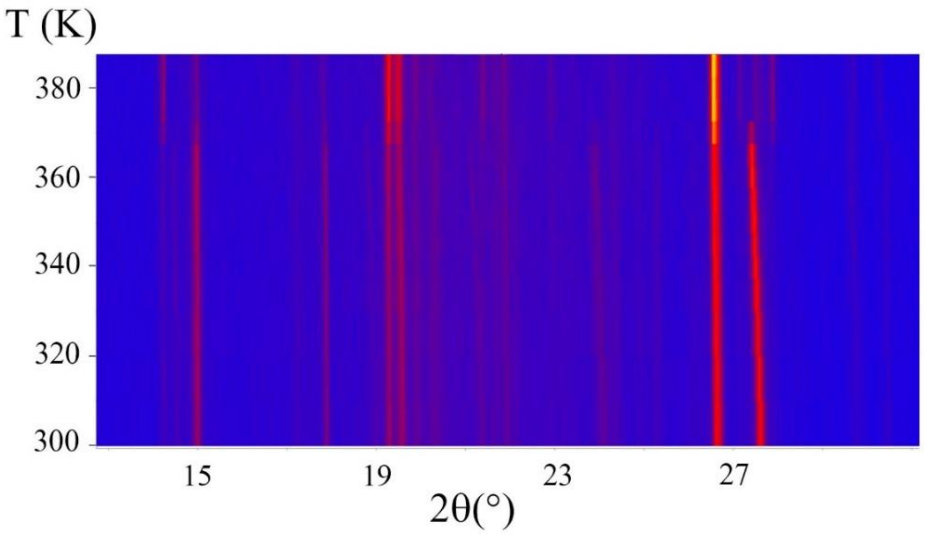

Graph 4. 3 VT-PXRD pattern of ORV obtained from heating the sample from room temperature up to 403 K

Based on this information, we were able to synthesize the pure A-ORV phase in any desired quantity after heating the as-received ORV sample at 403 K with reduced pressure overnight. A thermal study was then done on the pure A-ORV sample to affirm its behaviour further. In the DSC scan of the pure A-ORV in Graph 4.4a, we see a small bump at around 355 K during the 1st scan (in blue). This can be associated with the loss of some residual loose water which is present in a smaller quantity in comparison to what was seen in the same region in the scan of the as-received ORV in Graph 4.2. Interestingly, no other peak is detected before the sample melts which testifies to the fact that the phase is anhydrous.

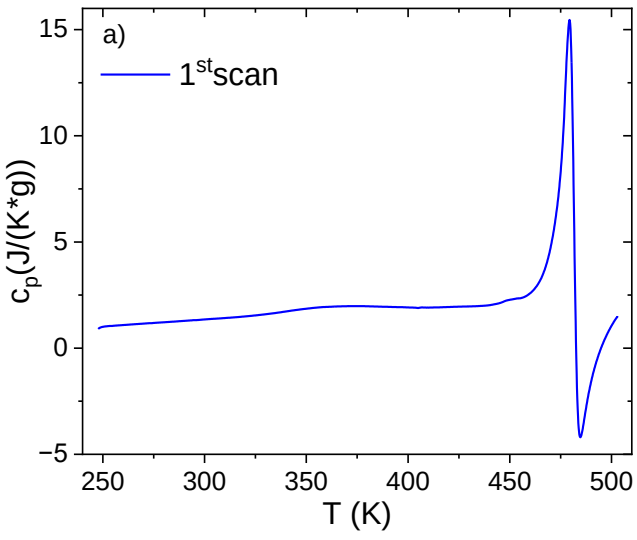

Graph 4. 4 DSC scans of A-ORV at a heating rate of 10 K/min with a) consecutive heating scans of A-ORV and b) consecutive heating scans where the first heating (blue line) was interrupted during melting. The second(red) and third(green) heating scans are restricted to the glass transition region

The experimental PXRD data of the pure A-ORV could be indexed with the 3D ED A-ORV primitive monoclinic cell parameters. Le Bail fit was performed to get the precise unit cell parameters' estimation, which refined the cell parameters to a = 4.9417(6) Å, b = 12.4553(15) Å, c = 18.1194(18) Å, β =89.9094(18)° and V = 1115.3(2) Å^3. The refinement converged to final R_p = 3.54 % and wR_p = 6.02 % with the calculated and observed profiles seen in Figure 4.9

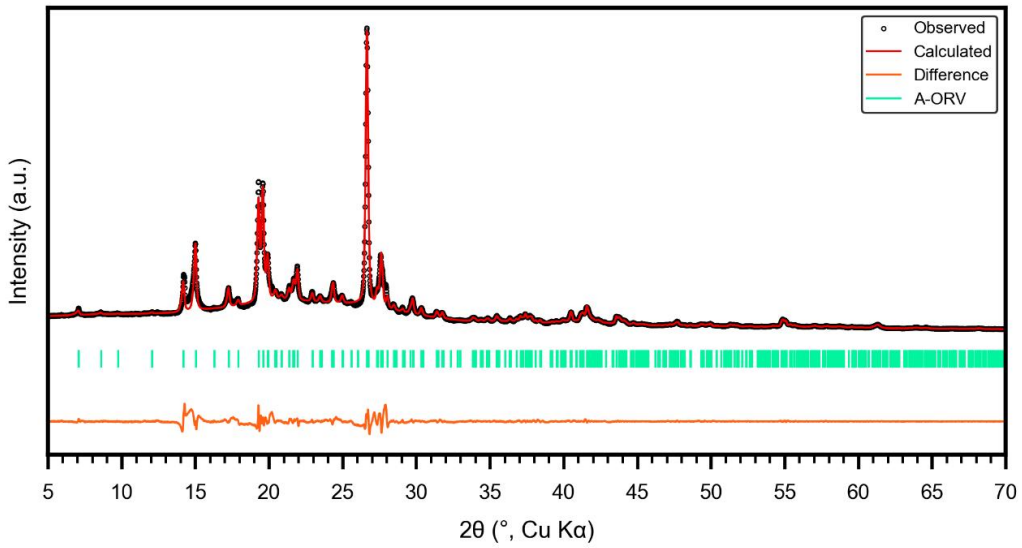

Figure 4. 9 Profile fit from Le Bail refinement on PXRD data of A-ORV. The ranges shown are limited to 2θ values of 5-70° for clarity, whereas the refinement was carried out in the range 3-90°.

After the Le Bail refinement, Rietveld refinement against PXRD data was conducted using the A-ORV crystal structure from 3D ED as the starting model to allow for the refinement of the atomic positions. Both refinements were carried out in *JANA2020*. The ORV molecules were refined as semirigid bodies and the torsion angles related to single bonds were freely refined. The structural model from the Rietveld refinement resulted in the same conformation as the initial 3D ED model, highlighting the accuracy of the 3D ED technique. The refinement

converged to a final *Rp* = 8.20 %, *wRp* = 12.45 % and the profiles of the observed and the calculated are seen in Figure 4.10.

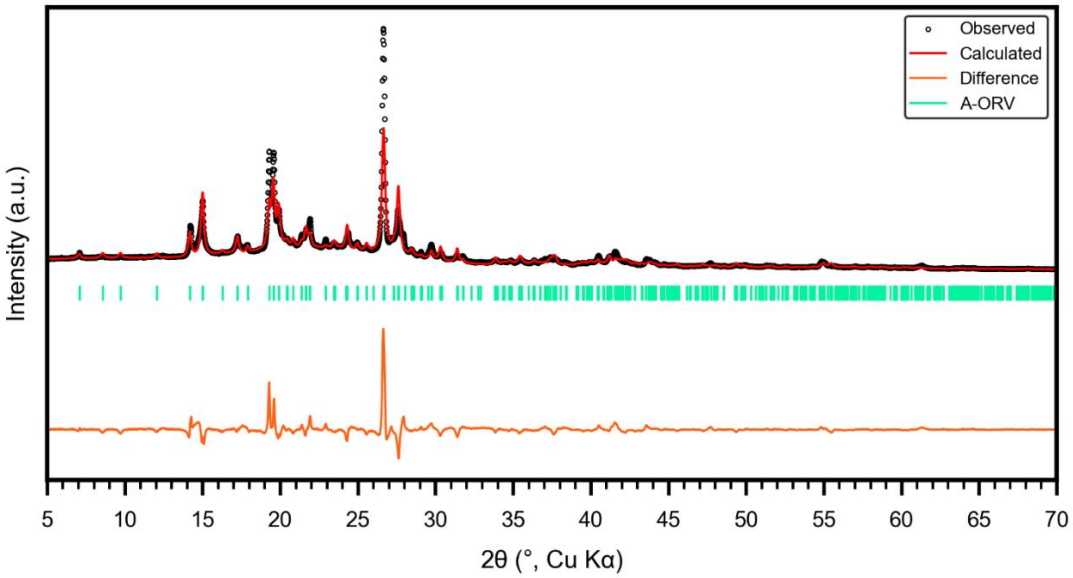

Figure 4. 10 Profile fit from Rietveld refinement on PXRD data of A-ORV. The ranges shown are limited to 2θ values of 5-70° for clarity, whereas the refinement was carried out in the range 3-90°.

4.4. Hydrate Oxyresveratrol Crystal Structure

Based on the thermal studies conducted on the as-received ORV sample, we could confirm that there was a hydrated phase present together with A-ORV in the as-received sample. Therefore, we synthesized the pure hydrated form by dissolving the precursor in a methanol and chloroform mixture in a 1:4 ratio. The resulting liquid had a yellowish hue which was evaporated slowly under a chemical hood. To ensure the full evaporation of the solvents, the sample was left in a vacuum oven at 40ºC. PXRD data were collected on the resulting powder, which showed a different pattern that did not match with the simulated PXRD pattern of *ZAPDOL,* pointing to a possible new ORV hydrate polymorph.

During the first set of 3D ED data collection on the as-received ORV sample, no crystalline hydrated phase was observed inside the TEM. However, we did detect several amorphous grains now and then on the grid. The synthesized pure H-ORV phase was also amorphized

when 3D ED room temperature data collection was attempted. This could be due to the high vacuum in the TEM causing dehydration and structural collapse of the hydrated phase. For protection by the amorphous ice, the cryoplunging sample preparation listed in Chapter 2 was used to successfully preserve the hydrated phase. PEDT data collection with a parallel beam size of approximately 150 nm was used in a stepwise acquisition with a 1° precession angle on a cryoplunged sample at -180 °C with a cryo-transfer sample holder. The crystal search was done in STEM mode after 3D ED data was acquired on three crystals appearing as thin large platelets as seen in Figure 4.11.

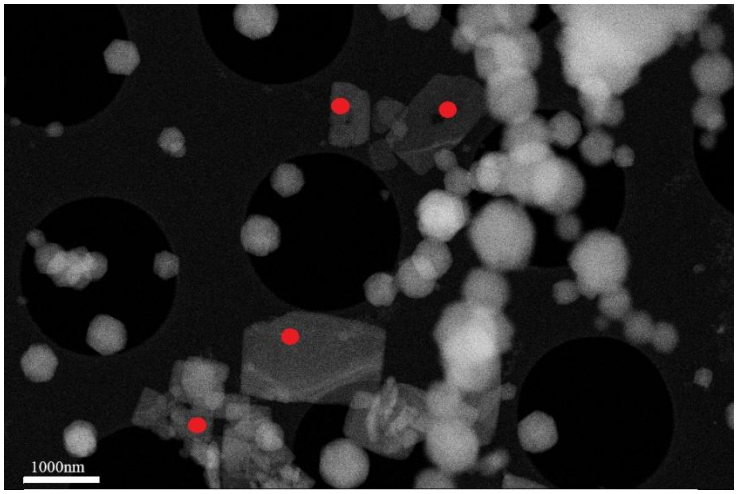

Figure 4. 11 HAADF-STEM image of typical H-ORV crystals for the 3D ED data collection

All three data sets had similar unit cell parameters with a= 8.87(1) Å b= 8.11(1) Å c= 9.29(1) Å with a volume V=668.28(1) Å^3 and a beta angle of 90.9(1)°. Although the volume was like *ZAPDOL,* a higher symmetry space group was observed (Figure 4.12). The presence of extinction condition $h0l$=2n suggests the presence of a c glide plane pointing towards a possible monoclinic space group *Pc* (also *P*2/*c* would be possible but due to the molecule shape we first try the non-centrosymmetric one). Interestingly, this phase has the space group, *Pc*, as the A-ORV but with half of its cell volume.

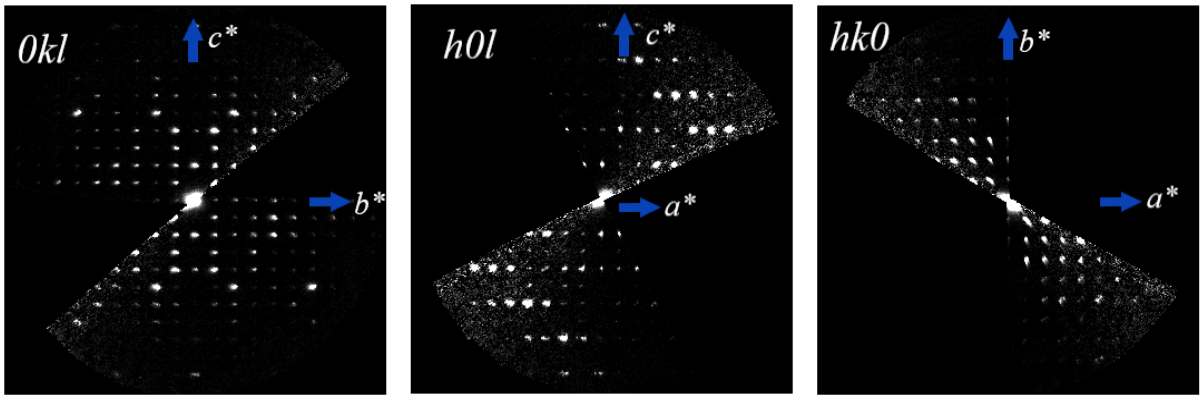

Figure 4. 12 Reciprocal space sections of the H-ORV 3D ED data

The crystal structure of a new hydrate ORV polymorph, H-ORV was then solved *ab initio* in the monoclinic *Pc*. The model was then refined kinematically with isotropic thermal factors resulting in R_{obs} of 24.5%. Unfortunately, the data quality was not high enough for dynamical refinement to accurately determine the hydrogen positions of the water molecules. In the resulting crystal structure, H-ORV had an asymmetric unit containing two molecules of water and one molecule of ORV (Figure 4. 13a). The hydrogen bonding network in the structure could only be guessed based on the interatomic distances between the O atoms of the water molecules with the O atoms from the hydroxyl group of ORV molecules (Figure 4. 13b) found to be between 2.7 Å to 2.9 Å.

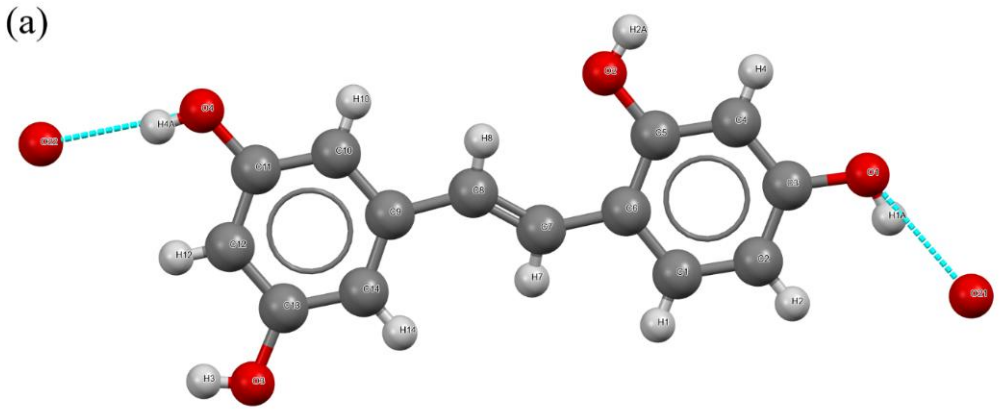

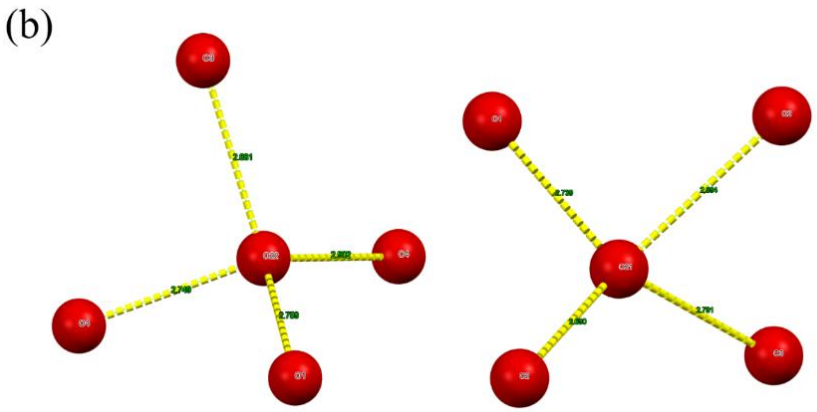

Figure 4. 13 (a) Asymmetric unit of H-ORV with the two water molecules displayed without hydrogens. (b) The hydrogen bonding network of the water molecules in the H-ORV structure

The ORV molecules in the H-ORV crystal structure form what appear to be chains on planes parallel to [10−1] in Figure 4.14 (left). The bonding between the molecules along the chain and within the chains is held together by a network of hydrogen bonds from the water molecules. The network has a distorted tetrahedral geometry which is formed by each water interacting with four other oxygens of ORV molecules.

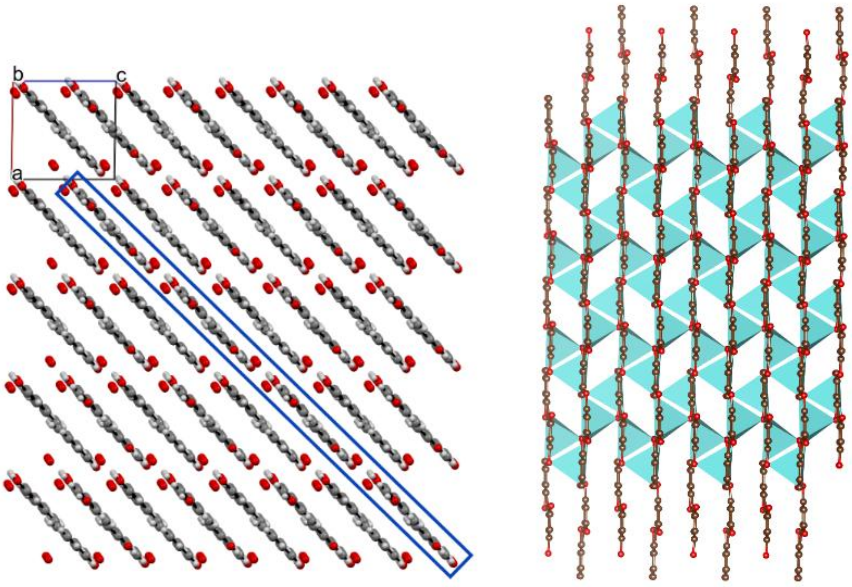

Figure 4. 13 Crystal structure of H-ORV viewed along b without hydrogens (left). Tetrahedral coordination of the water molecules in H-ORV crystal structure (right).

In adjacent planes, the chains run along two different directions, [111] and [1−11] forming an angle close to 65° (Figure 4.14). It is important to compare the structure of the new H-ORV

polymorph with that of the ZAPDOL crystal structure. H-ORV and ZAPDOL both contain two molecules of water in their asymmetric unit, however, the ZAPDOL crystallized in the triclinic centrosymmetric space group *P*-1 while the H-ORV had a higher symmetry space group, *Pc* but it is not centrosymmetric. A comparison of the packing of H-ORV with ZAPDOL can be seen in Figure 4.15. The ORV molecules in H-ORV are arranged in a head-to-tail fashion inside each plane like those in the A-ORV crystal structure. Although in ZAPDOL the ORV molecules are also packed similarly, due to the presence of the centre of symmetry, the adjacent chains of molecules run in opposite directions, while in the H-ORV they run in the same direction. Another interesting difference between the two structures is that in H-ORV, the hydrogen bonding is only between the water molecules and the O atoms of the four OH groups. In contrast, in the ZAPDOL structure, there is also a direct hydrogen bonding between the two water molecules.

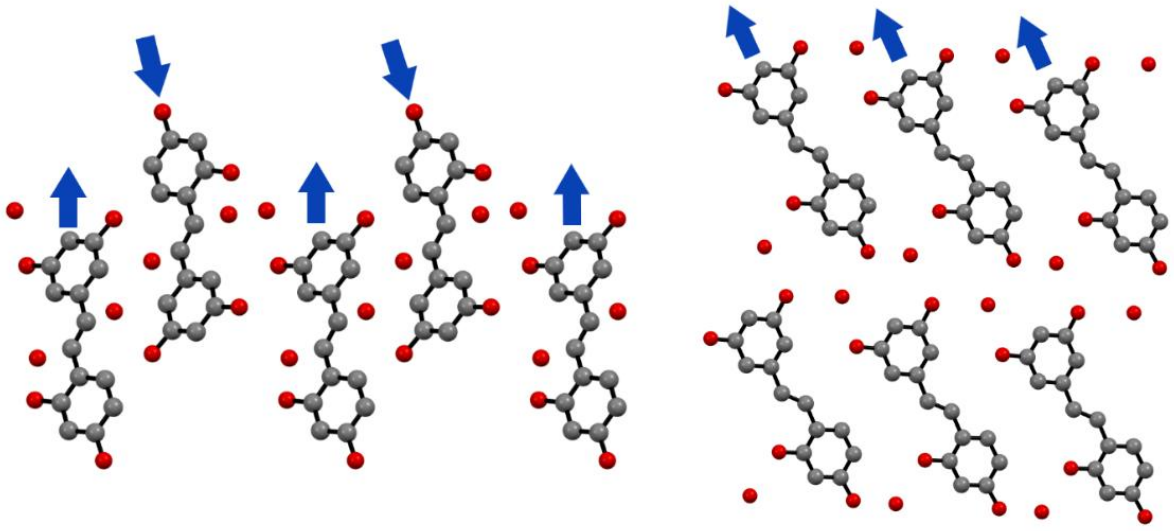

Figure 4. 14 Crystal packing of one layer chain of ZAPDOL (left) compared to H-ORV (right).

Finally, the conformation of the ORV molecule in the H-ORV structure showed conformation 2 that is one of the two aryl rings is rotated 180° around the C−C bond compared to the ZAPDOL, which has conformation 1 like that in the A-ORV structure (Figure 4.16).

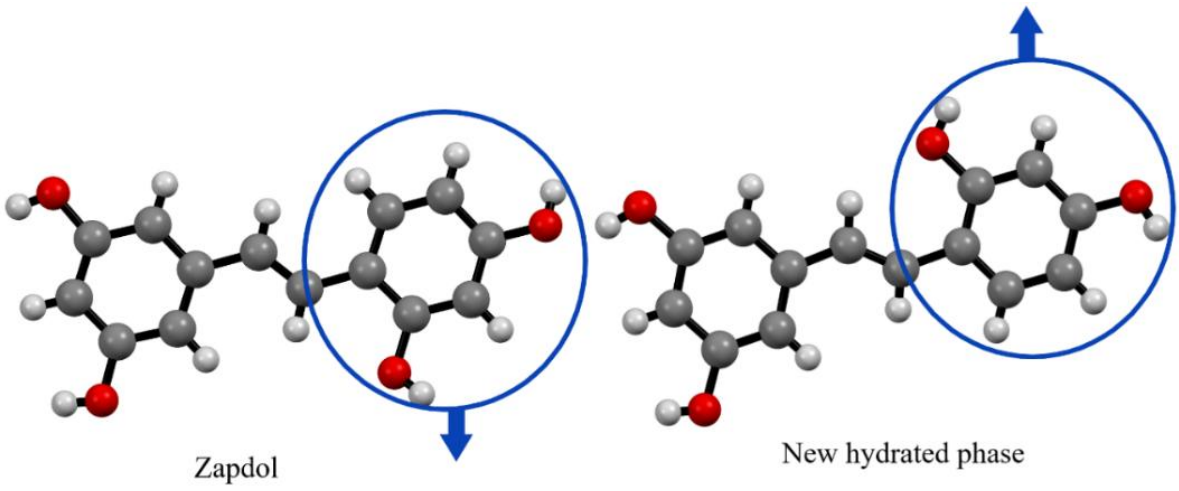

Figure 4. 15 The ORV molecule in ZAPDOL (left) had a conformation 1 compared to H-ORV with conformation 2.

A thermal investigation was then conducted on the pure H-ORV phase that was synthesized. In the first DSC scan (Graph 4.5 in red), a broad and intense peak can be seen in the temperature range of 350−425 K which can be attributed to the loss of water from the crystal structure. The sample was quenched after full dehydration at a temperature of 425 K. This intense peak was also seen in the DSC scan of the as-received ORV sample in the same temperature range. In the second DSC scan (Graph 4.5 in blue), a peak can be seen at a temperature of 486 K which is associated with the melting of the sample followed by an exothermic peak. A similar thermal behaviour is exhibited by A-ORV which shows that after water loss the sample remains crystalline due to the absence of a glass transition, unless melting is reached and then the sample is reheated.

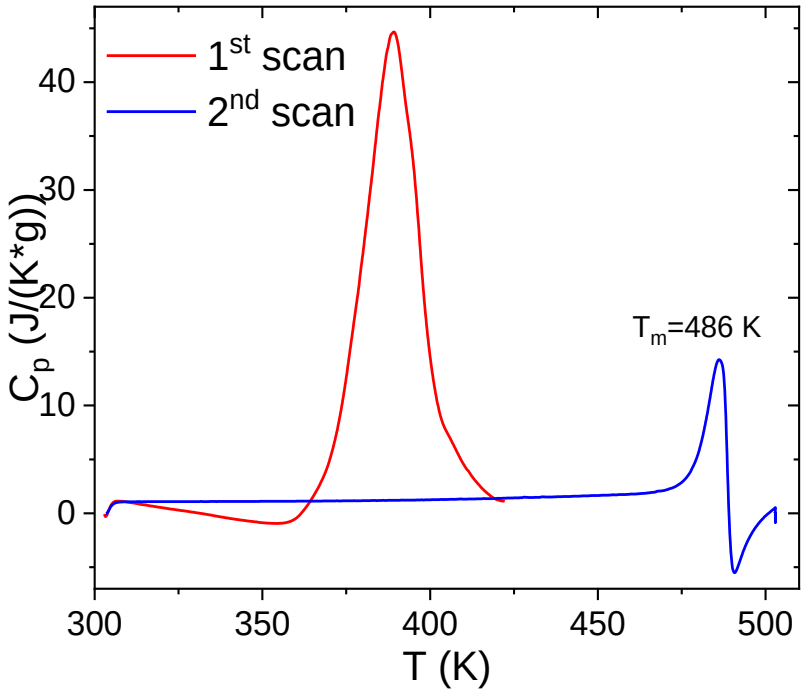

Graph 4. 5 DSC scans of H-ORV. First, the sample was brought to 425 K for its full dehydration and quenched (red line). The second scan brought the sample beyond the melting point (blue line).

Since we were able to understand the thermal behaviour of H-ORV, we wanted to confirm whether the crystal structure obtained from 3D ED was the phase obtained from the experiment PXRD data of the pure hydrated phase. First, the unit cell was confirmed when we successfully indexed and performed a Le Bail fitting of the PXRD profile. This led to a refined lattice parameters of a = 8.7224(3) Å, b = 8.0157(4) Å, c = 9.3326(3) Å, β = 91.3848(17)°, and V = 652.31(5) Å^3. The 3D ED structural model of H-ORV was then refined against the PXRD data using the Rietveld approach. In the refinement, the ORV molecule was considered a semirigid body, in which the aryl group was left free to rotate around the single C-C bond. Then, the positions of the oxygen atoms of the water were left free to refine without any restraint. This refinement converged to R_p = 8.02% and wR_p = 11.68%. The resulting structural model was in agreement with the 3D ED model (Figure 4.12a) and the profile fit can be seen in Figure 4.16.

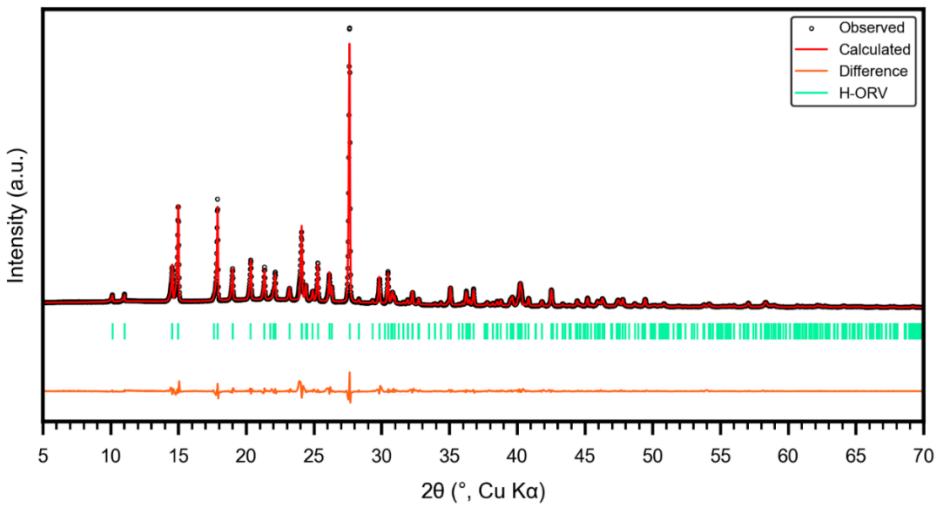

Figure 4. 16 Profile fit from Le Bail refinement on PXRD data of H-ORV. The shown range is limited to 2θ values of 5-70° for clarity, whereas the refinement was carried out in the range 3-90°.

4.5. Quantification of the Phases in the ORV as Received Sample

To confirm that the as-received sample was a phase mixture, we compared the simulated PXRD patterns of new phases (A-ORV and H-ORV) with the experimental PXRD pattern of the as-received sample as shown in Figure 4.18. It was confirmed that just a single phase could not fully account for all the peaks in the PXRD pattern of the as-received sample.

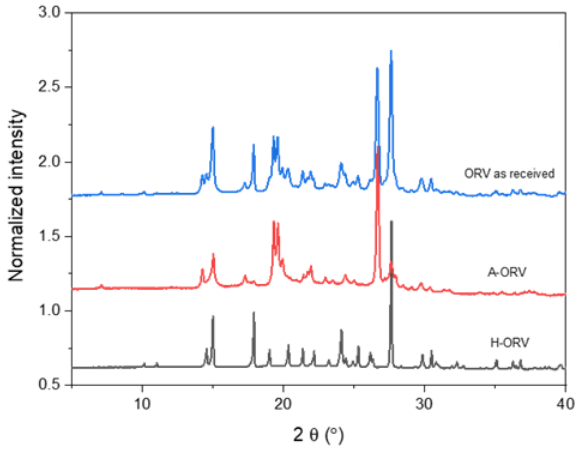

Figure 4. 17 Comparison of PXRD patterns of the A-ORV (red), H-ORV (black) and the as received ORV (blue) which supports the conclusion that there was a phase mixture in the starting sample

We then performed a Rietveld refinement using the 3D ED model of H-ORV and A-ORV. After the Rietveld refinement, we concluded that the phase mixture was composed of 58.9% A-ORV phase and 41.1% H-ORV phase (Figure 4.19). The refinement converged to R_p = 7.50% and

wR_p = 10.92%. Since the composition of the phase mixture consists of H-ORV, which is dihydrated, we can also estimate that the maximum weight loss in the case of full dehydration of H-ORV is 5.6%, which is in good agreement with the 5.5% weight loss seen in TGA data of the as-received sample.

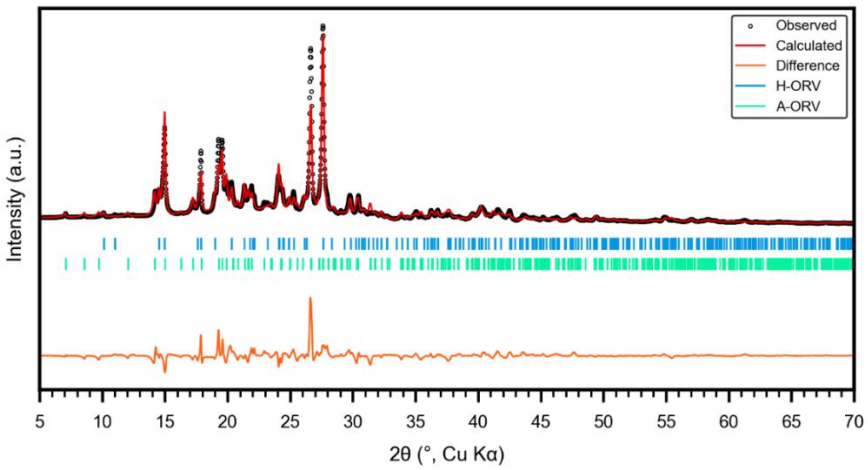

Figure 4. 18 Profile fit from Rietveld refinement on PXRD data of H-ORV and A-ORV mixed phase product. revealing a volumetric phase fraction H-ORV/A-ORV of 41.4:59.9.

Experimental details (Crystal Data)	**Anhydrate ORV**	**Dihydrate ORV**
Chemical formula	$C_{14}H_{12}O_4$	$C_{14}H_{12}O_4 \bullet 2H_2O$
Crystal system, space group	Monoclinic, *Pc*	Monoclinic, *Pc*
Temperature (K)	293	103
a, b, c (Å)	5.056 (4), 12.712 (11), 18.103 (12)	8.872 (6), 8.112 (6), 9.292 (8)
β (°)	91.37 (2)	90.929 (4)
Volume (Å^3)	1163.2 (16)	668.6 (9)
Radiation type	Electron, λ= 0.0335 Å	Electron, λ = 0.0335 Å
3D ED data collection	cRED	PEDT
Tilt range (°)	120	90
Data resolution (Å)	1.4	1.25
	Dynamical Refinement	**Kinematical Refinement**
No. of: measured, independent and observed reflections	27061, 4636, 2265	2649, 1931, 1293
Parameters	86	66
$(\sin\theta/\lambda)_{max}$ (Å^{-1})	0.620	0.619
Thickness (nm)	253.43	-
R_{obs}, wR_{obs} (%), *S*	12.45, 23.51, 2.86	24.5, 52.5, 1.72
R_{all}, wR_{all} (%)	16.70, 24.65	27.1
Δρmax, Δρmin (e Å^{-3})	0.19, -0.16	0.38, -0.23

Table 4. 2 Unit cell parameters, data collection information and the refinement statistics after dynamical refinement for A-ORV and kinematical refinement for H-ORV

Conclusion

In this chapter, we have shown how 3D ED can be instrumental in studying the crystal chemistry of natural compounds. Oxyresveratrol is an example of such a natural compound that has not been fully characterized due to its nanocrystalline nature. In the case of oxyresveratrol, the sample that was investigated was purchased from a chemical dealer but still exhibited new crystal forms that had never been reported before. Thanks to 3D ED, two new phases were detected, and their crystal structures were solved. The first phase was an anhydrous oxyresveratrol form whose crystal structure had never been reported. The second phase is a new dihydrated polymorph that is vacuum-sensitive. Thanks to the cryo-plunging sample preparation procedure, data collection was performed, and the H-ORV crystal structure was solved. The procedure for obtaining the pure phases was listed, after which their PXRD patterns fully fitted with a Rietveld refinement procedure. The thermal behaviour of the phases was also fully studied and the different conformations of the oxyresveratrol molecule were found through DFT calculations.

In conclusion, the workflow of our study can be considered as a model that could be applied to the crystal structure characterization of many other natural compounds and for finding their possible new polymorphs.

CHAPTER 5

Crystal structures of oxyresveratrol cocrystals solved using 3D electron diffraction

Background

Mechanochemical synthesis is one of the methods of synthesis identified for crystal engineering of pharmaceutical compounds to form new pharmaceutical compounds with desirable properties. The products obtained after synthesis are powders made up of thousands of single crystals with sizes in the submicron range, whose crystal structures can be solved and analyzed using 3D electron diffraction. The application of 3D electron diffraction on pharmaceutical and organic crystals synthesized using mechanosynthesis has not been fully explored. We take on this task by solving the structures of three cocrystals of oxyresveratrol with coformers: nicotinamide, isonicotinamide, and urea. The structures were successfully solved ab initio using 3D electron diffraction. To validate the reported crystal structures, PXRD Rietveld refinement was performed on the PXRD data using the 3D electron diffraction model as the starting rigid body. Additionally, the different interactions of oxyresveratrol with the coformers in the crystal lattice have also been studied through their non-covalent interactions, crystal packing, and dihedral angles.

5.1. Introduction

In the previous chapter, we discussed the potential application of oxyresveratrol because of its various benefits. Oxyresveratrol (ORV), like some other natural compounds and APIs, has been limited in its therapeutic application due to its low solubility, bioactivity, and low oral availability (Likhitwitayawuid, 2021). In the search for ways to improve the solubility of oxyresveratrol, cocrystallization with various potential GRAS coformershas been identified as a viable option. A successful synthesis of ORV cocrystals was achieved by Suzuki et al. in 2019, who reported the formation of ORV-citric acid and ORV-glutaric acid cocrystals (Suzuki

et al., 2019). In 2020, Ouiyangkul et al. also reported the synthesis of two new ORV cocrystals: ORV-L-proline and ORV-nicotinamide (Ouiyangkul et al., 2020). Finally, in 2021, Sakamoto et al. screened 67 potential coformers and reported the formation of six new oxyresveratrol cocrystals with coformers betaine (ORV-BTN), L-proline (ORV-PRL), isonicotinamide, nicotinamide, urea, and ethyl maltol. In their work, only two of the ORV cocrystal structures were reported: ORV-betaine with a ratio of 2:3 and a hydrated ORV-L-proline with a ratio of 1:2:1. Their crystal structures were solved by SCXRD after first using mechanosynthesis to create cocrystals and then growing single crystals from the nanocrystalline powder produced after mechanosynthesis. They reported an increase in the solubility of the cocrystals when compared to the pure ORV sample. A dissolution test was conducted on the sample for 120 minutes, resulting in the ORV-PRL and ORV-BTN having a dissolution rate of approximately 820µg/ml and 750µg/ml respectively. Oxyresveratrol with urea also showed a dissolution rate of about 700µg/ml while the one with nicotinamide and Isonicotinamide showed a rate of about 680µg/ml and 620µg/ml respectively while the pure oxyresveratrol had a 550µg/ml (Sakamoto et al., 2021).

The crystal structures of the other ORV cocrystals remain were not reported after the mechanosynthesis. Since the ideal crystal sizes for 3D ED crystal structure are in the submicron range, we wanted to uncover the crystal structures of three of the ORV cocrystals using the technique. In this chapter, we report on the crystal structures of cocrystals of oxyresveratrol with nicotinamide (ORV-Nic) and isonicotinamide (ORV-Iso), and urea (ORV-U), solved by 3D ED after mechanosynthesis. Below in Figure 5. 1 are the chemical structures of the ORV together with the coformers used in the cocrystallization.

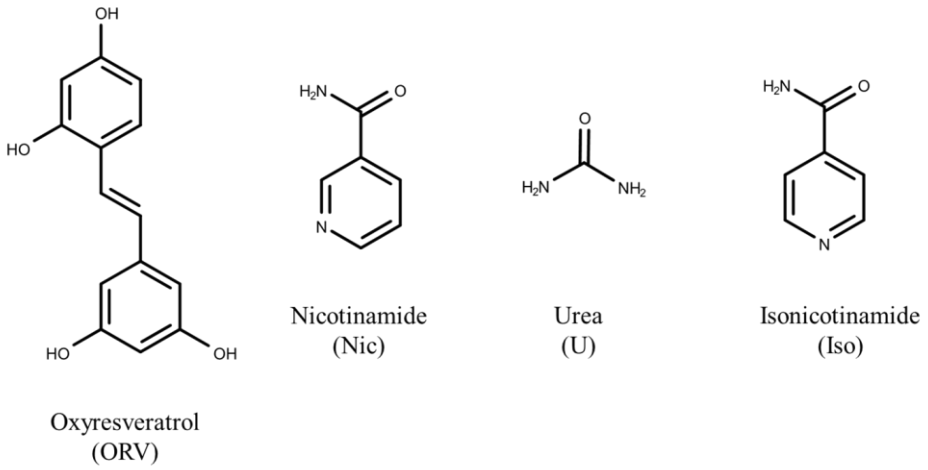

Figure 5. 1. Chemical structure of oxyresveratrol and coformers used in the study with their respective abbreviations

5.2. Mechanosynthesis of ORV Cocrystals

Oxyresveratrol (ORV), nicotinamide (Nic), isonicotinamide (Iso), urea (U), and ethyl acetate were purchased from Sigma Aldrich and used as received. The mechanochemical synthesis of the cocrystals was conducted in a molar ratio of 1:1 for isonicotinamide and nicotinamide, and 1:2 for the oxyresveratrol-urea cocrystals. The synthesis was performed in a Mixer Mill 400 IST (InSolido Technologies) using 14 mL zirconia jars and 2 balls of ZrO_2 (5 mm diameter). The mechanosynthesis was performed using liquid assisted grinding method (LAG) by using ethyl acetate and the mixtures were ground at a frequency of 15 Hz for 40 minutes at room temperature. After grinding, the jars were covered with pinhole parafilm and left to dry under a hood. The phase changes of the cocrystals were monitored using powder X-ray diffraction (PXRD) data.

5.3. Powder X-ray diffraction

PXRD data were acquired using a STOE Stadi P in Debye-Scherrer geometry equipped with Cu-Kα1 radiation (λ = 1.5406 Å), a Ge (111) Johansson monochromator from STOE & Cie and a MYTHEN2 1 K detector from Dectris. All studied samples were loaded in a borosilicate

glass capillary with 0.5 mm external diameter. The data were acquired in the range 3-70 ° 2θ with an interval of 0.03° between consecutive points.

The PXRD patterns from the ORV samples, the respective coformers and the final products after the synthesis were analysed to see if there was a phase change in all the three samples. This was done by comparing their PXRD patterns in the 2θ ranges of 5° to 40°. For the ORV-Nic PXRD pattern, a new peak was observed at 2θ = 5.38º, along with the sharpest peaks at 2θ values of 16.545º, 22.8º, and 25.335º (Figure 5.2a), which were absent in both ORV and Nic PXRD patterns. A new peak was detected at 2θ = 5.41º for ORV-Iso when compared with the starting material, with sharpest peaks at 20.43º, 26.68º, and 25.425º (Figure 5.2b) compared to the PXRD of the precursors. The first visible peak was observed at 2θ = 11.55º for ORV-U, with one characteristic peak at 23.775º (Figure 5.2c). With the observed phase change in the PXRD of the product compared with the precursors, we could conclude that there were new phases present after synthesis.

(a)

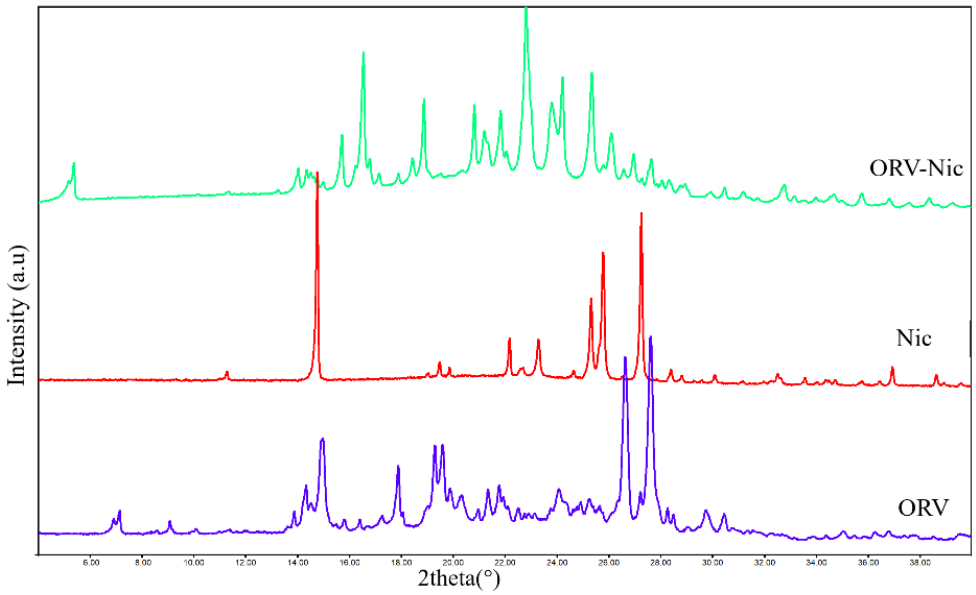

(b)

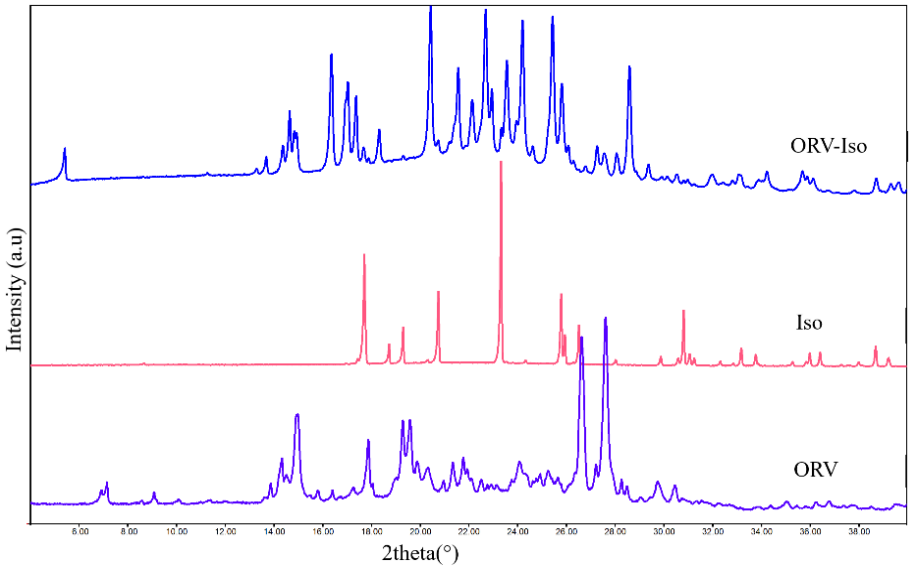

(c)

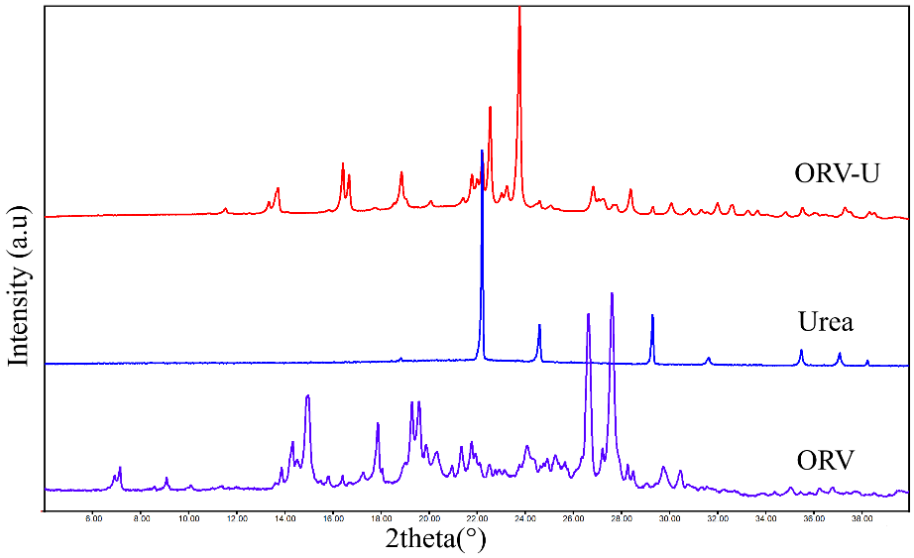

Figure 5. 2 Comparison of the PXRD patterns of the starting precursors and the resultant products. In purple is ORV for all the cocrystals and in (a) ORV-Nic is shown in green with the Nic in red (b) ORV-Iso in blue with Iso in red, and (c) ORV-U is in red with urea in blue.

5.4. 3D Electron Diffraction Analysis

The PXRD analysis confirmed a phase change when compared to the starting materials therefore, the next step was to determine whether the crystal structures of these samples could be obtained using 3D ED and to confirm if they were that of the cocrystals. To collect the data, we had the opportunity to use two different microscopes. The first was our lab microscope, the

Zeiss Libra 120 and the second was the JEOL JEM2100 (thermionic) LaB_6 Transmission Electron Microscope (Stockholm University), which had a 200 kV accelerating voltage. In both microscopes, cRED data collection was automated: *LibraEDT* with the Zeiss and the *Instamatic* software (Smeets et al., 2018) for the JEOL JEM2100. In our microscope, 3D ED was collected in NED mode with a beam size of 570 nm and the crystal search was performed in both STEM and TEM mode, while in the second microscope, a SAED aperture and a beam size of 700 nm was used for diffraction while using TEM mode for the crystal search. The samples were prepared according to the dry sample preparation protocol for room temperature data collection. An average angular tilt range of -60° to +60° with a tilt step of 0.5° was used. All the data were processed with *PETS2*, the structures were solved *ab intio* using *Shelxt* and the dynamical refinement was run in *JANA2020* against $|F|^2$.

5.4.1. Crystal Structure of ORV-Nic Cocrystal

The crystal sizes of the ORV-Nic ranged from approximately 200 nm to 500 nm and appeared to have a rod-like morphology as shown in Figure 5. 3 (right) from images taken in STEM. The crystal search for this sample was done in TEM mode and cRED data collection was done using both microscopes. Since the crystals were relatively stable under the beam, this allowed for more than 20 datasets from both microscopes. All the unit cell parameters found pointed to a=15.770(3) Å, b=7.025(2) Å c=34.342(7) Å, β =97.28(3)º with a unit cell volume of 3773.9(15) $Å^3$ and suggested a monoclinic symmetry. For the space group determination, we evaluated the reciprocal space sections to check for systematic absences (Figure 5.3). The reflection conditions $h+k$ =2n for hkl, and h,l =2n for $h0l$, consistent with the $C1c1$ extinction symbol and the two possible space groups $C2/c$ *or* Cc were observed.

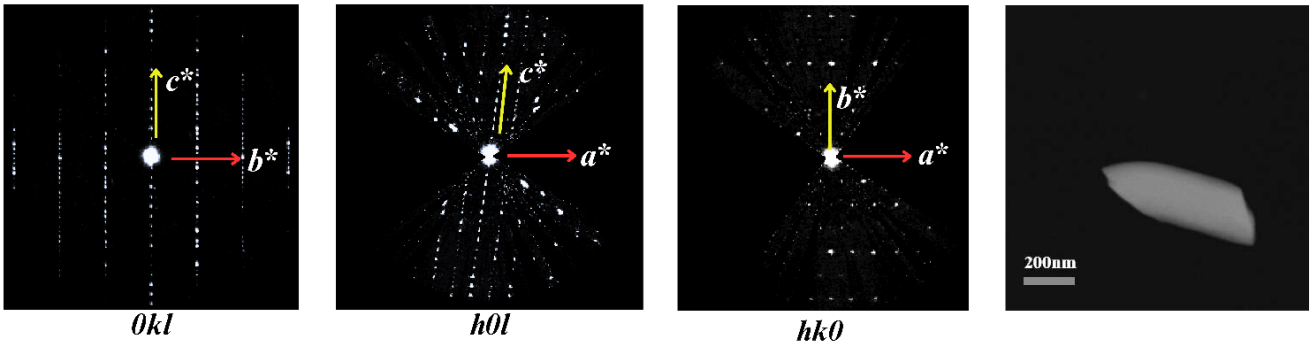

Figure 5. 3 Reciprocal space sections for ORV-Nic 3D ED data with the STEM image of ORV-Nic crystal (right)

The structure of ORV-Nic was solved *ab initio* in a centrosymmetric space group, *C*2/*c*, using *ShelxT*. All the non-H atoms were correctly located in an asymmetric unit formed by one independent molecule of ORV and one of Nic giving then a 1:1 ratio as expected by the ratio of the chemical ingredients. The best data set used for the refinement was from the JEOL JEM2100 microscope. The ORV-Nic structure obtained was refined using dynamical refinement firstly on the non-H atoms, with restraints on bond distances, angles, and the geometry of the aromatic rings of ORV and the pyridine of Nic. Planar restraints were also placed on the two different aryl rings of ORV, as well as on the pyridine ring and amide group of Nic molecule. All the non-H atoms were refined with anisotropic thermal parameters. The H atoms were then automatically added to the structure and refined using a riding model and distance restraints. The refined converged to a final R_{obs} of 10.96% and final crystal structure of ORV-Nic after dynamical refinement, can be seen in Figure 5.4, with the results after the analysis listed in Table 5.2 in the last section of this chapter.

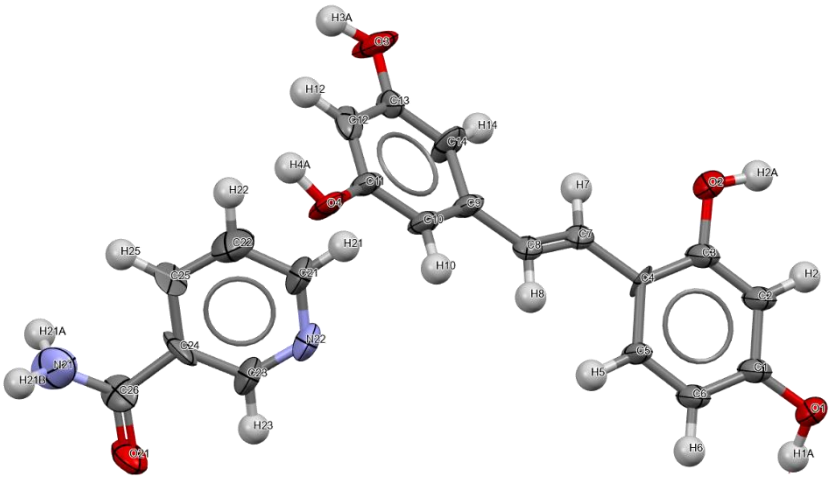

Figure 5. 4 Asymmetric unit of ORV-Nic containing one molecule of ORV and one molecule of Nic. The atoms are represented through their ellipsoids except for the H atoms.

5.4.2. Crystal Structure of ORV-Iso Cocrystal

The data collection on ORV-Iso cocrystal was much more challenging than ORV-Nic, since it was needed to perform the crystal search in low dose STEM crystal search with the Zeiss Libra 120 microscope. In a typical STEM image taken on the ORV-Iso sample (Figure 5.5), the crystals can be seen to be made of layers of thin platelets. After the data were collected on the thin edges of the crystals, the indexing was consistent with unit cell parameters of a=7.067(2) Å b=8.59(2) Å c=16.32(3) Å and angles α=77.28(3)°, β=84.21(3)°, γ=70.59(3)° with a volume of 910.9(4) Å^3. None higher symmetry super cell was found so the structure should be considered triclinic with possible space groups $P1$ or P-1. In Figure 5.5 the three fundamental (0kl, $h0l$, $hk0$) reciprocal sections are displayed.

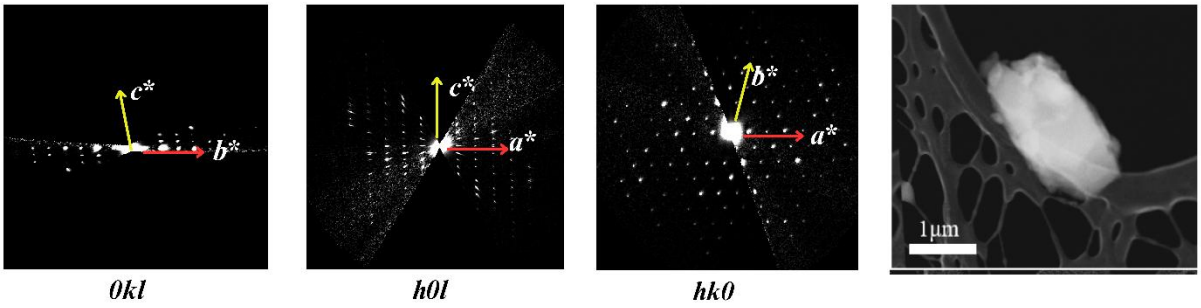

Figure 5. 5 Reciprocal space sections from ORV-Iso and on the right, a STEM image of a typical ORV-Iso grain.

In the next step, the structure was solved *ab intio* in the *P*-1 space group using *Shelxt* obtaining the correct location of all the non-H atoms. In the asymmetric unit, we observed one molecule of ORV and one of Iso hence giving a 1:1 ratio. The positions of all the non-hydrogen atoms were then refined using dynamical refinement with anisotropic thermal parameters. Restraints were placed on the interatomic bond distances, angles, geometry of the benzene rings of the ORV molecule and the pyridine of the Isonicotinamide molecule. A planar restraint was also placed on the aryl group of ORV molecules, the pyridine and amide group of isonicotinamide. After the initial run the hydrogens were added and refined using the riding model with restraints on their distances. The dynamical refinement resulted in a good figure of merit converging with R_{obs}= 11.1%. The asymmetric unit of the final crystal structure of ORV-Iso can be seen in the Figure 5.6 drawn with ellipsoids for the non-H atoms.

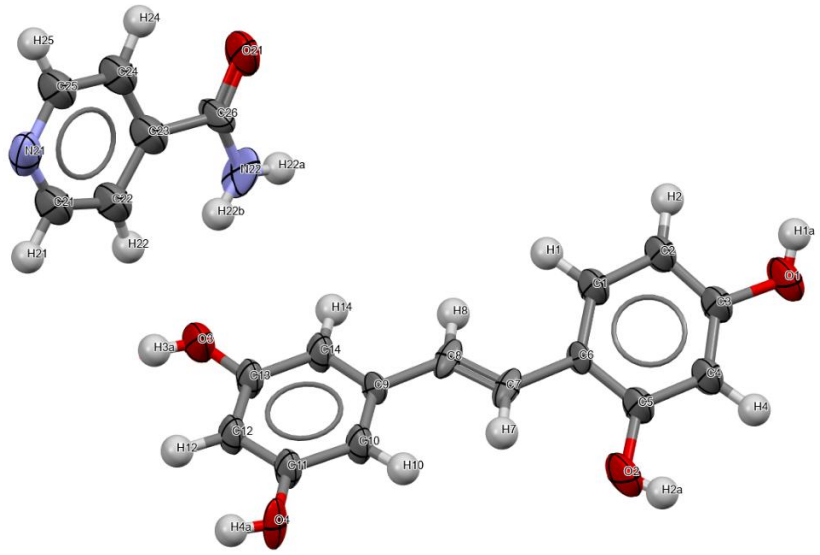

Figure 5. 6 The asymmetric unit of ORV-Iso containing one molecule of ORV and one molecule of Iso.

5.4.3. Crystal Structure of ORV-U Cocrystal

Structure solution data were collected also on ORV-U cocrystal in cRED with the Zeiss Libra 120. ORV-U crystals were slightly beam-sensitive compared to the ORV-Nic sample, but a low dose data collection resulted in some datasets good enough for the indexing and subsequent structure solution. In Figure 5.7, the typical morphology of the ORV-U crystals can be seen

made up of some thin platelets on top of each other with some isolated crystals. Data were therefore collected on isolated thin crystal platelets with sizes in the ranges of 200nm to 500nm (Figure 5.7). After indexing the cRED data sets we saw that ORV-U had unit cell parameters consistent with a= 8.299(2) Å b=8.859(2) Å and c=13.9(3) Å with angles α=76.51(3)° β=78.97(3)° γ= 72.56(3)° and volume of 940.4(4) Å^3. It had triclinic symmetry when the reciprocal space sections were carefully examined, as seen in Figure 5.7.

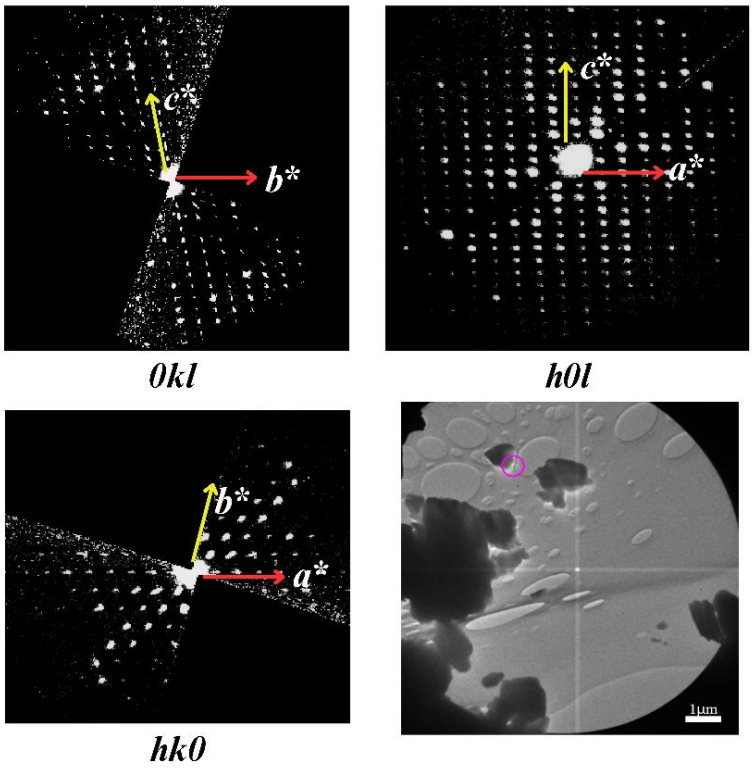

Figure 5. 7 Reciprocal space section of ORV-U after 3D ED data analysis and an image of typical ORV-U crystals taken in TEM mode with the pink circle indicating the approximate beam size for diffraction relative to the crystals

The crystal structure of ORV-U was then solved *ab initio* in the *P*-1 space group using *Shelxt.* The space group is the same as ORV-Iso and with a similar unit cell volume. Interestingly, there appeared to be a ratio of 1:2 between ORV and urea in the asymmetric unit, while the other cocrystals had a ratio of 1:1 between ORV and the correspondent coformers. One dataset was good enough to run dynamical refinement initially on all the non-H atoms which had been correctly located after the structure solution step. Restraints were placed on the interatomic

distances, angles and planarity on both the ORV and urea molecules, then on the geometry of the rings of the ORV to obtain a more accurate structure. The H atoms were added automatically and refined in a riding model with distance restraints for those of urea and angular restraints for those on the OH groups of the ORV molecule. The final model in the asymmetric unit after the refinement with anisotropic thermal parameters can be seen in Figure 5.8. The dynamical refinement converged to an R_{obs} of 11% with the final details about the data collection and refinement in Table 5.2.

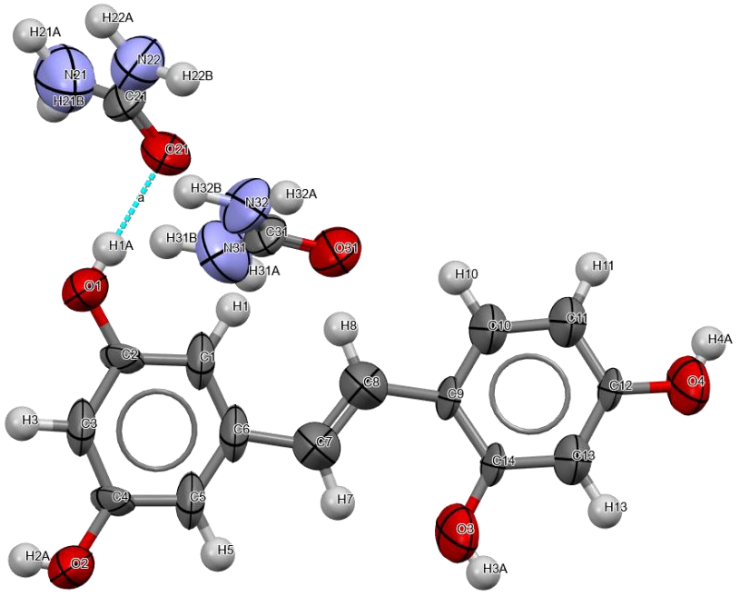

Figure 5. 8 Asymmetric unit of ORV-U containing one molecule of ORV and two molecules of urea

5.5. Comparison of the ORV Cocrystal Structures

After a successful structure solution of all the three cocrystal structures, we thought it to be interesting to compare the crystal packing of the cocrystal structures. Firstly, we observed a similarity between the crystal packing of ORV-Nic in the [010] direction with ORV-Iso [100] direction at first glance. The ORV molecules in both structures we arranged similarly appearing to be alternating with the coformers in layers normal to [001]. The main difference is how the coformers are arranged. In both situations, the coformers interact with each other by π-π stacking apart from the hydrogen bonding interactions between the OH groups of the ORV

molecules and the coformers. Both Nic and Iso are from the same amide group with the main difference being the position of one of the N in the pyridine ring. While in ORV-Iso the Iso molecules are arranged in the same way in each consecutive layer with ribbons of molecules running along [100], with their oxygen atoms pointing alternatively along the positive and negative *a* direction in each ribbon stacked along [010]. In the case of ORV-Nic two consecutive Nic layers are not equivalent: in the first one all the ribbons have the oxygens pointing in the same direction while in the second they point in the opposite. This results in a doubling of the unit cell along both directions with respect to ORV-Iso (see Figure 5.9).

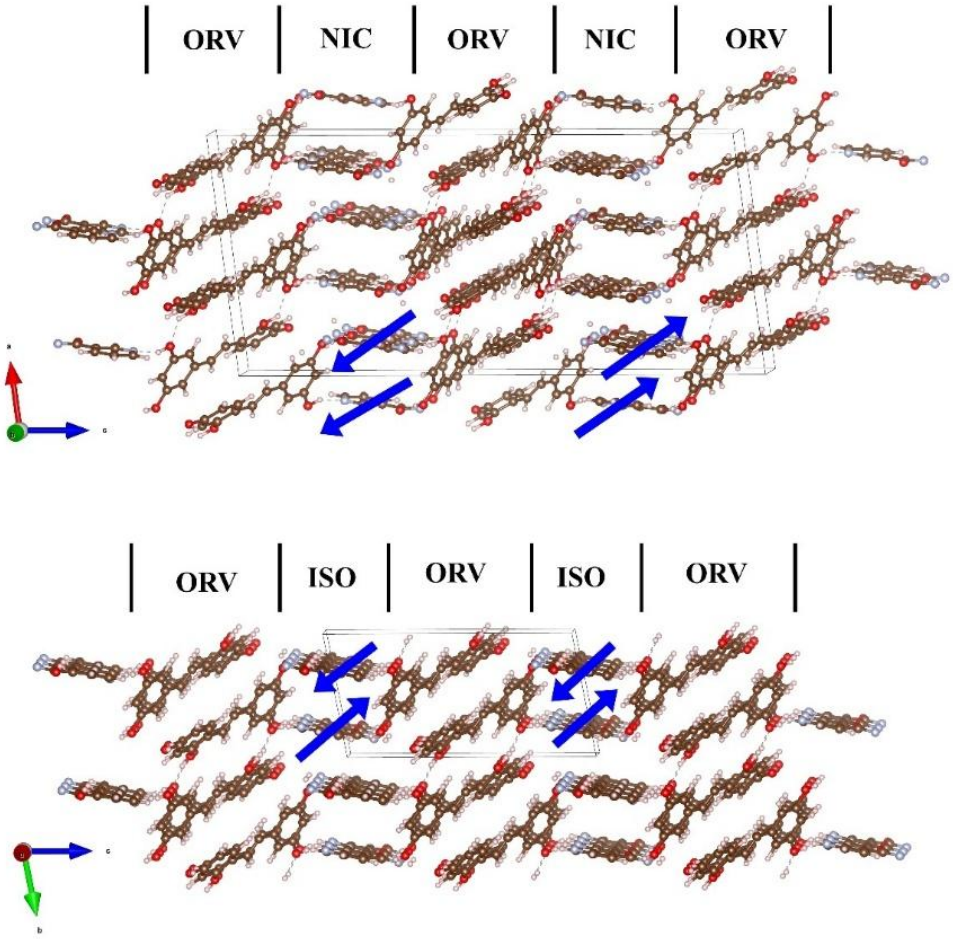

Figure 5. 9 Crystal structure of ORV-Nic is viewed along a direction close to [010] (top) and the crystal structure of ORV-Iso is viewed along a direction close to [100]. The layers formed by ORV and the coformers are indicated at the top of each picture. The blue arrows indicate the directions towards the oxygens of the coformers are pointing.

To compare the crystal packing of all the three ORV cocrystals, we can use the ORV molecules in the structure as the main point of reference to achieve this. Firstly, we can discuss the *conformation* of the ORV molecules in the different cocrystals. We have already established in the previous chapter that the ORV molecule has two conformations (Husanu et al., 2024). We observed that ORV-Nic and ORV-Iso had a conformation 1 while ORV-U cocrystal had the second *conformation*. To better visualize the difference in the molecular arrangement, the structures were viewed along the chains of the ORV molecules. As stated above both ORV-Nic and ORV-Iso have similar arrangement with ORV and the coformers lying in layers. The different setting of the coformers has an influence also in the ORV stacking. For the ORV-Nic, when the structure is viewed on the [1-30] direction, the ORV molecules appear to have layered stacking arrangement with alternate orientation along in adjacent planes with a relative orientation of the molecules of around 90°. These two arrangements of the ORV molecules in the ORV-Nic alternate along the [001] direction. This alternate stacking is absent in ORV-Iso. ORV-Iso viewed along [-210] and ORV-U viewed along [100] have similar crystal packing of the ORV molecules. The arrangement is made up of ORV ribbons moving in the same direction as the coformers in between them. The main difference between the two is that in the ORV-U, the coformers lie on the same plane as the ORV chains and form face-to-face dimers, while in ORV-Iso the ORV and the Iso are perpendicular to each other, they lie on different planes (Figure 5.10). Hydrogen bonding is seen between all four of the hydroxyl groups of the ORV molecules with the coformers bonding with the distance between 2.6 Å to 3 Å.

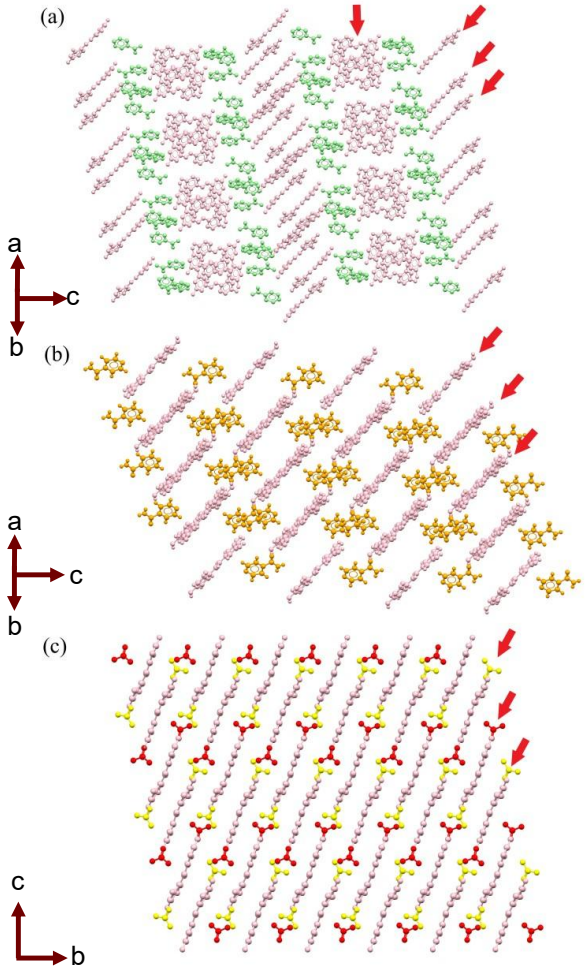

Figure 5. 10 Crystal packing of the three cocrystals structures viewed along the ORV molecule planes with a focus on the different arrangement of the ORV molecules (in pink for the three cocrystal structures) (a) ORV-Nic viewed along [1-30] and (b) ORV-Iso viewed along [-210] (c) ORV-U [100] directions.

Due to the flexibility of the ORV molecule, the aryl group can lie on slightly different planes measured by their dihedral angle. The dihedral angles of the ORV cocrystals were measured and compared with the ones existing in the reported structures.

Dihedral Angles comparison of aryl groups in Oxyresveratrol		
Cocrystals/Compound	Angle (°)	Source
Oxyresveratrol-Nicotinamide (**ORV-Nic**)	31.21 (3)	*This work*
Oxyresveratrol-Isonicotinamide (**ORV-Iso**)	26.18 (2)	
Oxyresveratrol-Urea (**ORV-U**)	13.06 (2)	
Hydrated oxyresveratrol (**ZAPDOL**)	9.39 (9)	*Deng et al, 2012*
Monohydrate bis(proline) oxyresveratrol (**YUYDAA**)	7.1 (2)	*Ouiyangkul et al 2020*
Bis (proline) oxyresveratrol (**YUYDEE**)	14.15 (19)	

Table 5. 1 Dihedral angles of ORV comparison

5.6. Rietveld Refinement of ORV Cocrystals

Given the 3D ED model obtained from the single nanocrystals, we had to check if the model was representative of the powder obtained after the mechanochemical synthesis at ambient conditions. To do this, Rietveld refinement was performed on the experimental PXRD data of all the cocrystals. In all three PXRD data sets, the refinements were carried out in a 2θ range of 3° to 90°. *Topas Academic* (Coelho, 2018) was the software of choice for refinement. The 3D ED models were used as a starting rigid body with their respective lattice parameters being used before refining. The molecules were refined as semirigid bodies, and the torsion angles related to single bonds in ORV, Nic and Iso were freely refined. This allowed for the rotation of the flexible parts of the molecules to move to ensure more accurate structures.

5.6.1. Rietveld refinement of ORV Nic

ORV-Nic the same space group *C*2/*c* was used in the refinement, however, there was a slight difference in the volume of the cell from 3773.9(15) $Å^3$ to 3577.6(4) $Å^3$. The resulting cell parameters were a=15.7331(8) Å b=6.9488(6) Å c=33.069(2) Å and β= 98.283(3)°. The resulting profile fit is seen in Figure 5.11 after the Rietveld refinement. The model obtained after refining the structure against the PXRD is overlayed with the 3D ED structural model in Figure 5.12 . The Retvield refinement resulted in an Rw_p of 4.56% confirming the presence of the ORV Nic phase in the sample.

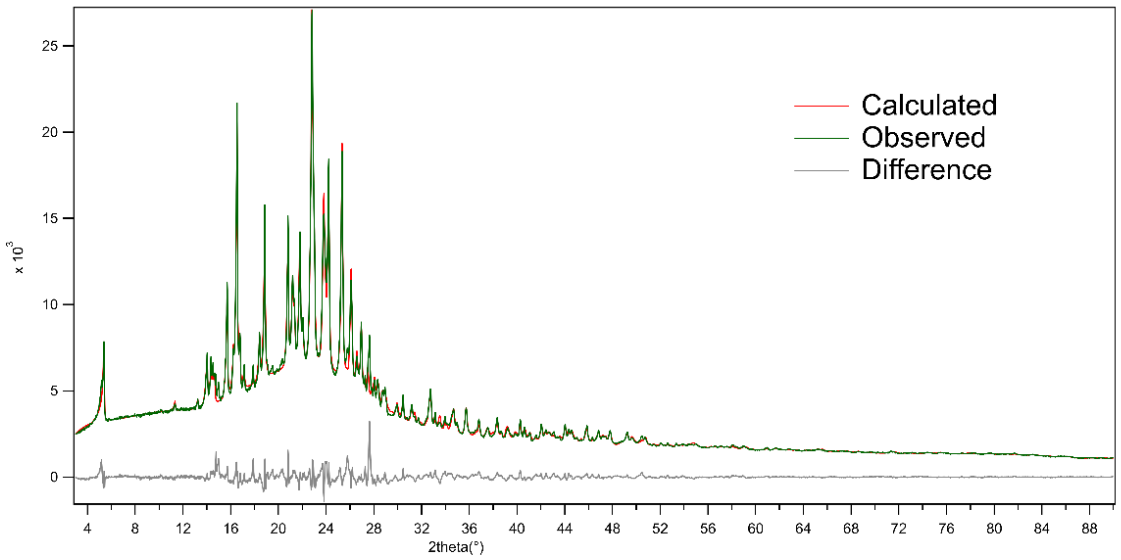

Figure 5. 11 Profile fit after Rietveld refinement of ORV-Nic model against PXRD data

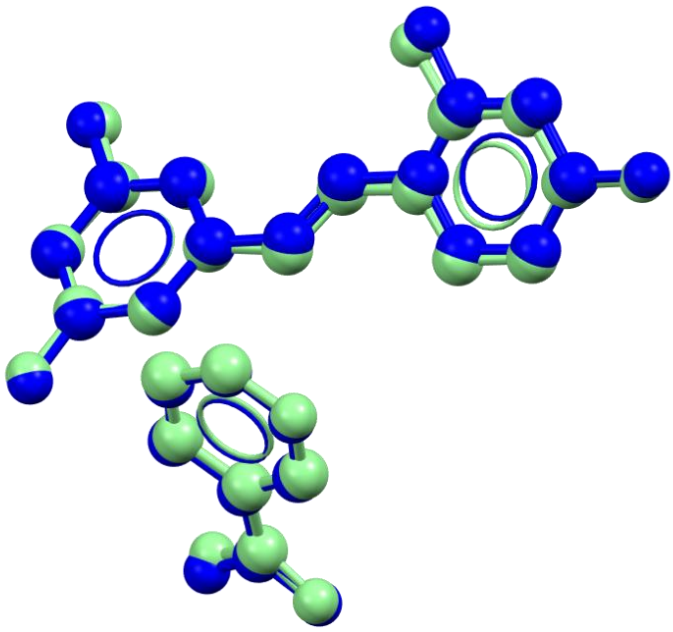

Figure 5. 12 Crystal structure overlay of the 3D ED model (blue) and the model obtained after Rietveld refinement (blue) of ORV-Nic

5.6.2. Rietveld refinement of ORV-Iso

The presence of the ORV Nic phase obtained from 3D ED was confirmed with a profile fit in the *P*-1 space group which resulted in an R_{wp} 5.34% after the Rietveld refinement. We did also observe a cell volume of 881.03(9) Å^3 from the volume of 910.9(4) Å^3. The resulting cell parameters were *a*=6.8369(5) Å *b*=8.3943(4) Å *c*=16.5123(9) Å with angles *α*=79.874(3)°

β=85.756(3)° γ=70.828(3)°. In Figure 5.12, we can see the profile fit of the observed against the calculated after the Rietveld refinement. A structural overlay was done to compare the model obtained from 3D ED to the refined structure against the PXRD data shown in Figure 5.14.

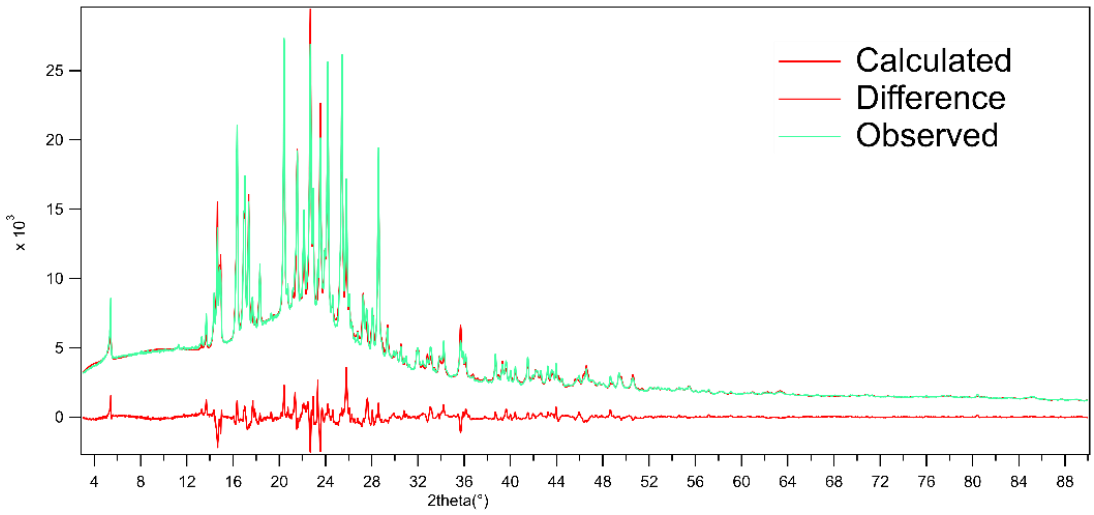

Figure 5. 13 Profile fit after Rietveld refinement of ORV-Iso model against PXRD data

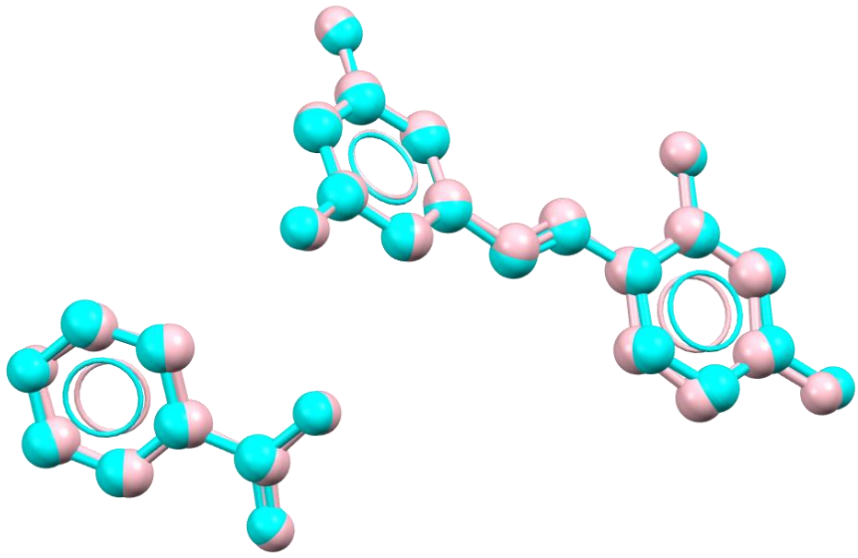

Figure 5. 14 Crystal structure overlay of the 3D ED model (pink) and the model obtained after Rietveld refinement (blue) of ORV-Iso

5.6.3. Rietveld refinement of ORV-U

A successful refinement was achieved with our starting 3D ED model confirmingthe presence of the ORV U phase in the sample. The refinement converged to an R_{wp} of 6.44% in the *P*-1

space group. Here, again, we also see a slight change in the cell volume from 940.4(4) $Å^3$ to 877.68(5) $Å^3$ after the refinement. The cell parameters obtained a=8.0490(2) Å b=8.5759(2) Å c=13.6575(6) Å with angles of α= 78.332(3)° β =79.240(3)° γ =73.710(4)°. The PXRD profile of the observed against the calculated can be seen in Figure 5.13 and an overlay of the 3D ED model and the model obtained after Rietveld refinement (5.16) below.

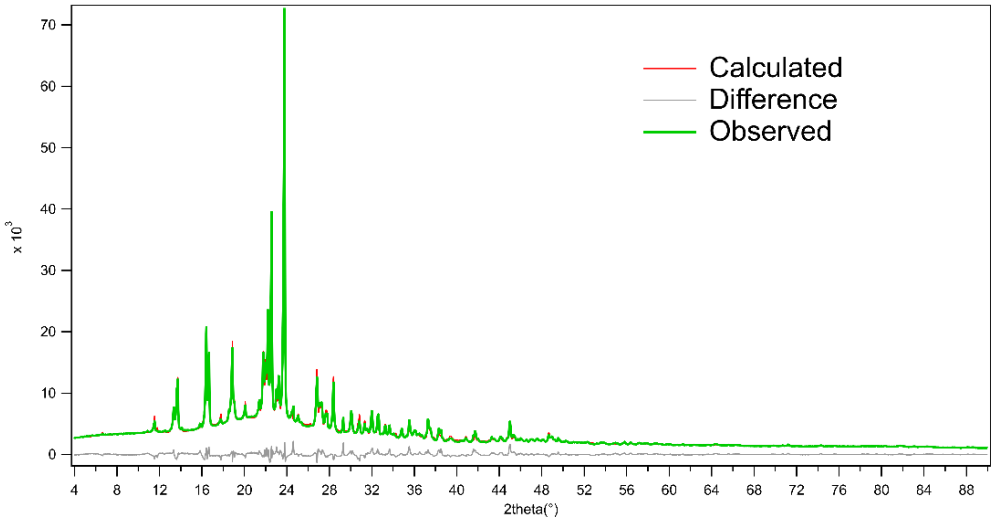

Figure 5. 15 Profile fit from Rietveld refinement of ORV-U model against PXRD data

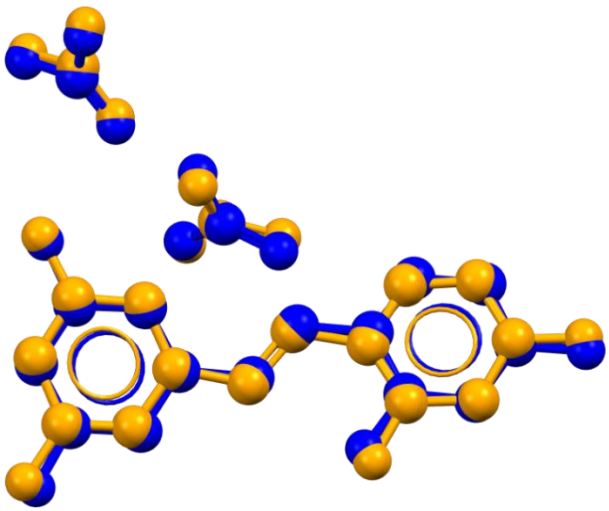

Figure 5. 16 Crystal structure overlay of the 3D ED model (orange) and the model obtained after Rietveld refinement (blue) of ORV-U

Experimental details	Oxyresveratrol-Nicotinamide (ORV-Nic)	Oxyresveratrol-Isonicotinamide (ORV-Iso)	Oxyresveratrol-Urea (ORV-U)
Chemical formula	$C_{20}H_{28}N_2O_5$	$C_{20}H_{16}N_2O_{10}$	$C_{16}H_{20}N_4O_6$
Crystal system, Space group	Monoclinic, *C2/c*	Triclinic, *P*-1	Triclinic, *P*-1
Temperature (K)	293	293	293
a, *b*, *c* (Å)	15.770 (3), 7.025 (2), 34.342 (7)	7.067 (2), 8.591 (2), 16.315 (3)	8.299 (2), 8.859 (2), 13.907 (3)
α, β, γ (°)	90, 97.28 (3),90	77.28 (3), 84.21 (3), 70.59 (3)	76.51 (3), 78.97 (3), 72.56 (3)
Volume (Å^3)	3773.9 (15)	910.9 (4)	940.4 (4)
Transmission Electron Microscope (TEM.) type	Joel 2100F	Zeiss Libra 120	Zeiss Libra 120
Radiation type	Electron, λ = 0.02508 Å	Electron, λ = 0.0335 Å	Electron, λ = 0.0335 Å
Tilt range (°)	120	110	100
Data resolution (Å)	1.25	1.4	1.4
Dynamical refinement			
No. of measured, independent and observed reflections	21745, 4560, 1287	23836, 5148, 1106	8720, 2624, 1085
Parameters	232	183	72
$(\sin\theta/\lambda)_{max}$ (Å^{-1})	0.75	0.620	0.474
Thickness (nm)	440	304.98	404
R_{obs}, wR_{obs} (%), *S*	10.96, 21.46, 1.6433	11.1, 22.7, 1.67	11, 21.8, 2.47
Δρmax, Δρmin (e Å^{-3})	0.19, -015	0.16, -0.12	0.10, -0.10

Table 5. 2 Table S2. Selected parameters after data collection and dynamical refinement

Conclusion

3D electron diffraction has played a significant role in the structure determination of small molecules, especially for organic and pharmaceutical nanocrystals. Mechanosynthesis is a method of synthesis of small molecules such as cocrystals and leads to the formation of submicron crystals. It is important to address the problem of the structure determination of powder samples obtained with this method of synthesis which plays a significant role in crystal engineering of pharmaceutical products. A successful *ab initio* crystal structure solution of cocrystals of ORV with nicotinamide, isonicotinamide and urea of nanosized single crystals synthesized using mechanosynthesis was done by exploring the 3DED combined with PXRD as powerful tools. We have shown that 3D ED can be used for solving structures of crystals obtained by mechanosynthesis.

CHAPTER 6

Serial Electron Diffraction on Beam-Sensitive Organic Nanocrystals

Background

Organic nanocrystals very often have shown beam sensitivity, which is expressed by the loss of the high-resolution intensities during a 3D ED data acquisition. A proposed data collection method called Serial electron diffraction (SerialED) was introduced in Chapter 2. In this chapter, this method of diffraction data acquisition was applied to a pharmaceutical API called Levodopa or L-Dopa whose crystal structure is already known in literature as a test of the technique. After a long data collection, the data was processed and the crystal structure of the L-Dopa was solved ab initio using SerialED. In this work, we present the preliminary results of what could be a way of applying SerialED on pharmaceutical nanocrystals that are too beam-sensitive for 3D ED.

6.1. Introduction

The concept of serial crystallography involves collecting one diffraction pattern per crystal on tens of thousands of crystals which are very beam-sensitive (Chapman et al., 2011). This is based on the idea of obtaining diffraction from the samples before their degradation has time to occur, so the data are collected in very fast single shots (Chapman et al., 2014) (Zhu et al., 2020). This technique was originally developed for data collection on synchrotron radiation facilities or X-ray Free-Electron Lasers (XFELs) which are either not easily accessible or expensive to operate.

The ED in a TEM is a possible alternative technique to be used in the SerialED approach that in principle is affordable for a relatively small lab. It is used in many research institutions and universities and has components that are customizable to perform such experiments.

Advantages such as having the ability to change: the beam sizes, the different movements of the stage and the beam dose, provide the opportunity to perform SerialED in a quite flexible way. Although 3D ED has proven useful for unveiling the crystal structures of numerous materials, there are some limitations for beam-sensitive materials such as MOFs, macromolecules and organic nanocrystals. SerialED has the potential to expand and fill some of these gaps in the application of 3D ED. Some work, however, has already been done using SerialED but the technique has remained not widely used (Bücker et al., 2021; Hogan-Lamarre et al., 2024; Smeets et al., 2018). This is because processing of all the tens of thousands of randomly oriented frames comes with some challenges. To index the frames, the unit cell parameters must already be known. since each frame almost contains only 2D information. However, if for some reason the cell unit cell is known, for example, it can be taken from literature or from a short 3D ED analysis the indexing step can be simplified.

This chapter will therefore focus on the application of SerialED for solving the crystal structure of L-Dopa as a preliminary work on applying the technique to an organic sample.

6.2. Sample preparation and data acquisition

The sample preparation method used followed the room temperature dry sample protocol listed in Chapter 2, however this time, more crystals were loaded onto the grid, compared to sample preparation for 3D ED, to ensure that data could be collected on the many crystals.

The data collection follows a similar protocol to the one used in serial crystallography with a fixed target. To acquire the data, *LibraEDT* software was used which has a SerialED data collection section added recently. The interface of the software can be seen in Figure 6.1 and contains four main panels, one of which is dedicated to SerialED. In this panel, several parameters must be inserted, which determines the scanning procedure of the sample, and which collected patterns must be retained and saved avoiding disk space overflow. Firstly, the beam is located on a few crystals and the diffraction patterns are collected to determine the

threshold parameters. For example, if the ‘Peaks’ value is set to 3, ‘d_max’ is set to $Å^{-1}$ and ‘I/Sig’ is set to 5, only frames with more than 3 reflection peaks beyond the 1.25 Åresolution having an intensity-over-sigma ratio larger than 5 are saved. This ensures that only high-quality and high-resolution data are saved during the data collection. Before starting the data collection, the areas that will be scanned for the data collection are selected through a panel that displays a sketch of the entire grid (Figure 6 top left, TEM stage map). During the data collection, the recorded patterns can be seen live on a window with the resolution rings drawn on top. In the last window, the number of all the frames saved out of all the frames collected is displayed. Data collection can take up to 10 hours and is performed by the detector recording patterns while the stage is continuously moving. A typical example can be the stage moving at a speed of 10 μm/s and an exposure time of 150 ms giving a frame-to-frame displacement of 1.5 μm, which should correspond to the average crystal size in the sample. A data collection of 10 hours, depending on the quality of the frames, can range between 6000-10000 retained patterns or more with a total of more 200,000 captured frames.

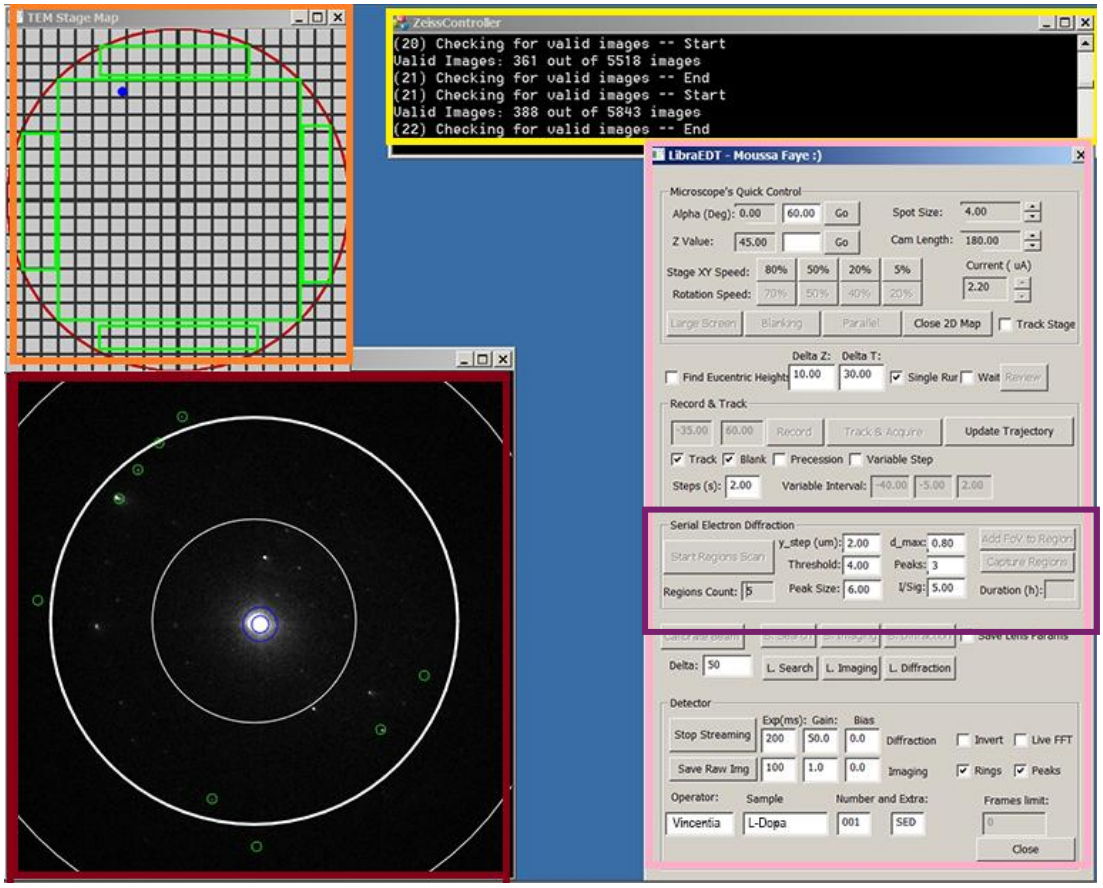

Figure 6. 1 The interface of the LibraEDT software for the data collection of SerialED data with highlights on the different windows. The orange window shows the grid, with the green highlighting the selected areas on the grid that will be mapped. The blue dot shows the position of the beam at the actual point of the data collection. The yellow shows the log of the number of images saved and the total number of images collected. In the large pink window, we see the data collection parameters. A smaller box in purple shows the settings needed for the SerialED data collection. Lastly in the red, the diffraction patterns collected can be seen with the resolution rings in white and the detected spots in green circles.

6.3. Processing of SerialED Data

The workflow of SerialED data processing is displayed in Figure 6.2. The critical step of the entire procedure is the indexing process. The software *CrystFEL* (White et al., 2012) is the most used for this step in the case of X-ray data. Bücker et. al. in 2021 used *CrystFEL* to process SerialED data using *diffractem* (Bücker et al., 2021). Other data software such as *nXDS* (Kabsch, 2014) a package from the *XDS* software suite for processing serial crystallography data, is also adaptable for SerialED data. 3D ED data processing software, *PETS2* has also

SerialED data processing software capabilities. In this work, the data were processed using the *nXDS* data processing software. The following section will list how the input file for *nXDS* is prepared for data analysis of L-Dopa. The next steps, which are structure determination and refinement follow the same routine as in 3D ED. The workflow for data processing, structure solution and refinement can be seen in Figure 6.2.

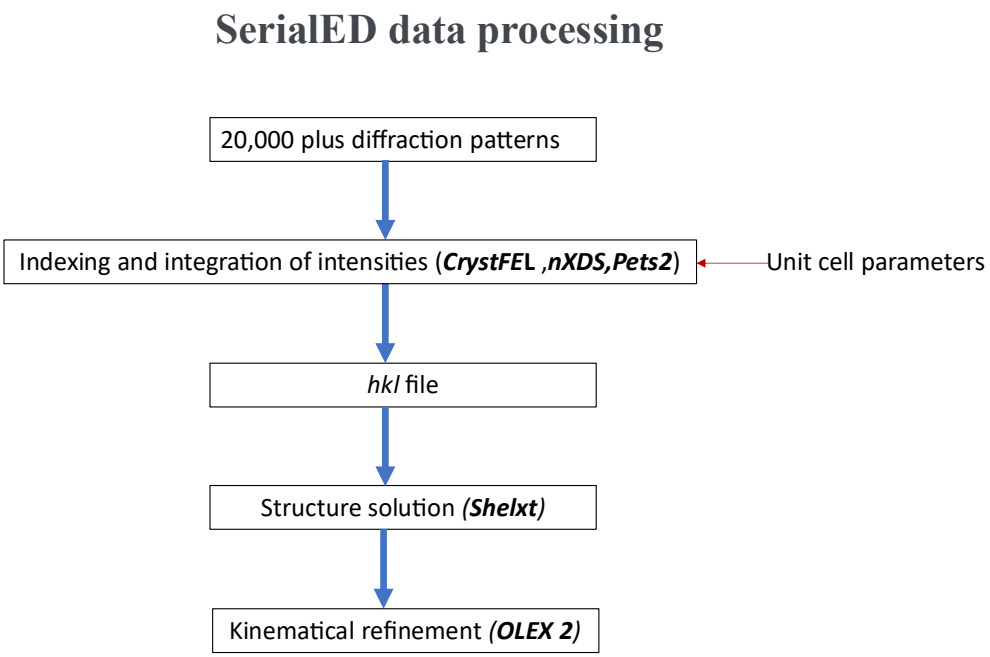

Figure 6. 2 Workflow for data processing of SerialED data

6.4. Serial Electron Diffraction on L-Dopa

The sample selected for the SerialED analysis was L-Dopa or L-3,4-dihydroxyphenylalanine whose crystal structure has already been reported in literature (A. Mostad et al., 1971) (Figure 6.3). To start the analysis, 3D ED data were collected on the L-Dopa sample. This sample although diffracted nicely at the start of the data collection, lost some of the high-resolution reflection after exposure to the electron beam in about 3 seconds which made it an ideal candidate for the SerialED data collection. The 3D ED data collected were sufficient for the unit cell determination which resulted in a monoclinic space group with a=13.093(3) Å

b=5.3560(11) Å *c*=6.1840(12) Å with *β*=90.733(3)° showing extinctions compatible with space group $P2_1$ and unit cell parameters similar to what was reported in the literature.

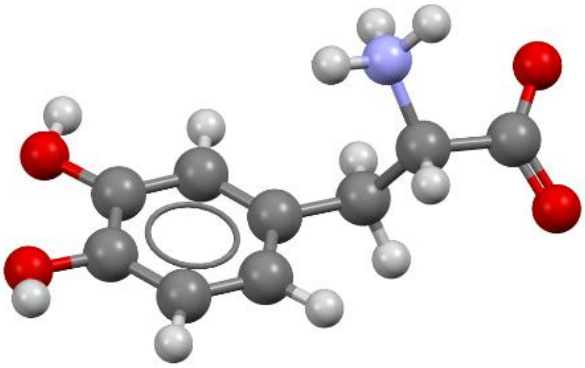

Figure 6. 3 Crystal structure of L-Dopa

The unit cell parameters obtained from the 3D ED analysis were then used in the data processing using *nXDS*.

For the data collection, the sample was prepared as described earlier. Figure 6.4 below shows the morphology of the L-Dopa crystals ranging in size between 300 nm to 1000 nm.

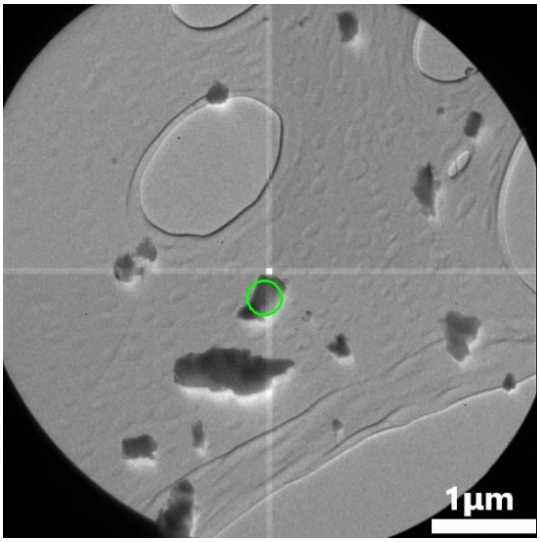

Figure 6. 4 Typical morphology of the L-Dopa crystals with sizes between 300nm to 500nm taken in TEM mode

After a fast check that the crystals were uniformly distributed on the grid and an optimization of the collecting parameters on a few selected crystals, the data collection was started. The data acquisition parameters in the case of L-Dopa are listed in Table 6.1. To ensure the

maximum variety of the orientations, a 10° rotation of the stage was performed after every 2000 frames retained. In total, about 40,000 diffraction patterns were collected for a total experiment time of 15 hours in which the TEM collected data completely unsupervised (most of the experiment was carried out overnight). Typical diffraction patterns that were saved can be seen in Figure 6.5

Parameter	**Value**
Data Acquisition Software	LibraEDT
Data Acquisition Mode	Stage movement
Acquisition Duration	≈ 15 hours
Stage Movement Speed	20 μm/second
Exposure Time	50 ms per frame
Total Images Captured	over 200,000
Retained Frames	40,000
Filtering Conditions	At least 7 peaks with I/σ > 4 and resolution higher than 1.25 Å

Table 6. 1 Parameters that were set for the SerialED data collection of L-Dopa

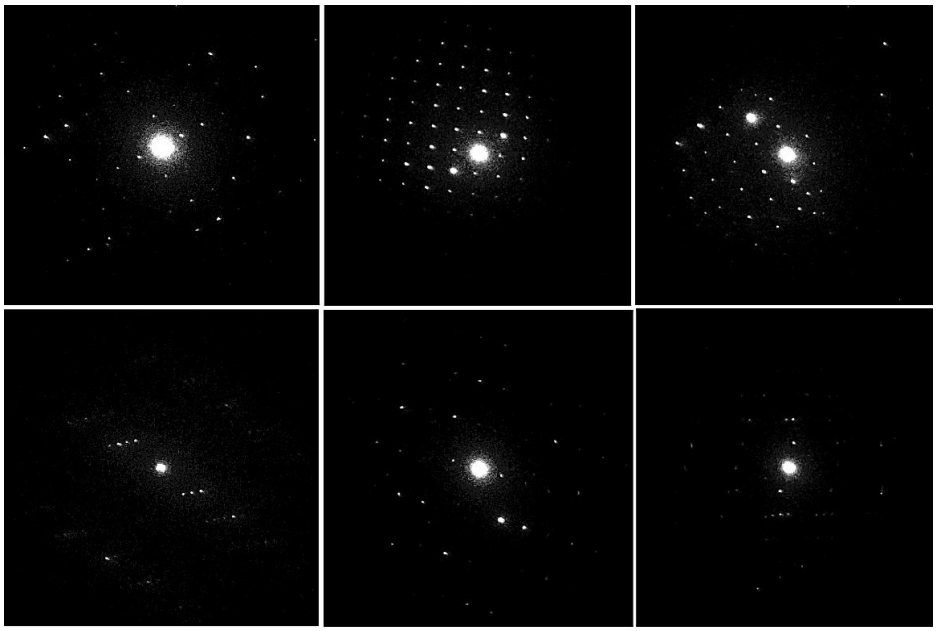

Figure 6. 5 Six diffraction patterns randomly selected from the data sets that were kept during the data collection by the LibraEDT software

6.5. Data Processing using *nXDS*

Similarly to *XDS, nXDS* requires an input file, *nXDS.INP,* which contains all the parameters including the wavelength. The diffraction patterns are uploaded in a specified directory where the software is launched. The JOB line in the input contains a line of tasks that are run which are *XYCORR, INIT, COLSPOT, IDXREF, DEFPIX,* and *INTEGRATE.* The first task that is run is the *XYCORR* which picks up the strong reflections based on the peak search values set in the input file. These values are set in the *MINIMUM_NUMBER_OF_SPOTS* line set to 5 in this data set. The *IDXREF* task is then run to determine the orientation of each diffraction pattern. This is done by refining the crystal orientations based on the given unit cell for each frame in other to index all the reflections present in the frames. This step is successful for all the frames and the success or not of the indexing is controlled by the '*MINIMUM FRACTION OF INDEXED SPOTS'* which was set to 0.4 in our case. This resulted in a total of 2900 successfully indexed frames. Once the indexing has been completed the next step is the integration of intensities, performed in the task called *INTEGRATE.* The last step is the *CORRECT* step in which the scaling and error calculations are performed. A typical input file of *nXDS* can be seen in Figure 6.6

```
!REFLECTING_RANGE_E.S.D.=
NUMBER_OF_PROFILE_GRID_POINTS_ALONG_ALPHA/BETA= 13
MINPK= 70.0 ! MINIMUM REQUIRED PERCENTAGE OF RECORDED INTENSITY
!CUT= 2.0    ! CUT-OFF VALUE DEFINING THE INTEGRATION REGION
PROFILE_FITTING= TRUE ! TRUE            !# Profile Fitting or sum counts.
MINIMUM_ZETA= 0.05
MAXIMUM_ERROR_OF_SPOT_POSITION= 10.0      !# Increase this to increase the tolerance between observed and calculated reflections positions, for better

!============== CORRECT
MINIMUM_EWALD_OFFSET_CORRECTION= 0.2 ! CORRECT
POSTREFINE= SKALA BEAM ORIENTATION CELL POSITION B-FACTOR ! MOSAICITY      !# Refining the mosaicity in this step resulted in a crash
!REFERENCE_DATA_SET=../xds11/XDS_ASCII.HKL
!USE_REFERENCE_IN_POSTREFINEMENT=TRUE ! FALSE is default
FRIEDEL'S_LAW= TRUE ! FALSE
!MERGE=FALSE ! TRUE is default
MAX_CELL_AXIS_ERROR= 0.5
MAX_CELL_ANGLE_ERROR= 4.0
!REJECT_ALIEN= 20.0

!============== CRYSTAL
SPACE_GROUP_NUMBER= 4               !# Usually guessing any space group that belongs to the correct laue class is OK
UNIT_CELL_CONSTANTS= 13.0931    5.3564    6.1840   90.0000   97.2165   90.0000 !# The lattice parameters of the system

!============== ROTATION PARAMETERS
!ROTATION_AXIS=0.93051 -0.36627 0.00000   !# For Serial Data, this is not needed.
OSCILLATION_RANGE=0.0                     !# For Serial Data with still images, the oscillation range is ZERO

!============== BEAM PARAMETERS
X-RAY_WAVELENGTH=0.03350            !# Electron Wavelength in Angrstroem
INCIDENT_BEAM_DIRECTION=0 0 1
FRACTION_OF_POLARIZATION=0.5
!UNTRUSTED_ELLIPSE=
!UNTRUSTED_RECTANGLE=
!UNTRUSTED_QUADRILATERAL=
!MINIMUM_FRACTION_OF_BACKGROUND_REGION= 0.01
NBX= 4
NBY= 4

!============ COLSPOT
BACKGROUND_PIXEL= 100.0  ! maximum signal/noise (COLSPOT, INTEGRATE)
SIGNAL_PIXEL= 4    ! minimum signal/noise (COLSPOT, INTEGRATE)
MINIMUM_NUMBER_OF_PIXELS_IN_A_SPOT=3
MINIMUM_NUMBER_OF_SPOTS=5      ! per image

!============ POWDER
!POWDER_CENTER_CORRECTION= 0.0 0.0 0.001 ! dx dy (pixel) q (radian)

!============ IDXREF
REFINE(IDXREF)= BEAM ORIENTATION CELL  ! POSITION
!RGRID=-1.0   ! histogram grid size (rec. A) for locating difference vectors
!SEPMIN=6.0   ! minimum length (pixels) of difference vectors
!CLUSTER_RADIUS=3.0 ! radius of a difference vector cluster (pixels)
!MAXIMUM_NUMBER_OF_DIFFERENCE_VECTOR_CLUSTERS= 30
!MERGE_TREE=0.1
!INTEGER_ERROR=0.1 ! max. allowed deviation of cluster indices from integers
!NUMBER_OF_TESTED_BASIS_ORIENTATIONS=1000000
INDEX_ERROR= 0.05                                                                                                    ze
INDEX_MAGNITUDE=10
INDEX_QUALITY= 0.7
MINIMUM_FRACTION_OF_INDEXED_SPOTS= 0.4 !# Keep the frame only if at least a certain proportion of the reflections were correctly indexed.

!============ INTEGRATE
INCLUDE_RESOLUTION_RANGE= 20.0 0.80   ! INTEGRATE, CORRECT   !# Resolution Range
!BEAM_DIVERGENCE=
!BEAM_DIVERGENCE_E.S.D.=
!******************************************************************************
! List of the possible input parameters that can be used in file nXDS.INP
! Characters in a line to the right of an exclamation mark are comment.
!******************************************************************************

!******************************************************************************
!******************************************************************************
! Adapted for Serial Electron Diffraction Data by Moussa Faye, December 2024
!******************************************************************************
!******************************************************************************

!============ JOB CONTROL
!JOB= XYCORR INIT COLSPOT POWDER IDXREF INTEGRATE CORRECT
!JOB= XYCORR INIT COLSPOT
!JOB= POWDER IDXREF
JOB= INTEGRATE CORRECT
!JOB= CORRECT
!JOB= XYCORR INIT COLSPOT POWDER IDXREF

MAXIMUM_NUMBER_OF_PROCESSORS=14
MAXIMUM_NUMBER_OF_JOBS=14            ! # main programs
!CLUSTER_NODES=bragg01 bragg02 bragg03 bragg04 bragg05 bragg06 bragg07 bragg08
!IMAGE_DIRECTORY=../0000000???.tiff              ! Contains images
NAME_TEMPLATE_OF_DATA_FRAMES= ../?????.tiff
DATA_RANGE=2 44266
!EXCLUDE_DATA_RANGE= 14393 20000
!SECONDS= 0                          ! # seconds to wait for image
!TEST= 15                            ! for testing image reading routine
VERBOSE=0                           ! 0: short listing; 1:long; >1:debug

!============ INIT
BACKGROUND_RANGE= 22000 23000! 30000 35000
!DARK_CURRENT_IMAGE=
!OFFSET= 0.0
!TRUSTED_REGION=0.0 2.0 !Relative radii limiting trusted detector region
```

Figure 6. 6 Input file for nXDS for the SerialED data processing of L-Dopa

The resulting statistics after the data processing of our data are listed in Table 6.2. The data are grouped in different resolution shells (each indicated by the resolution in Å in the *RESLIM*

column) with the corresponding figures of merits and completeness. The resulting output file is an *.hkl* that can then be used for the subsequent structure solution step.

RESLIM	OBSERVED	UNIQUE	POSSIBLE	COMPLETE	I/SIGMA	CHI-test	Rmrgd-F	CC(1/2)	NFREE	Zano	N-	N+
4.205	5465	9	9	100.0	9.2	0.616	5.5	97.5*	10	0.50	0	1
3.036	7406	14	14	100.0	11.9	1.390	8.2	92.5*	21	-0.57	5	2
2.497	5746	16	16	100.0	6.1	1.006	13.3	91.3*	25	0.71	2	6
2.170	6680	20	20	100.0	6.8	1.049	13.2	84.2*	35	-0.65	10	5
1.945	5400	20	20	100.0	5.3	1.164	17.7	91.7*	32	1.06	1	7
1.778	5517	25	25	100.0	4.4	0.702	13.6	87.4*	43	0.87	3	9
1.648	4450	23	23	100.0	4.6	1.049	19.4	82.2*	39	0.29	5	7
1.543	4234	27	27	100.0	4.0	0.938	20.8	68.7*	49	1.07	3	11
1.456	4315	31	31	100.0	3.6	0.816	20.6	74.8*	52	1.06	2	9
1.382	2560	22	22	100.0	3.3	0.840	20.9	70.8*	37	-0.67	4	1
1.318	3316	31	31	100.0	3.3	0.840	22.1	73.3*	57	0.45	4	7
1.262	3121	31	31	100.0	3.0	0.726	21.0	80.3*	56	0.35	3	5
1.213	3305	37	37	100.0	3.4	0.890	25.2	60.0*	66	0.17	4	5
1.169	3053	33	33	100.0	3.5	0.995	25.5	73.6*	58	0.15	5	6
1.130	2313	36	36	100.0	3.1	0.741	23.7	65.4*	66	-0.57	5	2
1.094	2183	35	35	100.0	3.1	0.901	23.3	64.1*	65	-0.17	5	4
1.062	1551	32	32	100.0	2.6	0.952	34.9	64.1*	57	0.00	1	1

Table 6. 2 Final statistics after analysis of the SerialED data of L-Dopa in nXDS

6.6. Structure Solution and Refinement

The structure of L-Dopa was solved fully *ab initio* using *ShelxD* (Schneider & Sheldrick, 2002). All the non-H atoms in the structure were found, but their chemical species were not assigned correctly. After assigning correctly each atom, the model was refined kinematically using *OLEX2* (Dolomanov et al., 2009). *AFIX 66* command was used to put restraints on the geometry of the benzene ring of the molecule. Restraints were also placed on some interatomic distances and angles. We see the crystal structure together with the observed electrostatic potential (F*obs*) in Figure 6.7.

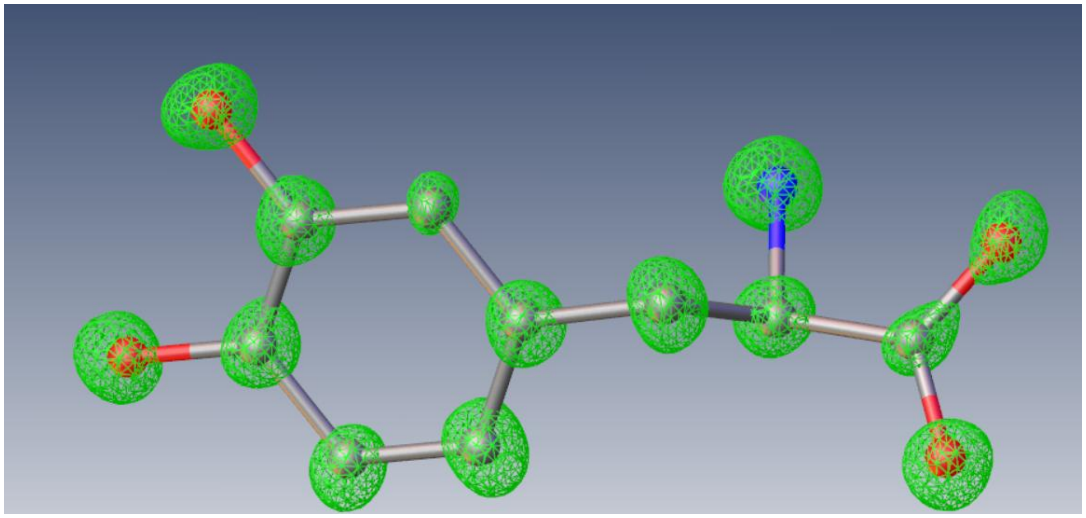

Figure 6. 7 Fourier maps of the observed electrostatic potential after the kinematical refinement of the L-Dopa structure.

The thermal parameters were isotropic however they were all negative after the refinement. The kinematical refinement converged to R*obs of* 45.47% which is high for what is typically obtained from 3D ED.

Conclusion

In this work, we have shown the potential of SerialED data on pharmaceutical crystals which can be extremely beam-sensitive. We have demonstrated that it is possible to obtain a model *ab initio*, however, the data processing is still critical in delivering data that yield quite high R-values. This was a preliminary test done in the very last period of the thesis. Possible future improvements, that are about to be set up, will involve SerialED data collection in precession mode. The precession should increase the integration over the excitation error of the reflection in each pattern, which will make it easier the indexing step and deliver more reliable reflection intensities. This we believe will also reduce the number of rejected frames during the indexing of the data. The potential of the *PETS2* software will further be exploited in the data process. Further expansion in SerialED will be instrumental in the analysis of beam-sensitive materials with unknown crystal structures.

CONCLUSION AND FUTURE PERSPECTIVES

This work has shown that 3D ED is a powerful tool for the structural characterization of organic nanocrystals, where traditional methods fail due to crystal size limitations. This was demonstrated by applying the technique on two areas of pharmaceutics not widely explored in 3D ED: on nanocrystalline natural products and on cocrystals obtained by mechanochemical synthesis. One of the challenges associated with 3D ED is the beam and vacuum sensitivity of the samples being investigated. This was addressed in this work by exemplifying how 3D ED, combined with cryo-cooling and cryo-plunging sample preparation, along with routine solid-state analysis, can elucidate the crystal structures of crystalline samples that are sensitive to beam and high vacuum conditions. It was also demonstrated that 3D ED can play an important role in identifying and exploring the polymorphic landscape of APIs and natural compounds, whose crystalline forms can exist as phase mixtures of submicron crystal sizes.

While significant progress has been made in the electron diffraction field since it was first introduced, further developments can still be achieved, which can focus on potentially increasing the areas of application. This can be done combining the recent advancements in Artificial Intelligence (AI) for crystal recognition to fully automate the data acquisition workflows for the different diffraction data collection methods such the PEDT, cRED, and SerialED. This will significantly increase the efficiency of the 3D ED technique and can address the problem of beam sensitivity of the samples. Automation of the technique will also facilitate the adoption of 3D ED into the industrial world as a possible industrial platform for quality control of chemical syntheses.

Another challenge faced in 3D ED involve samples that diffract only to low resolution which makes crystal structure solution difficult. Applying AI in 3D ED for solving the phase problem by using machine learning algorithms can be instrumental for *ab-initio* structure solutions in such cases.

Ultimately, the potential of the 3D ED technique remains far from being fully realized. With ongoing works being done by different institutions in the field, the future remains bright.

References

Aitipamula, S., & Vangala, V. R. (2017). X-Ray Crystallography and its Role in Understanding the Physicochemical Properties of Pharmaceutical Cocrystals. *Journal of the Indian Institute of Science*, *97*(2). https://doi.org/10.1007/s41745-017-0026-4

Altomare, A., Cuocci, C., Gatta, G. D., Moliterni, A., & Rizzi, R. (2017). Methods of crystallography: Powder x-ray diffraction. *European Mineralogical Union Notes in Mineralogy*, *19*, 79–138. https://doi.org/10.1180/EMU-notes.19.3

A.Mostad, T.Ottersen, & C.Romming. (1971). On the Structure pf L-Dopa. *Acta Chemica Scandinavica*, *25*, 3549–3560. https://doi.org/10.3891/acta.chem.scand.25-3549

Andrusenko, I., & Gemmi, M. (2022). 3D electron diffraction for structure determination of small-molecule nanocrystals: A possible breakthrough for the pharmaceutical industry. In *Wiley Interdisciplinary Reviews: Nanomedicine and Nanobiotechnology* (Vol. 14, Issue 5). John Wiley and Sons Inc. https://doi.org/10.1002/wnan.1810

Andrusenko, I., Hamilton, V., Lanza, A. E., Hall, C. L., Mugnaioli, E., Potticary, J., Buanz, A., Gaisford, S., Piras, A. M., Zambito, Y., Hall, S. R., & Gemmi, M. (2021). Structure determination, thermal stability and dissolution rate of δ-indomethacin. *International Journal of Pharmaceutics*, *608*, 121067. https://doi.org/10.1016/J.IJPHARM.2021.121067

Andrusenko, I., Hamilton, V., Mugnaioli, E., Lanza, A., Hall, C., Potticary, J., Hall, S. R., & Gemmi, M. (2019). The Crystal Structure of Orthocetamol Solved by 3D Electron Diffraction. *Angewandte Chemie*, *131*(32), 11035–11038. https://doi.org/10.1002/ange.201904564

Anyfanti, G., Husanu, E., Andrusenko, I., Marchetti, D., & Gemmi, M. (2024). The crystal structure of olanzapine form III. *IUCrJ*, *11*(5), 843–848. https://doi.org/10.1107/S2052252524007383

Basoccu, F., De Luca, L., & Porcheddu, A. (2024). Mechanochemistry in Organic Synthesis: An Italian Journey through Innovations. In *European Journal of Organic Chemistry* (Vol. 27, Issue 30). John Wiley and Sons Inc. https://doi.org/10.1002/ejoc.202400425

Bolla, G., Sarma, B., & Nangia, A. K. (2022). Crystal Engineering of Pharmaceutical Cocrystals in the Discovery and Development of Improved Drugs. In *Chemical Reviews* (Vol. 122, Issue 13, pp. 11514–11603). American Chemical Society. https://doi.org/10.1021/acs.chemrev.1c00987

Bollweg, W., Maurer, H., & Kroll, H. (1997). *Numerical Prediction of Crystal Structures by Simulated Annealing*.

Boothroyd, S., Kerridge, A., Broo, A., Buttar, D., & Anwar, J. (2018). Why Do Some Molecules Form Hydrates or Solvates? *Crystal Growth and Design*, *18*(3), 1903–1908. https://doi.org/10.1021/acs.cgd.8b00160

Borka, L. (1974). The polymorphism of indomethacine. New modifications, their melting behaviour and solubility. *Acta Pharmaceutica Suecica*, *11*(3), 295–303.

Braga, D., Casali, L., & Grepioni, F. (2022). The Relevance of Crystal Forms in the Pharmaceutical Field: Sword of Damocles or Innovation Tools? *International Journal of Molecular Sciences 2022, Vol. 23, Page 9013*, *23*(16), 9013. https://doi.org/10.3390/IJMS23169013

Brázda, P., Palatinus, L., & Babor, M. (2019). Electron diffraction determines molecular absolute configuration in a pharmaceutical nanocrystal. *Science*, *364*(6441), 667–669. https://doi.org/10.1126/science.aaw2560

Bruhn, J. F., Scapin, G., Cheng, A., Mercado, B. Q., Waterman, D. G., Ganesh, T., Dallakyan, S., Read, B. N., Nieusma, T., Lucier, K. W., Mayer, M. L., Chiang, N. J., Poweleit, N., McGilvray, P. T., Wilson, T. S., Mashore, M., Hennessy, C., Thomson, S., Wang, B., … Carragher, B. (2021). Small Molecule Microcrystal Electron Diffraction for the Pharmaceutical Industry–Lessons Learned From Examining Over Fifty Samples. *Frontiers in Molecular Biosciences*, *8*, 648603. https://doi.org/10.3389/FMOLB.2021.648603/BIBTEX

Bücker, R., Hogan-Lamarre, P., Mehrabi, P., Schulz, E. C., Bultema, L. A., Gevorkov, Y., Brehm, W., Yefanov, O., Oberthür, D., Kassier, G. H., & Dwayne Miller, R. J. (2020). Serial protein crystallography in an electron microscope. *Nature Communications*, *11*(1). https://doi.org/10.1038/s41467-020-14793-0

Bücker, R., Hogan-Lamarre, P., & Miller, R. J. D. (2021). Serial Electron Diffraction Data Processing With diffractem and CrystFEL. *Frontiers in Molecular Biosciences*, *8*. https://doi.org/10.3389/fmolb.2021.624264

Bunaciu, A. A., Udriştioiu, E. gabriela, & Aboul-Enein, H. Y. (2015). X-Ray Diffraction: Instrumentation and Applications. In *Critical Reviews in Analytical Chemistry* (Vol. 45, Issue 4, pp. 289–299). Taylor and Francis Ltd. https://doi.org/10.1080/10408347.2014.949616

Burla, M. C., Caliandro, R., Carrozzini, B., Cascarano, G. L., Cuocci, C., Giacovazzo, C., Mallamo, M., Mazzone, A., & Polidori, G. (2015). Crystal structure determination and refinement via SIR2014. *Journal of Applied Crystallography*, *48*(1), 306–309. https://doi.org/10.1107/S1600576715001132

Byrn, S. R., Zografi, G., & Chen, X. (2017). *Solid-State Properties of Pharmaceutical Materials*. Wiley. https://books.google.it/books?id=nXMsDwAAQBAJ

Carson, M., & Bugg, C. E. (1986). Computer Program Abstracts BSRIBBON-program for pro-ducing 3D ribbon models of macromolecules suitable for interactive graphics display. By. In *COMPUTER PROGRAM ABSTRACTS issue ofthe Journal[J. AppL CrysL* (Vol. 18).

Carstens, T., Haynes, D. A., & Smith, V. J. (2020). Cocrystals: Solution, Mechanochemistry, and Sublimation. *Crystal Growth and Design*, *20*(2), 1139–1149. https://doi.org/10.1021/acs.cgd.9b01450

Chapman, H. N., Caleman, C., & Timneanu, N. (2014). Diffraction before destruction. *Philosophical Transactions of the Royal Society B: Biological Sciences*, *369*(1647). https://doi.org/10.1098/rstb.2013.0313

Chapman, H. N., Fromme, P., Barty, A., White, T. A., Kirian, R. A., Aquila, A., Hunter, M. S., Schulz, J., Deponte, D. P., Weierstall, U., Doak, R. B., Maia, F. R. N. C., Martin, A. V., Schlichting, I., Lomb, L., Coppola, N., Shoeman, R. L., Epp, S. W., Hartmann, R., … Spence, J. C. H. (2011). Femtosecond X-ray protein nanocrystallography. *Nature*, *470*(7332), 73–78. https://doi.org/10.1038/nature09750

Chatsumpun, N., Chuanasa, T., Sritularak, B., Lipipun, V., Jongbunprasert, V., Ruchirawat, S., Ploypradith, P., & Likhitwitayawuid, K. (2016). Oxyresveratrol: Structural modification and evaluation of biological activities. *Molecules*, *21*(4). https://doi.org/10.3390/molecules21040489

Chernyshev, V. V. (2023). Structural Characterization of Pharmaceutical Cocrystals with the Use of Laboratory X-ray Powder Diffraction Patterns. *Crystals 2023, Vol. 13, Page 640*, *13*(4), 640. https://doi.org/10.3390/CRYST13040640

Chhetri, B. K., Lavoie, S., Sweeney-Jones, A. M., & Kubanek, J. (2018). Recent trends in the structural revision of natural products. In *Natural Product Reports* (Vol. 35, Issue 6, pp. 514–531). Royal Society of Chemistry. https://doi.org/10.1039/c8np00011e

Chopra, B., & Dhingra, A. K. (2021). Natural products: A lead for drug discovery and development. In *Phytotherapy Research* (Vol. 35, Issue 9, pp. 4660–4702). John Wiley and Sons Ltd. https://doi.org/10.1002/ptr.7099

Clabbers, M. T. B., & Xu, H. (2020). Microcrystal electron diffraction in macromolecular and pharmaceutical structure determination. In *Drug Discovery Today: Technologies* (Vol. 37, pp. 93–105). Elsevier Ltd. https://doi.org/10.1016/j.ddtec.2020.12.002

Coelho, A. A. (2018). TOPAS and TOPAS-Academic: An optimization program integrating computer algebra and crystallographic objects written in C++: An. *Journal of Applied Crystallography*, *51*(1), 210–218. https://doi.org/10.1107/S1600576718000183

Couillaud, B. M., Espeau, P., Mignet, N., & Corvis, Y. (2019). State of the Art of Pharmaceutical Solid Forms: from Crystal Property Issues to Nanocrystals Formulation. In *ChemMedChem* (Vol. 14, Issue 1, pp. 8–23). John Wiley and Sons Ltd. https://doi.org/10.1002/cmdc.201800612

Cowley, J. M. (1992). *Electron Diffraction Techniques* (Issue v. 2). International Union of Crystallography. https://books.google.it/books?id=y6trFXL1TGEC

Danelius, E., Halaby, S., Van Der Donk, W. A., & Gonen, T. (2021). MicroED in natural product and small molecule research. In *Natural Product Reports* (Vol. 38, Issue 3, pp. 423–431). Royal Society of Chemistry. https://doi.org/10.1039/d0np00035c

Deng, H., He, X., Xu, Y., & Hu, X. (2012). Oxyresveratrol from Mulberry as a dihydrate. *Acta Crystallographica Section E: Structure Reports Online*, *68*(5). https://doi.org/10.1107/S1600536812014018

Dhaval, M., Dudhat, K., Gadoya, A., Shah, S., Pethani, T., Jambukiya, N., Patel, A., Kalsariya, C., Ansari, J., & Borkhataria, C. (2025). Pharmaceutical Salts: Comprehensive Insights From Fundamental Chemistry to FDA Approvals (2019-2023). In *AAPS PharmSciTech* (Vol. 26, Issue 1, p. 36). https://doi.org/10.1208/s12249-024-03020-4

Dias, D. A., Urban, S., & Roessner, U. (2012). A Historical overview of natural products in drug discovery. In *Metabolites* (Vol. 2, Issue 2, pp. 303–336). MDPI AG. https://doi.org/10.3390/metabo2020303

Do, J. L., & Friščić, T. (2017). Mechanochemistry: A Force of Synthesis. *ACS Central Science*, *3*(1), 13–19. https://doi.org/10.1021/acscentsci.6b00277

Dobro, M. J., Melanson, L. A., Jensen, G. J., & McDowall, A. W. (2010). Plunge Freezing for Electron Cryomicroscopy. In *Methods in Enzymology* (Vol. 481, pp. 63–82). Elsevier. https://linkinghub.elsevier.com/retrieve/pii/S0076687910810031

Dolomanov, O. V., Bourhis, L. J., Gildea, R. J., Howard, J. A. K., & Puschmann, H. (2009). OLEX2: A complete structure solution, refinement and analysis program. *Journal of Applied Crystallography*, *42*(2), 339–341. https://doi.org/10.1107/S0021889808042726

Dorset, D. L. (1995). Structural Electron Crystallography. In *Structural Electron Crystallography*. Springer US. https://doi.org/10.1007/978-1-4757-6621-9

Escalante, C. F., Fabian, C., & Sierra, E. (2019). *Fundamentals of transmission electron microscopy, the technique with the best resolution in the world*. https://www.researchgate.net/publication/330999184

Freer, A. A., J. M. Bunyan, N. Shankland, & D. B. Sheen. (1993). Structure of (S)-(+)-ibuprofen. *Acta Crystallographica Section C*. https://doi.org/doi.org/10.1107/S0108270193000629

Frisch, M. J., Trucks, G. W., Schlegel, H. B., Scuseria, G. E., Robb, M. A., Cheeseman, J. R., Scalmani, G., Barone, V., Petersson, G. A., Nakatsuji, H., Li, X., Caricato, M., Marenich, A. V, Bloino, J., Janesko, B. G., Gomperts, R., Mennucci, B., Hratchian, H. P., Ortiz, J. V, … Fox, D. J. (2016). *Gaussian˜16 Revision C.01*.

Galant, O., Cerfeda, G., McCalmont, A. S., James, S. L., Porcheddu, A., Delogu, F., Crawford, D. E., Colacino, E., & Spatari, S. (2022). Mechanochemistry Can Reduce Life Cycle Environmental Impacts of Manufacturing Active Pharmaceutical Ingredients.

ACS Sustainable Chemistry and Engineering, *10*(4), 1430–1439. https://doi.org/10.1021/acssuschemeng.1c06434

Gemmi, M., La Placa, M. G. I., Galanis, A. S., Rauch, E. F., & Nicolopoulos, S. (2015). Fast electron diffraction tomography. *Journal of Applied Crystallography*, *48*, 718–727. https://doi.org/10.1107/S1600576715004604

Gemmi, M., & Lanza, A. E. (2019). 3D electron diffraction techniques. *Acta Crystallographica Section B: Structural Science, Crystal Engineering and Materials*, *75*, 495–504. https://doi.org/10.1107/S2052520619007510

Gemmi, M., Mugnaioli, E., Gorelik, T. E., Kolb, U., Palatinus, L., Boullay, P., Hovmöller, S., & Abrahams, J. P. (2019). 3D electron diffraction: The nanocrystallography revolution. In *ACS Central Science* (Vol. 5, Issue 8, pp. 1315–1329). American Chemical Society. https://doi.org/10.1021/acscentsci.9b00394

Gemmi, M., & Nicolopoulos, S. (2007). Structure solution with three-dimensional sets of precessed electron diffraction intensities. *Ultramicroscopy*, *107*(6–7), 483–494. https://doi.org/10.1016/j.ultramic.2006.03.010

Giacovazzo, C., Monaco, H. L., Artioli, G., Viterbo, D., Milanesio, M., Gilli, G., Gilli, P., Zanotti, G., Ferraris, G., & Catti, M. (2013). Fundamentals of Crystallography. In *Fundamentals of Crystallography*. Oxford University Press. https://doi.org/10.1093/acprof:oso/9780199573653.001.0001

Gogoi, D., Sasaki, T., Nakane, T., Kawamoto, A., Hojo, H., Kurisu, G., & Thakuria, R. (2023). Structure Elucidation of Olanzapine Molecular Salts by Combining Mechanochemistry and Micro-Electron Diffraction. *Crystal Growth and Design*, *23*(8), 5821–5826. https://doi.org/10.1021/acs.cgd.3c00432

Goodhew, P. (2011). *General Introduction to Transmission Electron Microscopy (TEM)*.

Grosse-Kunstleve, R. W., Sauter, N. K., Moriarty, N. W., & Adams, P. D. (2002). Applied Crystallography The Computational Crystallography Toolbox: crystallographic algorithms in a reusable software framework. *Computational Crystallography Toolbox J. Appl. Cryst*, *35*. http://www.fftw.org/

Gurung, K., Šimek, P., Jegorov, A. J., & Palatinus, L. (2024). Structure and absolute configuration of natural fungal product beauveriolide I, isolated from Cordyceps javanica, determined by 3D electron diffraction. *Acta Crystallographica Section C: Structural Chemistry*, *80*(Pt 3), 56–61. https://doi.org/10.1107/S2053229624001359

Harry G. Brittain. (2009). *Polymorphism in Pharmaceutical Solids*. https://doi.org/https://doi.org/10.3109/9781420073225

Harvey, A. L., Edrada-Ebel, R., & Quinn, R. J. (2015). The re-emergence of natural products for drug discovery in the genomics era. In *Nature Reviews Drug Discovery* (Vol. 14, Issue 2, pp. 111–129). Nature Publishing Group. https://doi.org/10.1038/nrd4510

Hasa, D., & Jones, W. (2017). Screening for new pharmaceutical solid forms using mechanochemistry: A practical guide. In *Advanced Drug Delivery Reviews* (Vol. 117, pp. 147–161). Elsevier B.V. https://doi.org/10.1016/j.addr.2017.05.001

Healy, A. M., Worku, Z. A., Kumar, D., & Madi, A. M. (2017). Pharmaceutical solvates, hydrates and amorphous forms: A special emphasis on cocrystals. In *Advanced Drug Delivery Reviews* (Vol. 117, pp. 25–46). Elsevier B.V. https://doi.org/10.1016/j.addr.2017.03.002

Hogan-Lamarre, P., Luo, Y., Bücker, R., Miller, R. J. D., & Zou, X. (2024). STEM SerialED: achieving high-resolution data for ab initio structure determination of beam-sensitive nanocrystalline materials. *IUCrJ*, *11*(Pt 1), 62–72. https://doi.org/10.1107/S2052252523009661

Hossain Mithu, M. S., Economidou, S., Trivedi, V., Bhatt, S., & Douroumis, D. (2021). Advanced Methodologies for Pharmaceutical Salt Synthesis. In *Crystal Growth and Design* (Vol. 21, Issue 2, pp. 1358–1374). American Chemical Society. https://doi.org/10.1021/acs.cgd.0c01427

Husanu, E., Agbemeh, V. E., Andrusenko, I., Marchetti, D., Sonaglioni, D., & Gemmi, M. (2024). Polymorphism in oxyresveratrol studied by 3D ED. *ACS Omega*. https://doi.org/10.1021/ACSOMEGA.4C05292

Ito, S., & Yamano, A. (2022). Breaking the 1-μm barrier with the electron diffractometer XtaLAB Synergy-ED. In *Rigaku Journal* (Vol. 38, Issue 1).

Jayant, V., & Yusuf, M. (2024). Insights into polymorphism and inclusion properties in organic compounds. *Discover Chemistry*, *1*(1), 52. https://doi.org/10.1007/s44371-024-00054-2

Joshi, K., Chandra, A., Jain, K., & Talegaonkar, S. (2019). Nanocrystalization: An Emerging Technology to Enhance the Bioavailability of Poorly Soluble Drugs. *Pharmaceutical Nanotechnology*, *7*(4), 259–278. https://doi.org/10.2174/2211738507666190405182524

Kabsch, W. (2010). *XDS*. *Acta Crystallographica Section D Biological Crystallography*, *66*(2), 125–132. https://doi.org/10.1107/S0907444909047337

Kabsch, W. (2014). Processing of X-ray snapshots from crystals in random orientations. *Acta Crystallographica Section D: Biological Crystallography*, *70*(8), 2204–2216. https://doi.org/10.1107/S1399004714013534

Kim, L. J., Ohashi, M., Zhang, Z., Tan, D., Asay, M., Cascio, D., Rodriguez, J. A., Tang, Y., & Nelson, H. M. (2021). Prospecting for natural products by genome mining and microcrystal electron diffraction. *Nature Chemical Biology*, *17*(8), 872–877. https://doi.org/10.1038/s41589-021-00834-2

Klar, P. B., Krysiak, Y., Xu, H., Steciuk, G., Cho, J., Zou, X., & Palatinus, L. (2023). Accurate structure models and absolute configuration determination using dynamical

effects in continuous-rotation 3D electron diffraction data. *Nature Chemistry*, *15*(6), 848–855. https://doi.org/10.1038/s41557-023-01186-1

Klitou, P., Parisi, E., Bordignon, S., Bravetti, F., Rosbottom, I., Dell'Aera, M., Cuocci, C., Chierotti, M. R., Altomare, A., & Simone, E. (2023). Navigating the Complex Solid Form Landscape of the Quercetin Flavonoid Molecule. *Crystal Growth and Design*, *23*(8), 6034–6045. https://doi.org/10.1021/acs.cgd.3c00584

Kolb, U., Gorelik, T., Kübel, C., Otten, M. T., & Hubert, D. (2007a). Towards automated diffraction tomography: Part I-Data acquisition. *Ultramicroscopy*, *107*(6–7), 507–513. https://doi.org/10.1016/j.ultramic.2006.10.007

Kolb, U., Gorelik, T., Kübel, C., Otten, M. T., & Hubert, D. (2007b). Towards automated diffraction tomography: Part I—Data acquisition. *Ultramicroscopy*, *107*(6–7), 507–513. https://doi.org/10.1016/J.ULTRAMIC.2006.10.007

Li, J., & Sun, J. (2017). Application of X-ray Diffraction and Electron Crystallography for Solving Complex Structure Problems. *Accounts of Chemical Research*, *50*(11), 2737–2745. https://doi.org/10.1021/acs.accounts.7b00366

Lightowler, M., Li, S., Ou, X., Zou, X., Lu, M., & Xu, H. (2021). *Indomethacin Polymorph δ Revealed To Be Two Plastically Bendable Crystal Forms by 3D Electron Diffraction: Correcting a 47-Year-Old Misunderstanding***. https://doi.org/10.33774/chemrxiv-2021-s9fhf

Likhitwitayawuid, K. (2021). Oxyresveratrol: Sources, productions, biological activities, pharmacokinetics, and delivery systems. In *Molecules* (Vol. 26, Issue 14). MDPI AG. https://doi.org/10.3390/molecules26144212

Marchetti, D., Guagnini, F., Lanza, A. E., Pedrini, A., Righi, L., Dalcanale, E., Gemmi, M., & Massera, C. (2021). Combined Approach of Mechanochemistry and Electron Crystallography for the Discovery of 1D and 2D Coordination Polymers. *Crystal Growth and Design*, *21*(12), 6660–6664. https://doi.org/10.1021/acs.cgd.1c01058

Marchetti, D., Pedrini, A., Massera, C., Diouf, M. D. F., Jandl, C., Steinfeld, G., & Gemmi, M. (2023). 3D electron diffraction analysis of a novel, mechanochemically synthesized supramolecular organic framework based on tetrakis-4-(4- pyridyl)phenylmethane. *Acta Crystallographica Section B: Structural Science, Crystal Engineering and Materials*, *79*, 432–436. https://doi.org/10.1107/S2052520623007680

Midgley, P. A., & Eggeman, A. S. (2015). Precession electron diffraction – a topical review. *IUCrJ*, *2*(Pt 1), 126. https://doi.org/10.1107/S2052252514022283

Mugnaioli, E., Gorelik, T., & Kolb, U. (2009). "Ab initio" structure solution from electron diffraction data obtained by a combination of automated diffraction tomography and precession technique. *Ultramicroscopy*, *109*(6), 758–765. https://doi.org/10.1016/j.ultramic.2009.01.011

Nannenga, B. L., Shi, D., Leslie, A. G. W., & Gonen, T. (2014). High-resolution structure determination by continuous-rotation data collection in MicroEDED. *Nature Methods*, *11*(9), 927–930. https://doi.org/10.1038/nmeth.3043

Nederlof, I., Van Genderen, E., Li, Y. W., & Abrahams, J. P. (2013). A Medipix quantum area detector allows rotation electron diffraction data collection from submicrometre three-dimensional protein crystals. *Acta Crystallographica Section D: Biological Crystallography*, *69*(7), 1223–1230. https://doi.org/10.1107/S0907444913009700

Newman, D. J., & Cragg, G. M. (2016). Natural Products as Sources of New Drugs from 1981 to 2014. In *Journal of Natural Products* (Vol. 79, Issue 3, pp. 629–661). American Chemical Society. https://doi.org/10.1021/acs.jnatprod.5b01055

Nicolaou, K. C., & Snyder, S. A. (2005). Chasing molecules that were never there: Misassigned natural products and the role of chemical synthesis in modern structure elucidation. In *Angewandte Chemie - International Edition* (Vol. 44, Issue 7, pp. 1012–1044). https://doi.org/10.1002/anie.200460864

Oszlányi, G., & Sütő, A. (2004). Ab initio structure solution by charge flipping. *Acta Crystallographica Section A: Foundations of Crystallography*, *60*(2), 134–141. https://doi.org/10.1107/S0108767303027569

Ouiyangkul, P., Saithong, S., & Tantishaiyakul, V. (2020). Syntheses and crystal structures of hydrated and anhydrous 1:2 cocrystals of oxyresveratrol and zwitterionic proline. *Acta Crystallographica Section E: Crystallographic Communications*, *76*, 1528–1534. https://doi.org/10.1107/S2056989020011536

Pal, R., Jelsch, C., Momma, K., & Grabowsky, S. (2022). π-Hole bonding in a new co-crystal hydrate of gallic acid and pyrazine: static and dynamic charge density analysis. *Acta Crystallographica Section B: Structural Science, Crystal Engineering and Materials*, *78*, 231–246. https://doi.org/10.1107/S2052520622001457

Palatinus, L., Brázda, P., Jelínek, M., Hrdá, J., Steciuk, G., & Klementová, M. (2019a). Specifics of the data processing of precession electron diffraction tomography data and their implementation in the program PETS2.0. *Acta Crystallographica Section B: Structural Science, Crystal Engineering and Materials*, *75*, 512–522. https://doi.org/10.1107/S2052520619007534

Palatinus, L., Brázda, P., Jelínek, M., Hrdá, J., Steciuk, G., & Klementová, M. (2019b). Specifics of the data processing of precession electron diffraction tomography data and their implementation in the program PETS2.0. *Acta Crystallographica Section B: Structural Science, Crystal Engineering and Materials*, *75*, 512–522. https://doi.org/10.1107/S2052520619007534

Palatinus, L., & Chapuis, G. (2007). SUPERFLIP - A computer program for the solution of crystal structures by charge flipping in arbitrary dimensions. *Journal of Applied Crystallography*, *40*(4), 786–790. https://doi.org/10.1107/S0021889807029238

Palatinus, L., Corrêa, C. A., Steciuk, G., Jacob, D., Roussel, P., Boullay, P., Klementová, M., Gemmi, M., Kopeček, J., Domeneghetti, M. C., Cámara, F., & Petříček, V. (2015). Structure refinement using precession electron diffraction tomography and dynamical diffraction: Tests on experimental data. *Acta Crystallographica Section B: Structural Science, Crystal Engineering and Materials*, *71*, 740–751. https://doi.org/10.1107/S2052520615017023

Palatinus, L., Jacob, D., Cuvillier, P., Klementová, M., Sinkler, W., & Marks, L. D. (2013). Structure refinement from precession electron diffraction data. *Acta Crystallographica Section A: Foundations of Crystallography*, *69*(2), 171–188. https://doi.org/10.1107/S010876731204946X

Palatinus, L., Petříček, V., & Correâ, C. A. (2015). Structure refinement using precession electron diffraction tomography and dynamical diffraction: Theory and implementation. *Acta Crystallographica Section A: Foundations and Advances*, *71*, 235–244. https://doi.org/10.1107/S2053273315001266

Petříček, V., Palatinus, L., Plášil, J., & Dušek, M. (2023). J ana 2020 - a new version of the crystallographic computing system J ana. *Zeitschrift Fur Kristallographie - Crystalline Materials*, *238*(7–8), 271–282. https://doi.org/10.1515/ZKRI-2023-0005/DOWNLOADASSET/SUPPL/J_ZKRI-2023-0005_SUPPL.DOCX

Pindelska, E., Sokal, A., & Kolodziejski, W. (2017). Pharmaceutical cocrystals, salts and polymorphs: Advanced characterization techniques. In *Advanced Drug Delivery Reviews* (Vol. 117, pp. 111–146). Elsevier B.V. https://doi.org/10.1016/j.addr.2017.09.014

Plana-Ruiz, S., Krysiak, Y., Portillo, J., Alig, E., Estradé, S., Peiró, F., & Kolb, U. (2020). Fast-ADT: A fast and automated electron diffraction tomography setup for structure determination and refinement. *Ultramicroscopy*, *211*. https://doi.org/10.1016/j.ultramic.2020.112951

Qiao, N., Li, M., Schlindwein, W., Malek, N., Davies, A., & Trappitt, G. (2011). Pharmaceutical cocrystals: An overview. In *International Journal of Pharmaceutics* (Vol. 419, Issues 1–2, pp. 1–11). Elsevier B.V. https://doi.org/10.1016/j.ijpharm.2011.07.037

R. F. Egerton. (2005). An Introduction to TEM, SEM, and AEM. In *Physical Principles of Electron Microscopy* (1st ed., pp. XII–202). Springer New York, NY. https://doi.org/https://doi.org/10.1007/b136495

Reutzel-Edens, S. M., & Bhardwaj, R. M. (2020). Crystal forms in pharmaceutical applications: Olanzapine, a gift to crystal chemistry that keeps on giving. *IUCrJ*, *7*(6), 955–964. https://doi.org/10.1107/S2052252520012683/YC5024SUP1.PDF

Sakamoto, N., Tsuno, N., Koyama, R., Gato, K., Titapiwatanakun, V., Takatori, K., & Fukami, T. (2021). Four Novel Pharmaceutical Cocrystals of Oxyresveratrol, Including a 2 : 3 Cocrystal with Betaine. In *Chem. Pharm. Bull* (Vol. 69, Issue 10).

Sala, A., Faye Diouf, M. D., Marchetti, D., Pasquale, L., & Gemmi, M. (2024). Mechanochemical Synthesis and Three-Dimensional Electron Diffraction Structure Solution of a Novel Cu-Based Protocatechuate Metal-Organic Framework. *Crystal Growth and Design*, *24*(8), 3246–3255. https://doi.org/10.1021/acs.cgd.3c01494

Sanphui, P., Goud, N. R., Khandavilli, U. B. R., Bhanoth, S., & Nangia, A. (2011). New polymorphs of curcumin. *Chemical Communications*, *47*(17), 5013–5015. https://doi.org/10.1039/c1cc10204d

Savjani, K. T., Gajjar, A. K., & Savjani, J. K. (2012). Drug Solubility: Importance and Enhancement Techniques. *ISRN Pharmaceutics*, *2012*, 1–10. https://doi.org/10.5402/2012/195727

Schneider, T. R., & Sheldrick, G. M. (2002). Biological Crystallography Substructure solution with SHELXD. *Sheldrick Substructure Solution with SHELXD Acta Cryst*.

Sheldrick, G. M. (2015a). Crystal structure refinement with SHELXL. *Acta Crystallographica Section C: Structural Chemistry*, *71*, 3–8. https://doi.org/10.1107/S2053229614024218

Sheldrick, G. M. (2015b). SHELXT - Integrated space-group and crystal-structure determination. *Acta Crystallographica Section A: Foundations of Crystallography*, *71*(1), 3–8. https://doi.org/10.1107/S2053273314026370

Simoncic, P., Romeijn, E., Hovestreydt, E., Steinfeld, G., Santiso-Quiñones, G., & Merkelbach, J. (2023). Electron crystallography and dedicated electron-diffraction instrumentation. *Acta Crystallographica Section E: Crystallographic Communications*, *79*(Pt 5), 410–422. https://doi.org/10.1107/S2056989023003109

Smeets, S., Zou, X., & Wan, W. (2018). Serial electron crystallography for structure determination and phase analysis of nanocrystalline materials. *Journal of Applied Crystallography*, *51*(5), 1262–1273. https://doi.org/10.1107/S1600576718009500

Southern, S. A., & Bryce, D. L. (2021). Recent advances in NMR crystallography and polymorphism. In *Annual Reports on NMR Spectroscopy* (Vol. 102, pp. 1–80). Academic Press Inc. https://doi.org/10.1016/bs.arnmr.2020.10.001

Spence, J. C. H. (2017). XFELs for structure and dynamics in biology. *IUCrJ*, *4*, 322–339. https://doi.org/10.1107/S2052252517005760

Springob, K., & Kutchan, T. M. (2009). Introduction to the different classes of natural products. In *Plant-derived Natural Products: Synthesis, Function, and Application* (pp. 3–50). Springer US. https://doi.org/10.1007/978-0-387-85498-4_1

Suzuki, Y., Muangnoi, C., Thaweesest, W., Teerawonganan, P., Ratnatilaka, P., Bhuket, N., Titapiwatanakun, V., Yoshimura-Fujii, M., Sritularak, B., Likhitwitayawuid, K., Rojsitthisak, P., & Fukami, T. (2019). Exploring Novel Cocrystalline Forms of Oxyresveratrol to Enhance Aqueous Solubility and Permeability across a Cell

Monolayer. In *Biol. Pharm. Bull* (Vol. 42, Issue 6). https://doi.org/10.1248/bpb.b19-00048

Teka, T., Zhang, L., Ge, X., Li, Y., Han, L., & Yan, X. (2022). Stilbenes: Source plants, chemistry, biosynthesis, pharmacology, application and problems related to their clinical Application-A comprehensive review. In *Phytochemistry* (Vol. 197). Elsevier Ltd. https://doi.org/10.1016/j.phytochem.2022.113128

Thaklaewphan, P., Wikan, N., Potikanond, S., & Nimlamool, W. (2024). Oxyresveratrol Enhances the Anti-Cancer Effect of Cisplatin against Epithelial Ovarian Cancer Cells through Suppressing the Activation of Protein Kinase B (AKT). *Biomolecules*, *14*(9), 1140. https://doi.org/10.3390/biom14091140

Ticona Chambi, J., Fandaruff, C., & Cuffini, S. L. (2024). Identification and quantification techniques of polymorphic forms - A review. In *Journal of Pharmaceutical and Biomedical Analysis* (Vol. 242). Elsevier B.V. https://doi.org/10.1016/j.jpba.2024.116038

Van Genderen, E., Clabbers, M. T. B., Das, P. P., Stewart, A., Nederlof, I., Barentsen, K. C., Portillo, Q., Pannu, N. S., Nicolopoulos, S., Gruene, T., & Abrahams, J. P. (2016). Ab initio structure determination of nanocrystals of organic pharmaceutical compounds by electron diffraction at room temperature using a Timepix quantum area direct electron detector. *Acta Crystallographica. Section A, Foundations and Advances*, *72*(Pt 2), 236–242. https://doi.org/10.1107/S2053273315022500

Vincent, R., & Midgley, P. A. (1994). Double conical beam-rocking system for measurement of integrated electron diffraction intensities. In *Ultramicroscopy* (Vol. 53).

Wan, W., Sun, J., Su, J., Hovmöller, S., & Zou, X. (2013). Three-dimensional rotation electron diffraction: Software RED for automated data collection and data processing. *Journal of Applied Crystallography*, *46*(6), 1863–1873. https://doi.org/10.1107/S0021889813027714/NB5079SUP1.PDF

Wang, B., Zou, X., & Smeets, S. (2019). Automated serial rotation electron diffraction combined with cluster analysis: An efficient multi-crystal workflow for structure determination. *IUCrJ*, *6*, 854–867. https://doi.org/10.1107/S2052252519007681

Wang, H., Chen, X., Li, J., Chen, Z., Zhou, A., & Ye, L. (2024). Oxyresveratrol from mulberry (Morus alba L.) ameliorates post-inflammatory hyperpigmentation in vitro by anti-melanogenesis, inhibiting melanosome transfer, and providing photoprotection. *Journal of Functional Foods*, *122*. https://doi.org/10.1016/j.jff.2024.106557

Wang, J., Xu, C., Wong, Y. K., Li, Y., Liao, F., Jiang, T., & Tu, Y. (2019). Artemisinin, the Magic Drug Discovered from Traditional Chinese Medicine. *Engineering*, *5*(1), 32–39. https://doi.org/10.1016/j.eng.2018.11.011

Wang, Y., Yang, T., Xu, H., Zou, X., & Wan, W. (2018). On the quality of the continuous rotation electron diffraction data for accurate atomic structure determination of inorganic

compounds. *Journal of Applied Crystallography*, *51*, 1094–1101. https://doi.org/10.1107/S1600576718007604

White, T. A., Kirian, R. A., Martin, A. V., Aquila, A., Nass, K., Barty, A., & Chapman, H. N. (2012). CrystFEL: A software suite for snapshot serial crystallography. *Journal of Applied Crystallography*, *45*(2), 335–341. https://doi.org/10.1107/S0021889812002312

Williams, D. B., & Carter, C. B. (2009). *Transmission Electron Microscopy: A Textbook for Materials Science* (Issue v. 1). Springer. https://books.google.it/books?id=dXdrG39VtUoC

Winter, G., Waterman, D. G., Parkhurst, J. M., Brewster, A. S., Gildea, R. J., Gerstel, M., Fuentes-Montero, L., Vollmar, M., Michels-Clark, T., Young, I. D., Sauter, N. K., & Evans, G. (2018). DIALS: implementation and evaluation of a new integration package. *Urn:Issn:2059-7983*, *74*(2), 85–97. https://doi.org/10.1107/S2059798317017235

Yao, C., Zhang, S., Wang, L., & Tao, X. (2023). Recent Advances in Polymorph Discovery Methods of Organic Crystals. In *Crystal Growth and Design* (Vol. 23, Issue 1, pp. 637–654). American Chemical Society. https://doi.org/10.1021/acs.cgd.2c00960

Zeng, H. J., Li, Q. Y., Ma, J., Yang, R., & Qu, L. B. (2021). A comparative study on the effects of resveratrol and oxyresveratrol against tyrosinase activity and their inhibitory mechanism. *Spectrochimica Acta - Part A: Molecular and Biomolecular Spectroscopy*, *251*. https://doi.org/10.1016/j.saa.2020.119405

Zettili, N. (2009). *Quantum Mechanics: Concepts and Applications*. Wiley. https://books.google.it/books?id=6jXlpJCSz98C

Zhang, D., Oleynikov, P., Hovmoller, S., & Zou, X. (2010). Collecting 3D electron diffraction data by the rotation method. *Zeitschrift Fur Kristallographie*, *225*(2–3), 94–102. https://doi.org/10.1524/zkri.2010.1202

Zhu, L., Chen, X., Abola, E. E., Jing, L., & Liu, W. (2020). Serial Crystallography for Structure-Based Drug Discovery. *Trends in Pharmacological Sciences*, *41*(11), 830–839. https://doi.org/10.1016/j.tips.2020.08.009

Zuo, J. M., & Spence, J. C. H. (2016). *Advanced Transmission Electron Microscopy Imaging and Diffraction in Nanoscience*. Springer. https://doi.org/10.1007/978-1-4939-6607-3

Zuo, J.-M. (2006). Electron Nanocrystallography. In *Handbook of Microscopy for Nanotechnology* (pp. 567–599). Kluwer Academic Publishers. https://doi.org/10.1007/1-4020-8006-9_18